Interactive Buckling and Post-Buckling Studies of Thin-Walled Structural Members with Generalized Beam Theory

Junle Cai

Dissertation submitted to the Faculty of the
Virginia Polytechnic Institute and State University
in partial fulfillment of the requirements for the degree of

Doctor of Philosophy
in
Civil Engineering

Cristopher D. Moen, Chair
Carin L. Roberts-Wollmann
Jeffrey T. Borggaard
Matthew R. Eatherton
Ioannis Koutromanos

December 6, 2016
Blacksburg, Virginia

Keywords: Thin-walled structures; Elastic buckling; Perforations; Holes; Generalized beam theory; Buckling mode decomposition; Post-buckling

Interactive Buckling and Post-Buckling Studies of Thin-Walled Structural Members with Generalized Beam Theory

Junle Cai

ABSTRACT

Most thin-walled metallic structural members experience some extent of interactive buckling that corrodes the load carrying capacity. Current design methods predict the strength of thin-walled metallic structural members based on individual buckling limit-states and limited case of interactive buckling limit state. In order to develop design methods for most coupled buckling limit states, the interaction of buckling modes needs to be studied.

This dissertation first introduces a generally applicable methodology for Generalized Beam Theory (GBT) elastic buckling analysis on members with holes, where the buckling modes of gross cross-section interact with those of net cross-section. The approach treats member with holes as a structural system consisting of prismatic sub-members. These sub-members are connected by enforcing nodal compatibility conditions for the GBT discretization points at the interfaces. To represent the shear lag effect and nonlinear normal stress distribution in the vicinity of a hole, GBT shear modes with nonlinear warping are included. Modifications are made to the GBT geometric stiffness because of the influence from shear lag effect caused by holes. In the following sections, the GBT formulation for a prismatic bar is reviewed and the GBT formulation for members with holes is introduced. Special aspects of analyzing members with holes are defined, namely the compatibility conditions to connect sub-members and the geometric stiffness for members with holes. Validation and three examples are provided.

The second topic of this dissertation involves a buckling mode decomposition method of normalized displacement field, bending stresses and strain energy for thin-walled member displacement field (point clouds or finite element results) based on generalized beam theory (GBT). The method provides quantitative modal participation information regarding eigen-buckling displacement fields, stress components and elastic strain energy, that can be used to inform future design approaches. In the method, GBT modal amplitudes are retrieved at discrete cross-sections, and the modal amplitude field is reconstructed assuming it can be piece-wisely approximated by polynomials. The unit displacement field, stress components and strain energy are all retrieved by using reconstructed GBT modal amplitude field and GBT constitutive laws. Theory and examples are provided, and potential applications are discussed including cold-formed steel member design and post-disaster evaluation of thin-walled structural members.

In the third part, post-buckling modal decomposition is made possible by development of a geometrically nonlinear GBT software. This tool can be used to assist understanding couple-buckling limit-states. Lastly, the load-deformation response considering any one GBT mode is derived analytically for fast computation and interpretation of structural post-buckling behavior.

Interactive Buckling and Post-Buckling Studies of Thin-Walled Structural Members with Generalized Beam Theory

Junle Cai

GENERAL AUDIENCE ABSTRACT

Here I present novel analytical methods to quantitatively decompose interactive buckling in the thin-walled structures. Interactive buckling, where multiple buckling modes are present to initiate structure failure, often controls the load-carrying capacity of thin-walled structures, e.g., the amount of load a column can withstand or the maximum acceleration a space shuttle can experience. In this research, based on Generalized Beam Theory, I describe in detail the analytical methods revealing how buckling modes are coupled and contribute to key quantities related to the structural failure, namely, displacement, stress, and strain energy. I obtain the algorithms by performing rigorous mathematical derivations based on thin-walled mechanics. The research not only facilitates better building design according to the simplified method in the current design standard, but also enables advanced, nonlinear modal decomposition analysis using the custom-made Finite Element program. These studies aim to provide the quantitative understanding of the coupled buckling mechanism and further the development of more powerful strength prediction methods for thin-walled structures.

Acknowledgments

No words could properly thank the wonderful people who made the past four years so unforgettable. Thank you so much to my wife, Jiaxing, for her love and unconditional believing in me. I could not have done it without her. Thank you to my parents, my brother and sister-in-law, and my parents-in-law. It is their spiritual support that made all of these possible.

My advisor Dr. Cris Moen should be credited much for if any accomplishment. I am grateful that he always put his trust in me. He dedicated more than enough effort and energy to grooming me, from a student to a well-rounded researcher. He is not only a 'boss' but also a mentor and a friend. It is because of his words of encouragement I am more actively engaged with other researchers and engineers. He cared dearly about me and Jiaxing all the time and helped us in numerous ways. He invited the research group and friends to relax from time to time (and always pays the bill :), which brought us a ton of fun in the pressuring academic life. He taught me so many things besides academics, e.g., always be a salesman and sell yourself. I feel very lucky I could be mentored by someone so brilliant and open-minded. He brought me into the world of structure stability and it definitely grows on me.

I would like to express my sincere gratitude to Dr. Ioannis Koutromanos. I learned many of my research skills from his classes - one piece of my work is originated from the final project of his class. I benefited a lot from our discussions. I took my very first class at Virginia Tech as the TA for Dr. Carin Roberts-Wollmann's class. She was very devoted for every class making sure students were learning. She showed me how to be an easy-going person but at the same time be serious when it came to work. I would also like to thank her for the career advice she gave me. I was also TA for Dr. Matthew Eatherton. He always trusted me on his students. He was very enthusiastic and diligent about teaching and research and set a great role model for me. I am very grateful to Dr. Jeffrey Borggaard, he opened my eyes to the world outside of civil engineering and my work could not be done without his teaching.

I enjoyed the company of my fellow graduate students - especially Aritra, Abraham, Rafic, Fannie, Chenxi, Youyou, Yu, Kenny, David, Adrian, Bohan, Haiteng, Ding. Thank Dr. David Mokarem, Mr. Brett Farmer and Mr. Dennis Huffman for their advice. Thank Dr. Raymond Plaut and Dr. Ben Schafer for their precious guidance. Last but not least, thank Virginia Tech for being my sweet home for four years. Go Hokies!

Contents

List of Figures

List of Tables

List of Publications

[1] Cai, J., Schafer, B. W. and Moen, C. D. (2017). "CUFSM Elastic Buckling Analysis Software Module for Quantifying Hole Effects in Thin-Walled Structural Members." Proceedings of the Annual Stability Conference, USA, San Antonio, TX.

[2] Cai, J., and Moen, C. D. (2016a). "Elastic buckling analysis of thin-walled structural members with rectangular holes using generalized beam theory." Thin-Walled Structures. 2016 Oct;107:274–86.

[3] Cai, J., and Moen, C. D. (2016b). "Elastic buckling mode decomposition of displacement, strain energy and stress components for thin-walled structural members." Proceedings of the Annual Stability Conference, USA, Orlando, FL.

[4] Cai, J., and Moen, C. D. (2015a). "Generalized beam theory buckling analysis for members with holes." Proceedings of Eighth International Conference on Advances in Steel Structures, Lisbon, Portugal.

[5] Cai, J., and Moen, C. D. (2015b). "Automated Buckling Mode Identification of Thin-walled Structures from 3d Mode Shapes or Point Clouds." Proceedings of the Annual Stability Conference, USA, Nashville, TN.

[6] Lama-Salomon, A., Tao, F., Cai, J., and Moen, C. D. (2015). "Buckling mode identification for a cold-formed steel column experiment with 3d image-based reconstruction." Proceedings of the Annual Stability Conference, USA, Nashville, TN.

Chapter 1

Introduction

1.1 Research Motivation and Objectives

Most thin-walled structural members are subject to interactive buckling that degrades the load-carrying capacity. Direct Strength Method (DSM) adopted in AISI-S100-12 [7] and the Australian/New Zealand Standard [56], predicts cold-formed steel member capacity with global (G), distortional (D), or local (L) buckling limit states using three corresponding slenderness ratios as input. For coupled buckling, e.g., coupled D-L buckling, design methods are yet to be developed. The general motivation of this research is (i) to develop eigen buckling mode participation calculation method providing input for Direct Strength Method; (ii) to enable eigen buckling formulation for members with holes, that can be used to decompose the complex buckling mode for members with holes; (iii) to develop tools to evaluate the structural behavior in the post buckling range including the post-buckling modal participation and buckling mode propagation with increasing load.

The goals of this dissertation are (i) to extend Generalized Beam Theory to elastic buckling analysis for thin-walled members with holes, that can be used to predict the strength for members with holes; (ii) to develop buckling mode decomposition methods for metallic thin-walled members for stress, displacement and strain energy; these two outcomes can be used to provide input for current load-carrying capacity prediction methods; (iii) to code a geometrically nonlinear GBT software enabling buckling mode decomposition of post-buckling; (iv) to derive an approximate, analytical solution for column load-deformation response of any one GBT mode.

1.2 Original Contributions of The Research

The original contributions are made in many areas of capacity prediction either for using current Direct Strength Method or in the sense of developing a new method using modal participation.

The first original contribution is made for elastic buckling analysis of members with holes using Generalized Beam Theory. The work has practical motivation aside from extending the theory to members with holes. By the work, elastic buckling mode participation for members with holes is clearly defined, such that capacity prediction can be better accomplished for members with holes using Direct Strength Method.

The second original contribution is the development of an elastic buckling mode decomposition method for unit stress, strain energy, and displacement fields, for members with and without holes. The method processes eigen-buckling solution from finite element method or experimental point clouds and generates modal participation information. The method can serve the purpose of modal identification to provide input for the current strength prediction method; and facilitate the direct strength prediction method for interactive buckling limit state developed in this dissertation.

The third original contribution includes coding of a custom-made computer program for GBT post-buckling analysis. GBT analysis generates buckling mode participation in the post-buckling range, in addition to the displacement field yielded by Shell Finite Element method. Thus, the computer program can assist understanding the modal coupling for interactive buckling limit states.

The fourth original contribution consists of the derivation of the load-deformation response considering any one GBT mode. The formulation can be used to conveniently estimate the post-buckling response and to understand the post-buckling behavior for different GBT modes. The scope of this dissertation is summarized in Figure 1.1.

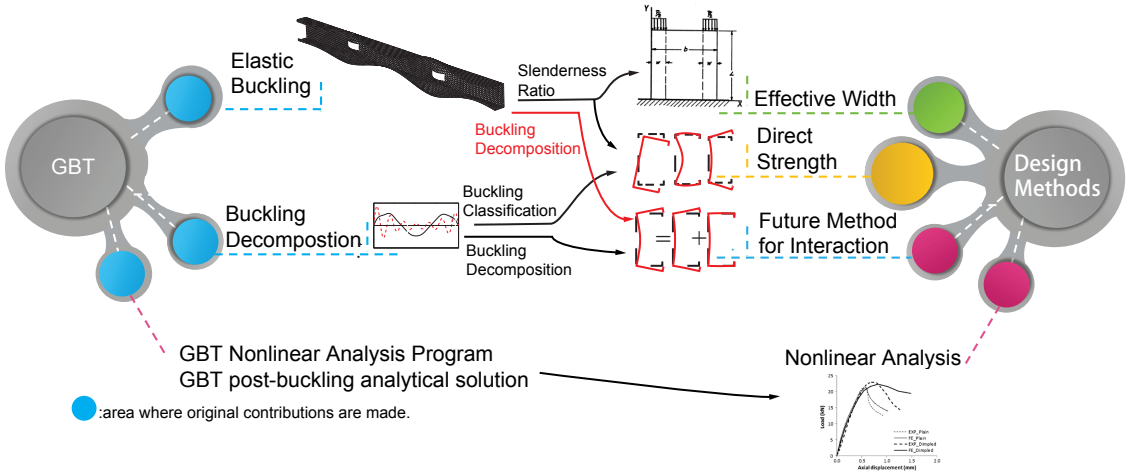

Figure 1.1: Scope of this dissertation: (i) GBT elastic buckling analysis yields buckling mode decomposition naturally and has the ability to compute isolated local, distortional and global buckling loads; it is extended to members with holes in this research (ii) meanwhile, a buckling mode decomposition algorithm is developed to treat shell finite element displacement field and experimental point-cloud performing mode decomposition; (iv) post-buckling mode decomposition is made possible by a custom-made GBT-element software; (v) modal participation provides Direct Strength Method with modal classification information and; (vi) facilitates the novel strength prediction method for strength prediction of interactive buckling limit state; (vii) in addition, analytical formulation is derived for post-buckling response of any one GBT mode.

1.3 Dissertation Organization

The thesis is organized in the following fashion. Chapter 1 includes the objectives and scope of this dissertation, that is to calculate buckling modal participation facilitating existing Direct Strength Method; and to develop a direct method for interactive buckling limit-state using modal participation information. Chapter 2 reviews current strength prediction methods focusing on Direct Strength Method and Perry-Robertson Method for global buckling, since they inspire this dissertation's research on strength prediction method of interactive buckling. Chapter 3 reviews thin-walled mechanics, modal participation calculation methods and Generalized Beam Theory, that paves the road for the original research to follow. For example, the concept that the axial stress being nonlinear for thin-walled member is utilized in the work of GBT for members with holes and strength prediction in the following chapters.

The subsequent chapters document the original work of this research. Chapter 4 introduces the extension of GBT to elastic buckling analysis of members with holes. This research not only extends the theory, but also lays the groundwork for defining/decomposing elastic

buckling mode for members with holes by theory. Chapter 5 elaborates on the modal decomposition algorithm for unit stress, strain energy, and displacement fields, along with the theoretical derivations. The results can either assist classification of buckling modes providing input for Direct Strength Method. Chapter 6 presents the applications for the modal identification scheme for thin-walled members , including finite element eigen-buckling solutions and experimental point-clouds. In Chapter 7, post-bucking modal decomposition is made possible by programming a nonlinear GBT-element software in Matlab. Lastly, Chapter 8 presents the derivation of analytical post-buckling response for any one GBT mode.

Chapter 2

Literature Review of Current Strength Prediction Methods for Thin-Walled Metallic Structural Members

Two strength prediction methods, namely Direct Strength Method (DSM) for thin-walled structural members and Perry-Robertson Method for hot-rolled steel members are reviewed in this Chapter. Direct Strength Method (DSM) is widely used for strength prediction of thin-walled metallic structural members. The method predicts the capacity based on local, distortional and global buckling limit states. Generalized Beam Theory (GBT) is extremely suitable to be used together as analysis tool with DSM, because local, distortional and global buckling modes are inherent in GBT. GBT is the main theory tool used in this dissertation and its usage in DSM is also reviewed in this chapter.

Currently, the way to treat interactive buckling has not been formalized in DSM and one goal of this dissertation is to develop a direct strength prediction method applicable to interactive buckling. This novel direct method is inspired by the Perry-Robertson method, where the deformed shape is assumed identical with that of elastic buckling, and a material failure criteria is defined corresponding with the load-carry capacity. That is the reason the Perry-Robertson method is also reviewed herein.

2.1 Direct Strength Method

The core concept of Direct Strength Method resides in the global, distortional and local buckling of thin-walled members, in contrast to considering buckling of individual plates comprising the member as in the Effective Width Method. Currently, cold-formed steel

Standards predict the load-carrying capacity by specifying the global, distortional and local-plate buckling limit states, e.g., Direct Strength Method (DSM), which is essentially an extension of the column curves for global buckling, but with application to local and distortional buckling instabilities [85]. The global, distortional and local buckling can be defined by Generalized Beam Theory (GBT) with mechanical differentiation. For the ultimate state corresponding to each one of them, the elastic buckling load is linked with predicted strength by fitted experimental strength curves Figure 2.1.

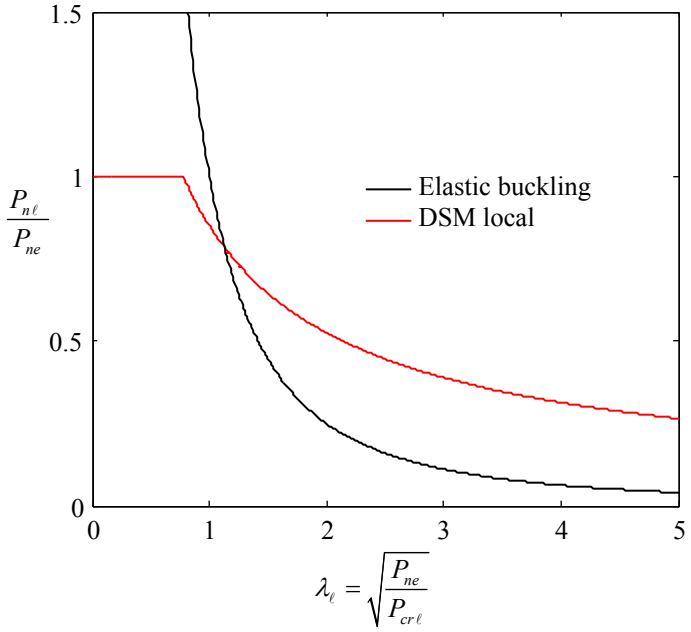

Figure 2.1: Comparison of the Direct Strength Method prediction curves with elastic buckling load for local buckling limit state: note that strength can be sufficiently higher than elastic buckling load, that is not the case for global buckling and hot-rolled steel member.

2.2 Perry-Robertson Method for Global Buckling

If only global buckling is under consideration, Perry-Robertson method as an analytical method is adopted for AISC Standard for hot-rolled steel (with necessary adjusting of parameters to best fit the experimental data). The method (i) uses one set of considerations for all of elastic buckling, inelastic buckling and yielding; (ii) adopts small displacement assumption for establishing a differential equation of equilibrium; (iii) assumes the column deforms in the shape of eigen-buckling solution which is a sine function; (3) the original derivation predicts the column failure occurs when the first fiber in the member reaches yielding point. The ultimate shape of the Perry-Robertson design curve depends on the choice of the magnitude of the initial imperfection. It is also worth noting according to Perry-Robertson

prediction the compacity is always lower than the elastic buckling load for global buckling, while for local buckling the capacity can be much higher than elastic buckling load as shown in the previous section.

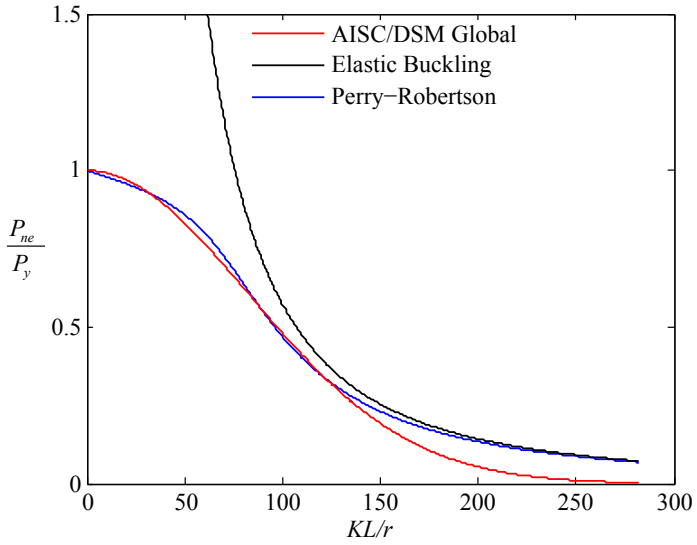

Figure 2.2: Perry-Robertson design curve for global buckling.

2.3 Use of Generalized Beam Theory in Direct Strength Method

GBT has been successfully used in conjunction with Standard Direct Strength Method. In DSM, experimental strength curves are used to link the elastic buckling loads with the capacity, as shown in Figure 2.1.

GBT is useful for Standards because it can easily calculate global, distortional and local buckling modes by including the corresponding modes in the analysis. Meanwhile, for a general elastic buckling analysis where all the modes are included, at the same time giving the elastic buckling load and shape, GBT identifies the modal participation of interest quantities such as displacement, stress, and strain energy. In these ways, a buckling solution is classified, which can then be used as input for DSM prediction for the corresponding limit-state.

Thin-walled members with holes cannot currently be treated by GBT. This causes practical difficulties for design, for example, the evaluation of isolated buckling loads and associated limit states that are needed for load-carrying capacity calculations. The results of this research, which include a method for applying GBT to members with perforations, have many applications for strength prediction of perforated members.

Often times, elastic buckling solutions are not generated by Generalized Beam Theory but by Finite Element Method using shell or solid elements. Before, modal identification of elastic buckling shapes or experimental point-clouds can be done by visual inspection. But it is subjective and tedious. To tackle that, several quantitative modal identification methods are brought out for decomposing the displacement fields, e.g., using GBT [77]. In this dissertation, the quantitative modal identification is extended to unit stress, strain energy and displacement. In this way, the modal participation information is more thorough and informative.

Currently, the load carrying capacities of thin-walled members are linked with elastic buckling load by empirical equations from regression analysis of experimental data. This method has limitations, e.g., the strength prediction for most interactive buckling limit states. The research in this dissertation facilitates interpretation of interactive buckling, which hopefully will lead to development of corresponding design methods.

Chapter 3

Literature Review of Thin-Walled Mechanics, Modal Participation Calculation Methods and Generalized Beam Theory

Thin-walled structural members exhibit fairly different behavior than that of non thin-walled members like hot-rolled steel - local buckling kicks in as the walls get sufficiently thin. Because local buckling has large strength reserve, thin-walled members have an attractive advantage of being able to take substantially larger load than elastic buckling load. It is essential to grasp the uniqueness of thin-walled structural members and thus thin-walled theories and analysis techniques are reviewed paving the groundwork for the original research presented later.

Modal participation calculation methods are also reviewed in this chapter. Because thin-walled members have more buckling limit states than member-wise global buckling, it is natural to intend to know the buckling mode participation for an elastic buckling solution. Modal participation can be used to identify local, distortional and global dominant buckling, and the very elastic bucking solution can be properly linked with corresponding buckling limit state using Direct Strength Method. For interactive buckling, e.g., where local buckling and distortional buckling are mixed, the Direct Strength Method has not been finalized for treating it. However, clearly a 90% local + 10% distortional buckling will behave differently that of a 10% local + 90% distortional. Based on that understanding, modal participation is used as input for this dissertation's research on interactive buckling.

Buckling modes associated with thin-walled behavior make Generalized Beam Theory an ideal analysis tool. The Global, Distortional and Local buckling modes are *inherent* in Generalized Beam Theory, making displaying modal participation extremely easy using GBT. Also, it is very convenient to get pure Gobal, Distortional, and Local buckling modes by

including only the modes of interest. These traits could have benefit over other analysis techniques like Finite Element Analysis (FEA) or Finite Strip Method (FSM). FEA and FSM need an extra step of modal decomposition to determine the contribution from each mode, while GBT solves for those directly. Also, FEA and FSM obtain isolated buckling modes by forming the whole stiffness matrix and then constrain the displacement field into the subspace of interest while GBT directly chooses the modes of interest and only forms the stiffness matrix for those modes without needing to impose any constraint. In addition, GBT is the main theory tool used in the research. GBT spent several decades to get where it is now that can analyze a variety of problems including geometric and material nonlinearities. The GBT literature and formulation are reviewed to understand the original work of this dissertation.

3.1 Thin-walled Theories and Analysis Techniques

The major characteristic of thin-walled members is the rigid cross-section assumption does not hold true. Some special aspects of thin-walled beams include:

- Plane sections no longer remain plane after deformation, and longitudinal warping does not conform to a linear distribution.
- For closed cross-sections, torsion is resisted by shear flow around the cross-section.
- Due to the shear lag effect, the area that is effective in resisting axial load may be less than the full net area.
- Cross-sectional distortion and local buckling may happen.

The most commonly utilized numerical techniques that counts for these effects and suitable for analyzing thin-walled beams are:

1. Shell Finite Element Method (SFEM). Shell elements are used to model structures in which one dimension, the thickness, is significantly smaller than the other dimensions. Conventional shell elements use this condition to discretize a body by defining the geometry at a reference surface. In this case the thickness is defined through the section property definition. Conventional shell elements have displacement and rotational degrees of freedom at the nodes. The displacement field inside the element domain is defined by using shape functions and nodal degrees of freedom. The advantage of SFEM is its general versatility for complex geometry and geometric/material nonlinear problems. The disadvantages include a large number of degrees of freedom and being purely numerical without mechanics insight. For more information, one may refer to [40, 69, 61, 57, 59, 119, 58].

2. Finite Strip Method (FSM). Finite strip method can be viewed as a special form of finite element method, where the thin-walled member is discretized into rectangular strips in the longitudinal direction of the beam. In many cases, finite strip method is more computationally efficient than shell finite element method. Finite strip method has several branches:

- Semi-Analytical Finite Strip Method. The classical finite strip method where the deflection of the strip is approximated as a combination of the sine harmonic series in the longitudinal direction and the polynomial function in the transverse direction. Originally the method is only applicable for simply-supported boundary conditions, e.g., [30], and later extended to general boundary conditions, e.g., [68].
- Spline Finite Strip Method. Compared to the previous method, the polynomial (spline) shape function is used to approximate the deflection in the longitudinal direction. One benefit is allowing analysis of non-standard boundary conditions and non-uniform internal forces and moments, e.g., [64, 42].
- Constrained Finite Strip Method (cFSM). cFSM add constraints on the displacement field of semi-analytical finite strip method, so that the pure buckling modes of global, distortional and local-plate buckling can be calculated, e.g., [6].

3. Generalized Beam Theory (GBT). Generalized Beam Theory (GBT) [90] is an enriched beam theory that analyzes thin-walled prismatic beams. It has the power to show the participation of global, distortional, and local modes explicitly for a general buckling problem. In the context of GBT, the cross-sectional modes are obtained by 'cross-section analysis', and the deformation at any cross-section is a linear combination of these modes.

3.2 Literature Review of Buckling Mode Decomposition Methods

The buckling phenomenon of open cross-section thin-walled structures is usually classified by three fundamental types: global (G) buckling; distortional (D) buckling; and local (L) buckling. These buckling mechanisms have different impacts on the post-buckling behavior: generally, global buckling has minimal post-buckling reserve, while cross-sectional modes like distortional buckling and local buckling have post-buckling capacity that can be utilized.

The Direct Strength Method, which is adopted in AISI-S100-12 [7] and the Australian/New Zealand Standard [56], predicts cold-formed steel member capacity with global (G), distortional (D), or local (L) buckling limit states using formulas with global or cross-sectional slenderness as input. As long as codes and standards treat G, D, and L modes separately,

proper buckling modal identification for both Finite Element (FE) Analysis and experiments is necessary. Modal identification can be exploited to quantitatively determine the nature of the buckling mode shape gained from FEA or test-based measurement, thus subjective and tedious visual inspection can be avoided. Modal identification is also helpful for research and code development, so that the failure mechanisms in FEA or experiments can be quantitatively categorized [67, 63].

There are two existing methods that perform modal identification. The constrained finite strip method (cFSM) treats the modal amplitude calculation as a least squares problem which minimizes the error between member-wise displacement fields and reconstructed displacement fields [5]. The motivation is to approximate any FEA displacement fields by the linear combination of the cFSM basis functions. The cFSM basis functions, which depend on the member length and boundary conditions, are obtained in advance. Another method is based on the Generalized Beam Theory (GBT) stiffness matrix [77, 78, 78]. This method solves linear equation systems for modal amplitudes at discrete cross-sections along the member. In the linear equation system, the coefficient matrix is the GBT stiffness matrix and the right-hand side vector is calculated by substituting the displacement fields from Finite Element Analysis (FEA) into GBT formulas for evaluating stiffness terms. Then modal participation factors can be evaluated using modal amplitudes along the member.

3.3 Literature Review of Generalized Beam Theory

Since the invention of generalized beam theory by Schardy in 1966, many researchers have contributed to its theoretical and applicative development. Nearly all of these efforts are made in Europe. This section reviews the GBT literature in the historical order.

3.3.1 Originality of Generalized Beam Theory, Schardt et al.

The inventor of GBT is Schardt from Technical University of Darmstadt in Germany. Since his first publications on this topic in 1966 and 1968 [88, 89], where first-order analysis for thin-walled bars with un-branched open or cylindrical cross-sections is covered, he and his research group continue to work on the project and wrote a textbook in 1989 [90]. During the period, these publications are mainly written in German, until the first English paper published in 1994 [87], and that is one of the reasons that GBT was not widely spread in English speaking academia. In his textbook, Schardt mentioned that he is inspired by Vlassov's effort to generalize the classical beam theory [90].

The first research using GBT in stability analysis is carried out by Schard in 1970 [86]. GBT formulation for closed cross-sections is developed by Möller in 1982 [76]. Shear lag effect and nonlinear warping is incorporated into GBT by Girmscheid in 1984 [43]. The methodology to add elastic constraints in the GBT analysis in order to tackle the stability of restrained

cold-formed purlins was found by Schardt and Schrade in 1989 [93]. GBT analysis for plates of several different boundary conditions was completed by Conchon in 2001 [31]. The post-buckling behavior of an unstiffened plate was studied analytically by GBT-based method by Schardt and C. Schardt in 2006 [92]. An full publication list of Schardt's research group from 1966 to 2001 can be found from http://www.vtb.info/.

3.3.2 Introduction of Generalized Beam Theory to English Speaking Academia, Davies et al.

Davies from the University of Manchester has made major contribution to the dissemination of GBT in the English speaking academic community. Davies group's focus is mainly on cold-formed steel. Leach, a Ph.D. student of Davies, published his dissertation on first and second-order GBT analysis of cold-formed members in 1989 [65]. In the dissertation, the GBT differential equation is solved by using finite difference method, and the analytical solution is verified against experiments. Another student of Davies, Jiang, carried out elastic and inelastic analysis of cold-formed columns, purlins and decking using GBT and finite element method [60, 33]. Jiang also made the suggestion that the design codes should account for distortional buckling for thin-walled members used in practice. Davies and Leach published two papers that introduced GBT first and second order analysis to the English speaking society [34, 35]. Also, Davies used GBT to study the buckling of perforated storage rack columns, where the the perforations are counted by empirical 'reduced thickness' method [70].

3.3.3 Study on distortional Buckling, closed cross-section of Generalized Beam Theory

- Lepistö, Halme et al.

Lepistö and others from the Lappeenranta University of Technology in Finland published a paper in 1996 and GBT was used to study the distortional buckling of C and Hat-section columns with intermediate and end stiffeners [66]. In the paper, the conclusion was reached that Eurocode 3 [41], the only Standard counting for distortional buckling at the time, was overly conservative in calculating critical buckling stress. Halme studied on the GBT static, buckling and dynamic analysis of thin plates [54]. Halme also proposed an alternative method for GBT cross-sectional analysis, in which an eigen frequency analysis of the cross-section is to be performed [55].

- Baláž and Rendek

Baláž and Rendek from the Slovak University of Technology utilized GBT to analyze the linear static behavior of open and closed cold-formed members [9]. Experimental study was also carried out [83], where it was shown that GBT is in good agreement with experiments. In 2002, they developed a code that performs GBT first order analysis on open and closed cross-section members [84].

- Simões da Silva and Simão

Simões da Silva and Simão from the University of Coimbra in Portugal, have done successful work on GBT theory and application on cold-formed steel. In 2002, Simões da Silva and Simão wrote a paper compared the GBT formulations for open and closed cross-section[81], in which Rayleigh-Ritz method was used to solve the governing differential equations. In 2003, they used GBT to study the post-buckling behavior of cold-formed columns with open [116] and closed [118] cross-section. In 2004, they published a journal article describing a unified energy formulation in the context of GBT for non-linear analysis of open and closed cross-sections [115]. In 2008, they studied the buckling behavior of Concerning hollow flange (HFB) beams and columns using GBT [117]. These outcome were summarized in Simão PhD dissertation written in English [114].

3.3.4 Development of Generalized Beam Theory for arbitrary cross-section, laminated composite beam and posting-buckling analysis, Camotim, Silvestre et al.

Professor Dinar Camotim and Professor Nuno Silvestre's research group from the Technical University of Lisbon in Portugal has been very (probably the most) active one on the research of GBT in recent years. Since their first journal articles in 2002 [104, 105], they have published more than a hundred papers. A summation of their research activities up to February, 2015 can be found at http://www.civil.ist.utl.pt/gbt/wp-content/uploads/2015/02/GBT-Bibliography.pdf.

Nuno Silvestre, now a professor at Technical University of Lisbon, completed fruitful Ph.D. research under Camotim. During his Ph.D., he developed GBT formulations for FRP composite and the shear warping modes [104, 111, 105]. His also used GBT deriving analytical formulas for the distortional buckling loads of cold-formed members with C, Z or rack-sections [109, 108, 110]. His work concerning steel include post-buckling analysis of GBT [113, 106]. He also published papers on the elastic buckling of circular tube [101], elliptical cross-section [102], and single-walled carbon nanotubes [103]. He revisited the basis of GBT and made a very clear explanation of GBT deformation modes [112].

Rodrigo Gonçalve, currently a professor at Universidade Nova de Lisboa, is another former Ph.D. student of Camotim who focused on developing elastic-plastic analysis scheme for GBT [45]. He used GBT to analyze the plastic bifurcation of aluminum and stainless steel

columns assuming Ramberg-Osgood and J2-plasiticity constitutive laws [48]. The work is later extended to general loading conditions [49]. He also developed the finite element formulation for the elastic buckling analysis of members subject to varying internal force resultants [47]. He extended GBT cross-sectional analysis from single-branch open cross-section to general cross-sections [51, 46]. Recently, he has published on the 1st-order analysis of steel-concrete composite bridges [50] and noval GBT cross-sectional analysis scheme [52].

Dinis worked with Gonçalve and expanded GBT cross-sectional analysis from single-branch open cross-section to open arbitrary branch cross-sections [38] and subsequently to general open and closed cross-sections [37]. More recently, he studied the coupled instabilities with distortional buckling in cold-formed steel lipped channel columns [29] and the mechanics of thin-walled angle column instability [39].

Cilmar Basaglia extended GBT to to analyze structural system, i.e., frames [16]. He developed 'joint elements' and compatibility conditions to connect individual members [10], and utilized it to study the local/global buckling [10, 12] and post-buckling [11] of both plane and spatial frames subject to general loading. He also investigated non-standard boundary conditions, i.e., fully or partially nodal restraints. Publications were achieved on the buckling [27] and post buckling [15] behavior for members under non-standard boundary conditions.

Silva who finished his Ph.D. study in 2013, focused on the GBT research of thin-walled laminated FRP composite members [80]. He investigated the influence of material couplings on the linear and buckling behavior of I-section composite columns [95], and the post-buckling behaviour [100]. He also studied buckling and post-buckling behavior of cylindrical stiffened panels [99], where a number of straight elements were used to approximate the geometric of shell instead of curved elements. Concerning experimental study, he compared the GBT with experimental results for the first-order, buckling and post-buckling behavior of pultruded I-section GRFP cantilevers [32, 98]. He also developed GBT formulation to capture load application and localized web buckling effects [97]. Last but not least Silva contributed to systematize the GBT cross-sectional analysis scheme for arbitrary open or closed cross-sections [96].

Bebiano is the main developer of the group's software GBTUL, which conducts GBT buckling and vibration analysis [22]. Before his Ph.D. he used GBT to study the buckling and post-buckling behavior of stiffened cold-formed steel columns [24]. His Ph.D. presented the development of new GBT formulations, expanding its applicability in the context of several relevant structural engineering problems including: buckling and ultimate strength, free vibration and dynamic response of thin-walled members [20]. He derived a GBT formulation to analyze the buckling behavior of thin-walled members subjected to non-uniform bending [19]. Recently, he completed a cross-section analysis procedure to rationalize and automate the performance of GBT-based structural analysis [18].

Miguel Abambres, Silvestre's Ph.D. student who graduated in 2014, focused on GBT formulations for elastoplastic first and second order (postbuckling) analysis, based on the J_2 theory with associated flow rule [4]. He had several papers published about geometric and material

nonlinear GBT analysis, e.g., [1, 3]. Recently, he studied GBT-based modal decomposition of elastic–plastic equilibrium configurations and collapse modes [2].

3.4 Generalized Beam Theory Formulations

This section introduces the Generalized Beam theory formulations for single branched isotropic members including shear-warping modes, for first and second-order analysis. The chapter starts with subsection 3.4.1, the establishment of governing equilibrium equations including constitutive laws, kinematics and Principal of Virtual Work in terms of GBT. subsection 3.4.2 covers GBT cross-sectional analysis where global, distortional, local and shear-warping modes can be found. subsection 3.4.3 tackles the solution techniques of the governing equation.

3.4.1 Components of Generalized Beam Theory

3.4.1.1 Kinematics of thin-walled member

Consider a single branched member with a thin-walled prismatic member as shown in Figure 3.1 with the global/local coordinates systems being $(X, Y, Z)/(x, s, z)$ and corresponding displacement components $(U, V, W)/(u, v, w)$.

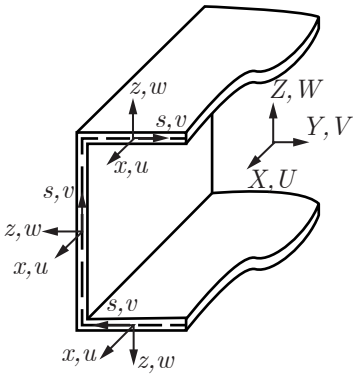

Figure 3.1: Coordinate system and translations for a thin-walled member

Kinematic assumptions GBT adopts Love-Kirchhoff hypotheses for plates:

- Straight lines normal to the mid-surface remain straight after deformation .

- Straight lines normal to the mid-surface remain normal to the mid-surface after deformation.
- The thickness of the plate does not change during a deformation.

For conventional GBT formulation [91], which corresponds to conventional GBT modes, Vlasov's null membrane strain assumption is adopted in addition:

- Transverse membrane normal and shear strains are negligible - $\varepsilon_{ss}^M = \gamma_{xs}^M = 0$,

where $(\cdot)^M$ stands for membrane term.

Kinematic relations Because of Love-Kirchhoff hypotheses, the displacement field of the continuum domain can be fully determined by the displacement field of the mid-surface plane, which corresponds to a two-dimensional mathematical model. This displacement of an arbitrary point $P(x, s, z)$ can be decomposed into the mid-surface displacement and an out-of-plane displacement, i.e.,

$$u(x,s,z) = u^M(x,s,z) + u^F(x,s,z) = u(x,s,0) - zw_{,x}(x,s,0), \tag{3.4.1}$$

$$v(x,s,z) = v^M(x,s,z) + v^F(x,s,z) = v(x,s,0) - zw_{,s}(x,s,0), \tag{3.4.2}$$

$$w(x,s,z) = w^M(x,s,z) = w(x,s,0) \tag{3.4.3}$$

where $(\cdot)^M$ denotes membrane terms and $(\cdot)^F$ denotes flexural terms, and standard summation notation applies; $(\cdot)_{,x} = d(\cdot)/dx$.

Strains including up to second-order terms are

$$\varepsilon_{ji} = \varepsilon_{ji}^L + \varepsilon_{ji}^{NL} = \frac{1}{2}(U_{j,i} + U_{i,j}) + \frac{1}{2}U_{j,i}U_{i,j}, \tag{3.4.4}$$

where $U_{(\cdot)}$ is displacement component which can refer to u, v or w according to the assigned coordinate system, and $(\cdot)^L, (\cdot)^{NL}$ refers to linear and nonlinear term respectively. Plugging Eq. (3.4.1)-Eq. (3.4.3) into Eq. (3.4.4), and recognizing $\varepsilon_{ss}^M = \gamma_{ss}^M = 0$, the strain components are

$$\varepsilon_{xx}^L = u_{,x} - zw_{,xx}, \tag{3.4.5}$$

$$\varepsilon_{ss}^{L} = 0 - zw_{,ss}, \tag{3.4.6}$$

$$\gamma_{xs}^{L} = 0 - 2zw_{,xs}, \tag{3.4.7}$$

$$\varepsilon_{xx}^{NL} = \frac{u_{,x}^2 + v_{,x}^2 + w_{,x}^2}{2}, \tag{3.4.8}$$

$$\gamma_{xs}^{NL} = u_{,s}u_{,x} + w_{,s}w_{,x} + v_{,s}v_{,x}. \tag{3.4.9}$$

In the circumstance of small strain and moderate rotation, the components $u_{,x}$, $u_{,s}$ are sufficiently smaller than $w_{,x}$, $w_{,s}$ or $v_{,x}$, $v_{,s}$ ([44]), and thus, Eq. (3.4.8) and Eq. (3.4.9) are rewritten as

$$\varepsilon_{xx}^{NL} = \frac{v_{,x}^2 + w_{,x}^2}{2}, \tag{3.4.10}$$

$$\gamma_{xs}^{NL} = w_{,s}w_{,x} + v_{,s}v_{,x}. \tag{3.4.11}$$

3.4.1.2 Constitutive law of thin-walled member

Constitutive law reads

$$\begin{Bmatrix} \sigma_{xx}^{M} \\ \sigma_{xx}^{F} \\ \sigma_{ss} \\ \tau_{xs} \end{Bmatrix} = \begin{bmatrix} E & 0 & 0 & 0 \\ 0 & \frac{E}{1-\nu^2} & \frac{\nu E}{1-\nu^2} & 0 \\ 0 & \frac{\nu E}{1-\nu^2} & \frac{E}{1-\nu^2} & 0 \\ 0 & 0 & 0 & G \end{bmatrix} \begin{Bmatrix} \varepsilon_{xx}^{M} \\ \varepsilon_{xx}^{F} \\ \varepsilon_{ss} \\ \gamma_{xs} \end{Bmatrix}, \tag{3.4.12}$$

where the membrane stress in the longitudinal direction is linked with the membrane strain by $\sigma_{xx}^{M} = E \cdot \varepsilon_{xx}^{M}$ instead of $\sigma_{xx}^{M} = \frac{E}{1-\nu^2} \cdot \varepsilon_{xx}^{M}$, in order to keep consistent with the 1D stress state in conventional beam theory.

3.4.1.3 Modal representation of the displacement field in Generalized Beam Theory

In the context of generalized beam theory, the displacement field for the cross-section at length x is a linear combination of GBT mode shapes

$$u(s,x) = u_k(s)\phi_{k,x}(x) + u_j\varphi_j(x) \qquad v(s,x) = v_k(s)\phi_k(x) \qquad w(s,x) = w_k(s)\phi_k(x), \quad (3.4.13)$$

where $u_k(s), v_k(s), w_k(s)$ are the functions specifying conventional GBT cross-sectional mode shapes; $u_j(s)$ is the function specifying the GBT shear mode shape; $\phi_k(x)$ is the modal amplitude vector of conventional GBT modes at length x along the member; $\varphi_j(x)$ is the modal amplitude vector of GBT shear modes at length x; $u_k(s)\phi_{k,x}(x)$ in the first term stands for warping from conventional GBT modes and is related to the first order derivatives of modal amplitudes, which can be proved by using Vlasov's null membrane strain assumption, i.e.,

$$\gamma_{xs}^M = 0 \quad \Leftrightarrow \quad v_{,x} = u_{,s} \quad . \quad (3.4.14)$$

Plugging Eq. (3.4.13) into Eq. (3.4.14) and including only the conventional modes, one has

$$v_k(s)\phi_{k,x}(x) = u_{k,s}(s)\phi_{k,x}(x) \quad \Leftrightarrow \quad v_k(s) = u_{k,s}(s). \quad (3.4.15)$$

So as long as the GBT mode shapes satisfy $v_k(s) = u_{k,s}(s)$, warping arises from conventional GBT modes can be written as related to the first order derivatives of modal amplitudes. For shear modes, in-plane cross-section displacements v and w are absent, and the warping is nonlinear along each fold line and Vlasov's assumption is not satisfied.

Substitute Eq. (3.4.13) into Eq. (3.4.5)-Eq. (3.4.11), the strains are

$$\varepsilon_{xx}^L = (u_k - zw_k)\phi_{k,xx} + u_j\varphi_{j,x}, \quad (3.4.16)$$

$$\varepsilon_{ss}^L = -zw_{k,ss}\phi_k, \quad (3.4.17)$$

$$\gamma_{xs}^L = (u_{k,s} + v_k)\phi_{k,x} - 2zw_{k,s}\phi_{k,x} + u_{j,s}\varphi_j \quad (3.4.18)$$

$$\varepsilon_{xx}^{NL} = v_i\phi_i v_k\phi_k + w_i\phi_i w_k\phi_k, \quad (3.4.19)$$

$$\gamma_{xs}^{NL} = w_{k,s}\phi_k w_i\phi_{i,x} + v_{k,s}\phi_k v_i\phi_{i,x}. \quad (3.4.20)$$

3.4.1.4 Establishment of governing equilibrium equations for Generalized Beam Theory

To acquire a differential equation system of equilibrium, the Principle of Virtual Work is utilized, i.e.,

$$\delta V = \delta U + \delta\Pi_\sigma + \delta\Pi = 0 \tag{3.4.21}$$

where δV is the variation in total potential energy, δU is the variation in elastic strain energy, $\delta\Pi_\sigma$ is the variation in the potential energy with respect to a pre-applied reference stress, and $\delta\Pi$ is the variation of potential energy with respect to the applied external force and traction.

Internal elastic strain energy The strain energy variation is given by

$$\begin{aligned}\delta U &= \int_L \int_B \int_t (\sigma_{xx}\delta\varepsilon_{xx} + \sigma_{ss}\delta\varepsilon_{ss} + \tau_{xs}\delta\gamma_{xs}) \\ &= \int_L \int_B \int_t (\sigma_{xx}^{L.M}\delta\varepsilon_{xx}^{L.M} + \sigma_{xx}^{L.F}\delta\varepsilon_{xx}^{L.F} + \sigma_{ss}^{L.F}\delta\varepsilon_{ss}^{L.F} + \tau_{xs}^{L.F}\delta\gamma_{xs}^{L.F})\end{aligned} \tag{3.4.22}$$

where the stresses can be obtained from substitution of Eq. (3.4.16)-Eq. (3.4.18) into Eq. (3.4.12), i.e.,

$$\sigma_{xx}^{L.M} = E(u_k\phi_k + u_j\varphi_{j,x}) \tag{3.4.23}$$

$$\sigma_{xx}^{L.F} = -z\frac{E}{1-\nu^2}[w_k\phi_{k,xx} + \nu w_{k,ss}\phi_k] \tag{3.4.24}$$

$$\sigma_{ss}^{L.F} = -z\frac{E}{1-\nu^2}[\nu w_k\phi_{k,xx} + w_{k,ss}\phi_k] \tag{3.4.25}$$

$$\tau_{xs}^{L.F} = -2zGw_{k,s}\phi_{k,x}. \tag{3.4.26}$$

Plugging Eq. (3.4.23)-Eq. (3.4.26) and Eq. (3.4.16)-Eq. (3.4.18) into Eq. (3.4.22), the internal strain energy reads

$$\begin{aligned}\delta U = \int_L (&C_{ik}\phi_{k,xx}\delta\phi_{i,xx} + C_{hk}\phi_{k,xx}\delta\varphi_{h,x} + C_{ij}\varphi_{j,x}\delta\phi_{i,xx} + C_{hj}\varphi_{j,x}\delta\varphi_{h,x} \\ &+ D^I_{ik}\phi_{k,x}\phi_{i,x} + D^I_{hj}\varphi_j\delta\varphi_h + D^{II}_{ik}\phi_k\delta\phi_{i,xx} + D^{II}_{ki}\phi_{k,xx}\delta\phi_i + B_{ik}\phi_k\delta\phi_i)dx\end{aligned} \tag{3.4.27}$$

Tensors denoted by C, D and X are calculated using GBT conventional and shear mode shapes, cross-sectional dimensions and material properties:

$$\begin{aligned} C_{ik} &= \int_b Etu_iu_kds + \int_b \frac{Et^3}{12(1-\nu^2)}w_iw_kds, & C_{ij} &= \int_b Eu_iu_jds, \\ D^I_{ik} &= \int_b \frac{Gt^3}{3}w_{i,s}w_{k,s}ds, & C_{hj} &= \int_b Eu_hu_jds, \\ D^{II}_{ik} &= \int_b \frac{\nu Et^3}{12(1-\nu^2)}w_iw_{k,ss}ds, & D^I_{hj} &= \int_b \frac{Et}{2(1+\nu)}u_{h,s}u_{j,s}ds, \\ B_{ik} &= \int_b \frac{t^3}{12(1-\nu^2)}w_{i,ss}w_{k,ss}ds, \end{aligned} \tag{3.4.28}$$

where subscripts i, k, p correspond to conventional GBT modes and h, j correspond to shear modes.

Potential energy with respect to pre-applied reference stress In the second-order analysis in this dissertation, cases where loads acting on the two ends of a member are of primary concern. Hence, the virtual work $\delta\Pi_\sigma$ done by the pre-applied reference stress considering only the contribution from normal stress is

$$\begin{aligned}\delta\Pi_\sigma &= \int_L\int_B\int_t \sigma^0_{xx}\delta\varepsilon^{NL}_{xx} \\ &= \int_L\int_B\int_t X_{mik}\phi_{i,x}\delta\phi_{k,x} + X^I_{mik}\phi_{k,xx}\delta\phi_{i,xx} \\ &+ X_{mjh}\varphi_{j,x}\delta\varphi_{h,x} + X_{mij}\varphi_{j,x}\delta\phi_{i,xx} + X_{mkh}\phi_{i,xx}\delta\varphi_{h,x}\end{aligned}, \tag{3.4.29}$$

where the third order tensors are defined

$$
\begin{aligned}
X_{mik} &= \int_b \sigma^0_{xx}(v_i v_k + w_i w_k)ds \\
X^I_{mik} &= \int_b \sigma^0_{xx} u_i u_k ds \\
X_{mjh} &= \int_b \sigma^0_{xx} u_j u_h ds, \\
X_{mij} &= \int_b \sigma^0_{xx} u_i u_j ds \\
X_{mkh} &= \int_b \sigma^0_{xx} u_k u_h ds
\end{aligned}
\tag{3.4.30}
$$

and X^I_{mik}, X_{mjh}, X_{mij}, X_{mkh}, can be neglected compared to X_{mik}, similar to the case in classical beam theory [44]. Now consider that the reference normal stress σ^0_{xx} stems from axial load, major/minor axis bending, and torsional warping bimoment:

$$
\sigma^0_{xx} = \frac{W^0_1}{C_{11}/E}u_1 + \frac{W^0_2}{C_{22}/E}u_2 + \frac{W^0_3}{C_{33}/E}u_3 + \frac{W^0_4}{C_{44}/E}u_4, \tag{3.4.31}
$$

where u_i is the i^{th} GBT mode shape (warping); W^0_p is the pre-buckling force resultant of axial load N ($p = 1$), major axis bending moment M_1 ($p = 2$), minor axis bending moment M_2 ($p = 3$), and torsional warping bimoment B ($p = 4$); and C_{pp}/E is the cross-sectional property of area ($p = 1$), major axis moment of inertia ($p = 2$), minor axis moment of inertia ($p = 3$), warping moment of inertia ($p = 4$). In this case Eq. (3.4.29) can be rewritten as:

$$
\delta\Pi_\sigma = \int_L \int_B \int_t \sigma^0_{xx}\delta\varepsilon^{NL}_{xx} = \int_L \int_B \int_t W^0_p X_{pik}\phi_{k,x}\delta\phi_{i,x}, \tag{3.4.32}
$$

where X_{pik} is a third order tensor defined by:

$$
X_{pik} == \int_b E\frac{u_p}{C_{pp}}(v_i v_k + w_i w_k)ds. \tag{3.4.33}
$$

Loading and external potential energy For the virtual work $\delta\Pi$ with respect to external force, consider traction q_x, q_s, and q_z along the local coordinate axes x, s, z (Figure 3.2) applied at the center line of thin plate. Under the variation of $\delta\phi_i$ and $\delta\varphi_k$:

$$
\delta\Pi = -\int_L \int_b (q_x\delta u + q_s\delta v + q_z\delta w)dsdx = -\int_L (q^I_i\delta\phi_i, x + q^I_h\delta\varphi_h + q^{II}_i\delta\phi_i)dx, \tag{3.4.34}
$$

where q_i^I, q_i^{II} are force vectors correspond to conventional modes and q_h^I to shear modes, they are:

$$q_i^I = \int_b q_x u_i ds \qquad q_i^{II} = \int_b (q_s v_i + q_z w_i) ds \qquad q_h^I = \int_b q_x u_h ds.$$

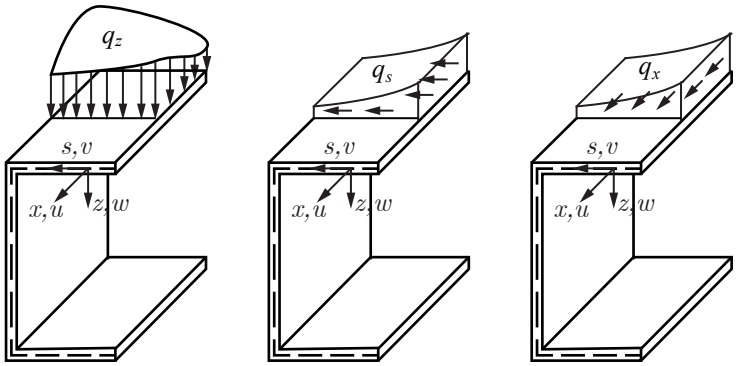

Figure 3.2: Distributed loading

3.4.1.5 Governing equilibrium equations for different analysis types in Generalized Beam Theory

Once δU and $\delta\Pi$ are obtained, the Principle of Virtual Work (δV) is exploited and differential equations system of equilibrium can be established as

$$\begin{aligned}(C_{ik}\frac{\partial^4}{\partial x^4} - D_{ik}\frac{\partial^2}{\partial x^2} + B_{ik} - W_p^0 X_{pik}\frac{\partial^2}{\partial x^2})\phi_k + C_{ij}\frac{\partial^3}{\partial x^3}\varphi_j = q_i^{II} - q_{i,x}^I,\\ C_{hk}\frac{\partial^3}{\partial x^3}\phi_k + (C_{ij}\frac{\partial^3}{\partial x^3} - D_{hj}^I)\varphi_j = -q_h^I.\end{aligned} \tag{3.4.35}$$

The boundary conditions are

$$\begin{aligned}W_i^\tau + q_x u_i + X_{mik} W_m^0 \phi_{k,x} = 0,\\ (W_i^\sigma + X_{mij} W_m^0 \varphi_{j,x})\delta\phi_{i,x}|_0^L = 0,\\ (W_h^\sigma + X_{mjh} W_m^0 \varphi_{j,x})\delta\varphi_h|_0^L = 0,\end{aligned} \tag{3.4.36}$$

where W_i^σ and W_i^σ are generalized normal force resultants corresponding to virtual displacement $\delta\phi_{i,x}$ (conventional modes) and $\delta\varphi_h$ (shear warping modes) respectively, reading

$$\begin{aligned} W_i^\sigma &= C_{ik}\phi_{k,xx} + D_{ik}^{II}\phi_k + C_{ij}\varphi_{j,x}, \\ W_h^\sigma &= C_{hk}\phi_{k,xx} + D_{hk}^{II}\phi_k + C_{hj}\varphi_{j,x}. \end{aligned} \tag{3.4.37}$$

W_i^τ in Eq. (3.4.36) are generalized shear force resultants on the other hand,

$$\begin{aligned} W_i^\tau &= -W_{i,x}^\sigma + W_i^{xs}, \\ W_i^{xs} &= D_{ik}^I\phi_{k,x}. \end{aligned} \tag{3.4.38}$$

Conventional modes analysis When GBT was formulated in the first place [91], mere conventional modes are included, in which Vlasov's assumption holds true. In many circumstances, conventional modes of analysis are acceptable, e.g., prismatic members subject to most loading situations, or even preferred if computational efficiency is considered. The governing differential equation of conventional modes analysis can be obtained through including only the corresponding terms in Eq. (3.4.35)

$$(C_{ik}\frac{\partial^4}{\partial x^4} - D_{ik}\frac{\partial^2}{\partial x^2} + B_{ik} - W_p^0 X_{pik}\frac{\partial^2}{\partial x^2})\phi_k = q_i^{II} - q_{i,x}^I, \tag{3.4.39}$$

with boundary condition

$$W_i^\tau + q_x u_i + X_{mik}W_m^0\phi_{k,x} = 0 W_i^\sigma \delta\phi_{i,x}|_0^L = 0 \quad , \tag{3.4.40}$$

$$W_i^\sigma = C_{ik}\phi_{k,xx} + D_{ik}^{II}\phi_k, \tag{3.4.41}$$

in which

$$\begin{aligned} W_i^\tau &= -W_{i,x}^\sigma + W_i^{xs}, \\ W_i^{xs} &= D_{ik}^I\phi_{k,x}. \end{aligned} \tag{3.4.42}$$

3.4.2 Cross-section analysis of Single Branched Cross-Sections

GBT cross-section analysis generates the mode shapes $u_k(s), v_k(s), w_k(s)$. This section introduces GBT cross-section analysis for single-branch open cross-section. For multi-branch cross-section, one may refer to [38], [37]. For a systematic approach for arbitrary cross-section, one may refer to [18].

3.4.2.1 Generation of GBT conventional modes

For conventional modes, Vlasov's assumption ($\varepsilon_{ss}^M = \gamma_{xs}^M = 0$) applies, and three components of a GBT mode $u_k(s), v_k(s), w_k(s)$ are not independent but subject to kinematic constraints. The goal here is to find conventional modes that simultaneously diagonalize GBT matrices C, B in Eq. (3.4.39). Recall

$$\begin{aligned} C_{ik} &= \int_b E u_i u_k ds + \int_b \frac{Et^3}{12(1-\nu^2)} w_i w_k ds, \\ B_{ik} &= \int_b \frac{t^3}{12(1-\nu^2)} w_{i,ss} w_{k,ss} ds, \end{aligned} \tag{3.4.43}$$

and the approach is to: first calculate the displacement field $u_i^0(s), v_i^0(s), w_i^0(s)$ for *elementary modes* and associated C^0, B^0; and second find the linear combinations of *preliminary modes* that simultaneously diagonalize C, B, which will be the modes needed. The approach described herein for calculating $u_i^0(s), v_i^0(s), w_i^0(s)$ is based on [91] and is essentially a *force method*. For more complex shape like multi-branch cross-section, *displacement method* can be more convenient like in [52].

There are three types of nodes in cross-section analysis, namely natural nodes that are intersections of plates, intermediate nodes that are in between natural nodes, end nodes that are two in open-branch cross-section and should be counted as both natural and intermediate node.

Degrees of freedom of cross-section analysis are warping u at the natural nodes and the lateral deflection w at intermediate nodes. All the other displacement components can be derived from these DOFs because of the enforcement of Vlasov's assumption and the shape functions described later.

Preliminary warping modes This section describes the approach to calculate $u(s)$, $v(s)$, $v(s)$ when warping are enforced at natural nodes. The warping function $u(s)$ is interpolated linear in between natural nodes, and thus the warping on any fold line r with natural coordinate s can be written as

$$u_r(s) = \frac{s_{r+1} - s}{b_r} u_r + \frac{s - s_r}{b_r} u_{r+1}, \tag{3.4.44}$$

where $u_r(s)$ stands for the warping on fold line r and u_r stands for the warping at the r^{th}natural node. In the matrix form, one has

$$\mathbf{u_s} = \mathbf{Uu} \Leftrightarrow \begin{Bmatrix} u_1 \\ \cdots \\ u_r \\ \cdots \\ u_n \end{Bmatrix} = \begin{bmatrix} \frac{s_2-s}{b_1} & \frac{s-s_1}{b_1} & 0 & 0 & 0 & 0 \\ 0 & \cdots & \cdots & 0 & 0 & 0 \\ 0 & 0 & \frac{s_{r+1}-s}{b_r} & \frac{s-s_r}{b_r} & 0 & 0 \\ 0 & 0 & 0 & \cdots & \cdots & 0 \\ 0 & 0 & 0 & 0 & \frac{s_{n+1}-s}{b_n} & \frac{s-s_n}{b_n} \end{bmatrix} \begin{Bmatrix} u_1 \\ u_2 \\ \cdots \\ u_r \\ u_{r+1} \\ \cdots \\ u_n \\ u_{n+1} \end{Bmatrix}. \tag{3.4.45}$$

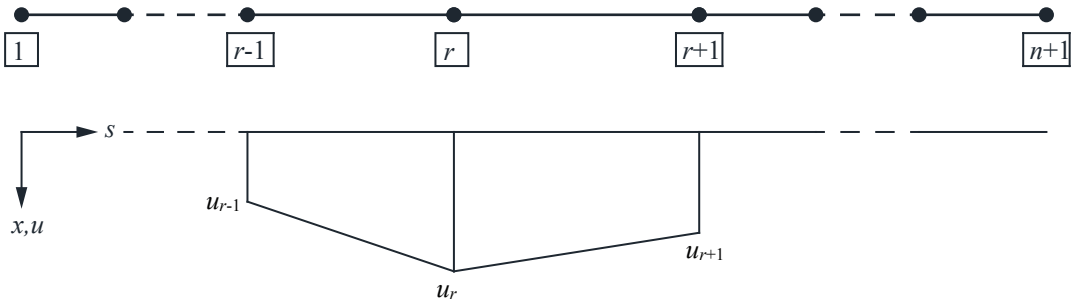

Figure 3.3: Shape function of $u(s)$

For the v part, substituting Eq. (3.4.44) into Eq. (3.4.15), there is

$$v_r = \frac{s_{r+1} - s}{b_r} u_r, \tag{3.4.46}$$

where v_r stands for the v displacement in r^{th}fold line and is a constant. Eq. (3.4.46) is written in the matrix form

$$\mathbf{v_s} = \mathbf{Vu} \Leftrightarrow \begin{Bmatrix} v_1 \\ \cdots \\ v_r \\ \cdots \\ v_n \end{Bmatrix} = \begin{bmatrix} \frac{1}{b_1} & -\frac{1}{b_1} & 0 & 0 & 0 & 0 \\ 0 & \cdots & \cdots & 0 & 0 & 0 \\ 0 & 0 & \frac{1}{b_r} & -\frac{1}{b_r} & 0 & 0 \\ 0 & 0 & 0 & \cdots & \cdots & 0 \\ 0 & 0 & 0 & 0 & \frac{1}{b_n} & -\frac{1}{b_n} \end{bmatrix} \begin{Bmatrix} u_1 \\ u_2 \\ \cdots \\ u_r \\ u_{r+1} \\ \cdots \\ u_n \\ u_{n+1} \end{Bmatrix}. \tag{3.4.47}$$

The remaining part is flexural component $w(s)$. Single branch cross-section is viewed as a continuous beam subject to forced displacements or support settlements. The displacement

field is solved using *force method* and the unknown forces are chosen as the moment at the supports as shown in Figure 3.4.

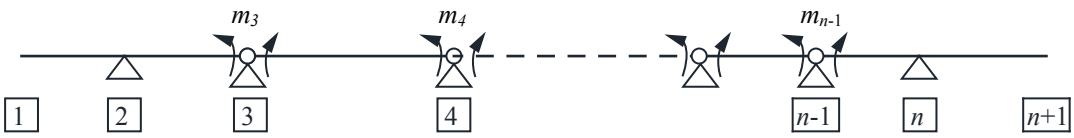

Figure 3.4: Basic system of force method for solving of $w(s)$

When $v(s)$ is enforced because of Eq. (3.4.47), the flexural component $w(s)$ will be present as well because of the kinematical constraint described in Figure 3.5.

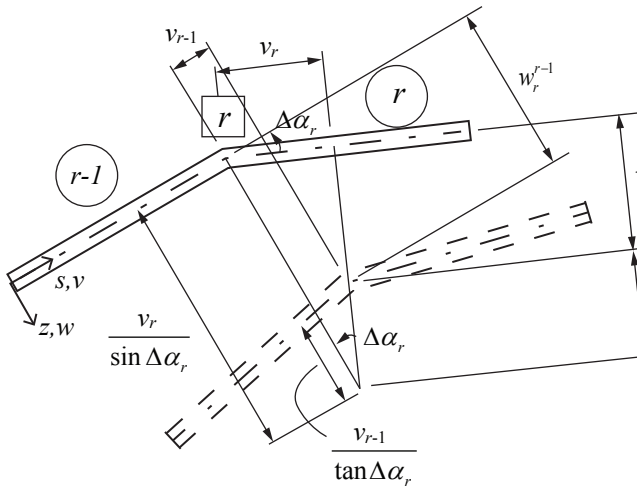

Figure 3.5: w displacement of natural node because the enforcement of v

$$\Delta\alpha_r = \alpha_{r-1} - \alpha_r \quad (2 \le r \le n) \tag{3.4.48}$$

Because of the kinematics in Figure 3.5, it can be calculated that

$$\begin{aligned} w_r^s &= \frac{v_r}{tan\Delta\alpha_r} - \frac{v_{r-1}}{sin\Delta\alpha_r} \quad (r \ge 2) \\ w_{r-1}^e &= \frac{v_r}{sin\Delta\alpha_r} - \frac{v_{r-1}}{tan\Delta\alpha_r} \quad (r \le n) \end{aligned}, \tag{3.4.49}$$

where w_r^s stands for w of the starting point of r^{th} fold line and w_{r-1}^e for w of the starting point of r^{th} fold line. They are describing the displacement of the same point. But because the

point is the intersection of two fold lines, there are two equations. Introducing Eq. (3.4.44) into Eq. (3.4.49), one has

$$\begin{aligned} w_r^s &= -\frac{1}{b_{r-1}sin\Delta\alpha_r}u_{r-1} + (\frac{1}{b_{r-1}sin\Delta\alpha_r} + \frac{1}{b_r tan\Delta\alpha_r})u_r - \frac{1}{b_r tan\Delta\alpha_r}u_{r+1} \\ w_r^e &= -\frac{1}{b_r tan\Delta\alpha_{r+1}}u_r + (\frac{1}{b_r tan\Delta\alpha_{r+1}} + \frac{1}{b_{r+1}sin\Delta\alpha_{r+1}})u_{r+1} - \frac{1}{b_{r+1}sin\Delta\alpha_{r+1}}u_{r+2} \end{aligned}, \tag{3.4.50}$$

in the matrix form

$$\mathbf{w^s} = \mathbf{W^s u} \Leftrightarrow \begin{Bmatrix} w_1^s \\ w_2^s \\ \cdots \\ w_r^s \\ \cdots \\ w_n^s \end{Bmatrix} =$$

$$\begin{bmatrix} 0 & 0 & 0 & 0 & 0 & 0 & 0 & 0 & 0 \\ \mathrm{W}^{\mathrm{S}}_{(2.1)} & \mathrm{W}^{\mathrm{S}}_{(2.2)} & \mathrm{W}^{\mathrm{S}}_{(2.3)} & 0 & 0 & 0 & 0 & 0 & 0 \\ 0 & \cdots & \cdots & \cdots & \cdots & 0 & 0 & 0 & 0 \\ 0 & 0 & 0 & \mathrm{W}^{\mathrm{S}}_{(\mathrm{r.r-1})} & \mathrm{W}^{\mathrm{S}}_{(\mathrm{r.r})} & \mathrm{W}^{\mathrm{S}}_{(\mathrm{r.r+1})} & 0 & 0 & 0 \\ 0 & 0 & 0 & 0 & \cdots & \cdots & \cdots & \cdots & 0 \\ 0 & 0 & 0 & 0 & 0 & 0 & \mathrm{W}^{\mathrm{S}}_{(\mathrm{n.n-1})} & \mathrm{W}^{\mathrm{S}}_{(\mathrm{n.n})} & \mathrm{W}^{\mathrm{S}}_{(\mathrm{n.n+1})} \end{bmatrix} \begin{Bmatrix} u_1 \\ u_2 \\ u_3 \\ \cdots \\ u_{r-1} \\ u_r \\ u_{r+1} \\ \cdots \\ u_{n-1} \\ u_n \\ u_{n+1} \end{Bmatrix}, \tag{3.4.51}$$

$$\mathbf{w^s}= \mathbf{W^e u} \Leftrightarrow \left\{ \begin{array}{c} w_1^e \\ \cdots \\ w_r^e \\ \cdots \\ w_{n-1}^e \\ w_n^e \end{array} \right\} =$$

$$\begin{bmatrix} \mathrm{W}^{\mathrm{e}}_{(1.1)} & \mathrm{W}^{\mathrm{e}}_{(1.2)} & \mathrm{W}^{\mathrm{e}}_{(1.3)} & 0 & 0 & 0 & 0 & 0 & 0 \\ 0 & \cdots & \cdots & \cdots & \cdots & 0 & 0 & 0 & 0 \\ 0 & 0 & 0 & \mathrm{W}^{\mathrm{e}}_{(\mathrm{r.r})} & \mathrm{W}^{\mathrm{e}}_{(\mathrm{r.r+1})} & \mathrm{W}^{\mathrm{e}}_{(\mathrm{r.r+2})} & 0 & 0 & 0 \\ 0 & 0 & 0 & 0 & \cdots & \cdots & \cdots & \cdots & 0 \\ 0 & 0 & 0 & 0 & 0 & 0 & \mathrm{W}^{\mathrm{e}}_{(\mathrm{n-1.n-1})} & \mathrm{W}^{\mathrm{e}}_{(\mathrm{n-1.n})} & \mathrm{W}^{\mathrm{e}}_{(\mathrm{n-1.n+1})} \\ 0 & 0 & 0 & 0 & 0 & 0 & 0 & 0 & 0 \end{bmatrix} \left\{ \begin{array}{c} u_1 \\ u_2 \\ u_3 \\ \cdots \\ u_r \\ u_{r+1} \\ u_{r+2} \\ \cdots \\ u_{n-1} \\ u_n \\ u_{n+1} \end{array} \right\}, \tag{3.4.52}$$

where

$$\begin{array}{lll} \mathrm{W}^{\mathrm{S}}_{(\mathrm{r.r-1})} = -\dfrac{1}{b_{r-1} sin\Delta\alpha_r} & \mathrm{W}^{S}_{(r.r)} = \dfrac{1}{b_{r-1} sin\Delta\alpha_r} + \dfrac{1}{b_r tan\Delta\alpha_r} & \mathrm{W}^{S}_{(r.r+1)} = -\dfrac{1}{b_r tan\Delta\alpha_r} \\ \mathrm{W}^{\mathrm{e}}_{(\mathrm{r.r})} = -\dfrac{1}{b_r tan\Delta\alpha_{r+1}} & \mathrm{W}^{e}_{(r.r+1)} = \dfrac{1}{b_r tan\Delta\alpha_{r+1}} + \dfrac{1}{b_{r+1} sin\Delta\alpha_{r+1}} & \mathrm{W}^{e}_{(r.r+2)} = -\dfrac{1}{b_{r+1} sin\Delta\alpha_{r+1}} \end{array}. \tag{3.4.53}$$

The first row of Eq. (3.4.51) and the last row of Eq. (3.4.52) consists of zeros because the w of the start and end point of the cross-section are degrees-of-freedom determined differently. Knowing the w of two end points of each fold line, w of the mid point of fold line is

$$\hat{w}_r = \frac{w_r^s + w_r^e}{2}, \tag{3.4.54}$$

in the matrix form

$$\hat{\mathbf{w}} = \frac{1}{2}(\mathbf{w^s} + \mathbf{w^e}). \tag{3.4.55}$$

Introducing Eq. (3.4.51), Eq. (3.4.52) into Eq. (3.4.55), there is

$$\hat{\mathbf{w}} = \frac{1}{2}(\mathbf{W^s} + \mathbf{W^e})\mathbf{u} = \hat{\mathbf{W}}\mathbf{u}. \tag{3.4.56}$$

On the other hand, the rotation of the r^{th} plate can be calculated as

$$\varphi_r = \frac{w_r^e - w_r^s}{b_r}. \tag{3.4.57}$$

By considering Eq. (3.4.51) and Eq. (3.4.52), Eq. (3.4.57) can be written in the matrix form

$$\boldsymbol{\varphi} = \boldsymbol{\Phi}\mathbf{u}. \tag{3.4.58}$$

Knowing φ, the relative rotation between two adjacent plates is

$$\Delta\varphi_r = \varphi_r - \varphi_{r-1} = \frac{w_r^e - w_r^s}{b_r} - \frac{w_{r-1}^e - w_{r-1}^s}{b_{r-1}}. \tag{3.4.59}$$

And likewise, it can be written in the matrix form

$$\Delta\boldsymbol{\varphi} = \Delta\boldsymbol{\Phi}\mathbf{u}. \tag{3.4.60}$$

Then the relationship between the distribution of the transverse moment along the cross-section and the support moments. Because the transverse deflection is assumed to be Hermitian cubic function, the transverse moment varies linearly in each plate

$$\mathbf{m_p} = \mathbf{M_s}\mathbf{m} \Leftrightarrow \begin{Bmatrix} m_1 \\ m_2 \\ \cdots \\ m_r \\ \cdots \\ m_{n-1} \\ m_n \end{Bmatrix} = \begin{bmatrix} 0 & \frac{s-s_1}{b_1} & 0 & 0 & 0 & 0 & 0 & 0 \\ 0 & \frac{s_3-s}{b_2} & \frac{s-s_2}{b_2} & 0 & 0 & 0 & 0 & 0 \\ 0 & 0 & \cdots & \cdots & 0 & 0 & 0 & 0 \\ 0 & 0 & 0 & \frac{s_{r+1}-s}{b_r} & \frac{s-s_r}{b_r} & 0 & 0 & 0 \\ 0 & 0 & 0 & 0 & \cdots & \cdots & 0 & 0 \\ 0 & 0 & 0 & 0 & 0 & \frac{s_n-s}{b_{n-1}} & \frac{s-s_{n-1}}{b_{n-1}} & 0 \\ 0 & 0 & 0 & 0 & 0 & 0 & \frac{s_{n+1}-s}{b_{n+1}} & 0 \end{bmatrix} \begin{Bmatrix} m_1 \\ m_2 \\ \cdots \\ m_r \\ m_{r+1} \\ \cdots \\ m_n \\ m_{n+1} \end{Bmatrix}. \tag{3.4.61}$$

Assign matrix $\mathbf{k}$, whose components contain the transverse flexural rigidity of every plate,

$$\mathbf{k} = \begin{bmatrix} K_1 & 0 & 0 & 0 & 0 \\ 0 & \cdots & 0 & 0 & 0 \\ 0 & 0 & K_r & 0 & 0 \\ 0 & 0 & 0 & \cdots & 0 \\ 0 & 0 & 0 & 0 & K_n \end{bmatrix}, \tag{3.4.62}$$

where $K_r = Et_r^3/12(1-\nu^2)$. And the flexibility matrix can be found as

$$\mathrm{F} = \int_b \mathrm{M_s^T k^{-1} M_s} ds, \tag{3.4.63}$$

and by doing the integral

$$\mathrm{F} = \begin{bmatrix} 1 & 0 & 0 & 0 & 0 & 0 & 0 & 0 & 0 \\ 0 & \frac{b_1}{3K_1}+\frac{b_2}{3K_2} & \frac{b_2}{6K_2} & 0 & 0 & 0 & 0 & 0 & 0 \\ 0 & \frac{b_2}{6K_2} & \frac{b_2}{3K_2}+\frac{b_3}{3K_3} & \frac{b_3}{6K_3} & 0 & 0 & 0 & 0 & 0 \\ 0 & 0 & \cdots & \cdots & \cdots & 0 & 0 & 0 & 0 \\ 0 & 0 & 0 & \frac{b_{r-1}}{6K_{r-1}} & \frac{b_{r-1}}{3K_{r-1}}+\frac{b_r}{3K_r} & \frac{b_r}{6K_r} & 0 & 0 & 0 \\ 0 & 0 & 0 & 0 & \cdots & \cdots & \cdots & 0 & 0 \\ 0 & 0 & 0 & 0 & 0 & \frac{b_{n-2}}{6K_{n-2}} & \frac{b_{n-2}}{3K_{n-2}}+\frac{b_{n-1}}{3K_{n-1}} & \frac{b_{n-1}}{6K_{n-1}} & 0 \\ 0 & 0 & 0 & 0 & 0 & 0 & \frac{b_{n-1}}{6K_{n-1}} & \frac{b_{n-1}}{3K_{n-1}}+\frac{b_n}{3K_n} & 0 \\ 0 & 0 & 0 & 0 & 0 & 0 & 0 & 0 & 1 \end{bmatrix}. \tag{3.4.64}$$

Then the stiffness matrix can be found by finding the inverse of the flexibility matrix,

$$\mathrm{K} = \mathrm{F}^{-1}, \tag{3.4.65}$$

and the unknowns of the support moments can be found,

$$\mathrm{M} = -\mathrm{K} \cdot \Delta\mathbf{\Phi}. \tag{3.4.66}$$

Up to this point, all the values one needs to determine the deflection function in the r^{th} plate when a unit warping is imposed at node k can be calculated,

$$\mathbf{W_{(r,k)}} = \hat{\mathbf{W}}_{\mathbf{(r,k)}}\eta_1 + \frac{b_r}{2}\mathbf{\Phi_{(r,k)}}\eta_2 - \frac{b_r^2}{3K_r}\mathbf{M_{(r,k)}}\eta_3 - \frac{b_r^2}{3K_r}\mathbf{M_{(r+1,k)}}\eta_4, \tag{3.4.67}$$

where $\eta_1 - \eta_4$ are shape functions in Eq. (3.4.68) and graphically depicted in Figure 3.6

$$\begin{aligned} \eta_1 &= 1 & \eta_2 &= 2(\frac{s-s_r}{b_r}) - 1 \\ \eta_3 &= -\frac{s-s_r}{b_r} + \frac{3}{2}(\frac{s-s_r}{b_r})^2 - \frac{1}{2}(\frac{s-s_r}{b_r})^3 & \eta_4 &= \frac{1}{2}(\frac{s-s_r}{b_r}) + \frac{1}{2}(\frac{s-s_r}{b_r})^3 \end{aligned}. \tag{3.4.68}$$

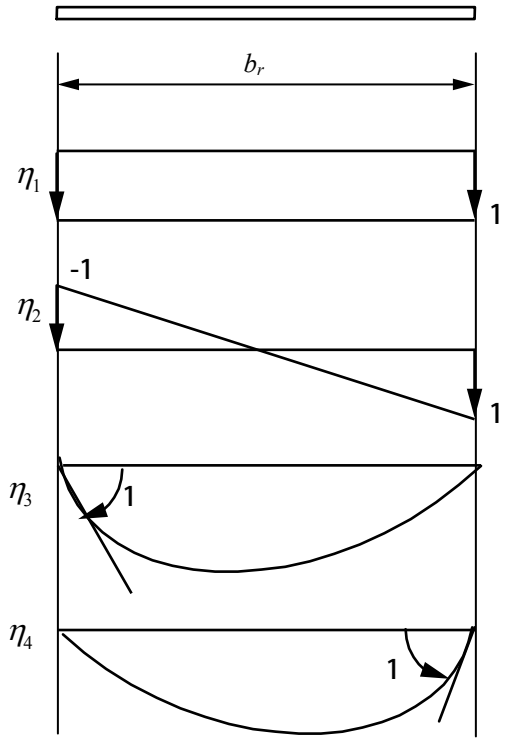

Figure 3.6: Shape functions for w in the cross-section analysis

Eq. (3.4.67) can be written in the matrix form, and $w(s)$ can be found with forced $\mathbf{u}$,

$$\mathbf{w_s} = \mathbf{Wu}. \tag{3.4.69}$$

Preliminary local-plate modes Local-plate modes are those whose warping and shifting components u, v are null but only the transverse displacement w is present. The number of local-plate modes are equivalent to the number of *intermediate nodes* one uses to discretize the cross-section.

Essentially, the displacement field of a preliminary local mode is associated with the forced displacement $w = 1$ of an intermediate node and displacement along the member $w(s)$, which

can be solved by any structural method one prefers. If the approach in [91] is followed, the $w(s)$ is solved by using *force method*, and as follows.

1. Release the rotational degrees at the supports, and make the support moments unknowns.
2. Apply unit displacements at intermediate nodes, and keep natural nodes unmoved.
3. Solve for the unknown support moments per *force method,* and obtain the displacement field.

The method is essentially the same as in preliminary warping modes, and thus will not be explained in detail.

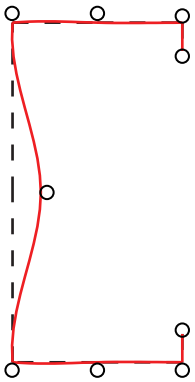

Figure 3.7: Preliminary local-plate mode

Determination of conventional modes The degrees of freedom of cross-section analysis are warping of the natural nodes and transverse displacement of the intermediate nodes, e.g., for the following cross-section (Figure 3.8)

$$y = \begin{Bmatrix} w_1 & u_2 & u_3 & w_4 & u_5 & w_6 & u_7 & w_8 & u_9 & u_{10} & w_{11} \end{Bmatrix}^T. \tag{3.4.70}$$

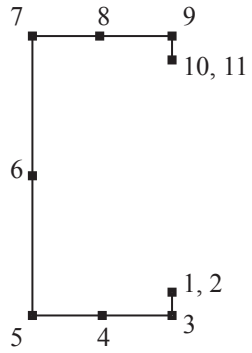

Figure 3.8: Example cross-section

Using the method described in preliminary warping and local-plate modes, the displacement field $u(s), v(s), w(s)$ can be determined upon any forced displacement in y. And the GBT tensors corresponding to preliminary modes can be calculated per Eq. (3.4.28) and Eq. (3.4.33). The conventional modes are obtained by a simultaneous diagonization process consisting of three steps:

1. Eigen problem $(\mathbf{B} - \lambda_k \mathbf{C})\mathbf{y}_k$=0, which yields

- $\lambda_k = 0 (k = 1 \sim 4)$ corresponds to rigid body modes, but the modes of axial, bending, twisting modes have to be found in next steps;
- $\lambda_k > 0 (k = 5 \sim n + 1)$ corresponds to distortional modes where both warping $u_k(s)$ and in-plane components are present $v_k(s), w_k(s)$, and n is number of fold-lines;
- $\lambda_k > 0 (k = n + 2 \sim n + m + 3)$ corresponds to local modes where $u_k(s), w_k(s)$ are null but only $w_k(s)$ is present, and m stands for number of intermediate nodes.

Accordingly, the resulted eigen-vectors are

$$\mathbf{Y}^I = \begin{bmatrix} y_1^I & \cdots & y_4^I & y_5^I & \cdots & y_{n+1}^I & y_{n+2}^I & \cdots & y_{n+m+3}^I \end{bmatrix}, \tag{3.4.71}$$

and

$$\mathbf{C}^I = \begin{bmatrix} \mathbf{y}_1^I & \cdots & \mathbf{y}_4^I \end{bmatrix}^T \mathbf{C} \begin{bmatrix} \mathbf{y}_1^I & \cdots & \mathbf{y}_4^I \end{bmatrix} \quad \mathbf{D}^I = \begin{bmatrix} \mathbf{y}_1^I & \cdots & \mathbf{y}_4^I \end{bmatrix}^T \mathbf{D} \begin{bmatrix} \mathbf{y}_1^I & \cdots & \mathbf{y}_4^I \end{bmatrix} \quad . \tag{3.4.72}$$

2. Torsion mode is found through eigen problem

$$(\mathbf{D}^I - \lambda_k \mathbf{C}^I)\mathbf{y}_k = 0, \tag{3.4.73}$$

where

- $\lambda_k = 0 (k = 1 \sim 3)$ corresponds to the linear space consisting of axial, strong axis bending and weak axis bending modes;
- $\lambda_k > 0 (k = 4)$ corresponds to the tortion mode.

The resulted eigen vectors are

$$\mathbf{Y} = \begin{bmatrix} \mathbf{y}_1 & \mathbf{y}_2 & \mathbf{y}_3 & \mathbf{y}_4 \end{bmatrix}, \tag{3.4.74}$$

and the GBT modes obtained from this step are

$$\mathbf{Y}^{II} = \mathbf{Y}^I \mathbf{Y} = \begin{bmatrix} \mathbf{y}_1^{II} & \mathbf{y}_2^{II} & \mathbf{y}_3^{II} & \mathbf{y}_4^{II} \end{bmatrix}, \tag{3.4.75}$$

where $\mathbf{y}_4^{II}$ denotes the torsion mode. Let

$$\mathbf{C}^{II} = \begin{bmatrix} \mathbf{y}_1^{II} & \cdots & \mathbf{y}_3^{II} \end{bmatrix}^T \mathbf{C} \begin{bmatrix} \mathbf{y}_1^{II} & \cdots & \mathbf{y}_3^{II} \end{bmatrix} \quad \mathbf{X}^{II} = \begin{bmatrix} \mathbf{y}_1^{II} & \cdots & \mathbf{y}_3^{II} \end{bmatrix}^T \mathbf{X} \begin{bmatrix} \mathbf{y}_1^{II} & \cdots & \mathbf{y}_3^{II} \end{bmatrix}, \tag{3.4.76}$$

and the axial mode and bending modes can be found by next step.

1. The axial mode and two bending modes are found by

$$(\mathbf{X}^{II} - \lambda_k \mathbf{C}^{II})\mathbf{y}_k = 0, \tag{3.4.77}$$

which yields

- $\lambda_1 = 0$ corresponds to mode of axial compression;
- $\lambda_2 > \lambda_3 > 0$ correspond to modes of strong and weak axis bending.

The resulted eigen vectors are

$$\mathbf{Y} = \begin{bmatrix} \mathbf{y}_1 & \mathbf{y}_2 & \mathbf{y}_3 \end{bmatrix}, \tag{3.4.78}$$

and the GBT modes obtained from this step are

$$\mathbf{Y}^{II} = \mathbf{Y}^{II} \mathbf{Y} = \begin{bmatrix} \mathbf{y}_1^{II} & \mathbf{y}_2^{II} & \mathbf{y}_3^{II} \end{bmatrix}. \tag{3.4.79}$$

3.4.2.2 Generation of GBT shear-warping modes

Shear-warping modes have warping u present and in-plane components v, w absent. The shape function is chosen to be linear function between discretization nodes (regardless of natural or intermediate node). Thus the preliminary shear-warping mode consists of Kronecker-delta function where warping is unity at one node and null at all others, as shown in Figure 3.9. The final shear-warping modes are found by simultaneously diagonizing matrix C_{hj}, D_{hj}, in Eq. (3.4.28),

$$\begin{aligned} C_{hj} &= \int_b E u_h u_j ds, \\ D_{hj} &= \int_b \frac{Et}{2(1+\nu)} u_{h,s} u_{j,s} ds \end{aligned} . \tag{3.4.80}$$

The eigen problem reads

$$(\mathbf{D_s} - \lambda_j \mathbf{C_s})\mathbf{y_j} = \mathbf{0}, \tag{3.4.81}$$

which yields $n + m + 1$ eigen pairs (n stands for number of plates; m stands for number of intermediate nodes) corresponding to:

- $\lambda_1 > \lambda_j > 0 (j = 2 \sim n + m + 1)$ corresponds to uniform compression, and can be discarded

$$\tilde{\mathbf{y}}_1 = \begin{Bmatrix} 1 & 1 & \cdots & 1 \end{Bmatrix}^T; \tag{3.4.82}$$

- $\lambda_j > 0 (j = 2 \sim n + m + 1)$ corresponds to shear-warping modes,

$$\tilde{\mathbf{y}}_1 = \begin{Bmatrix} \tilde{u}_1 & \tilde{u}_2 & \cdots & \tilde{u}_{n+m+1} \end{Bmatrix}^T. \tag{3.4.83}$$

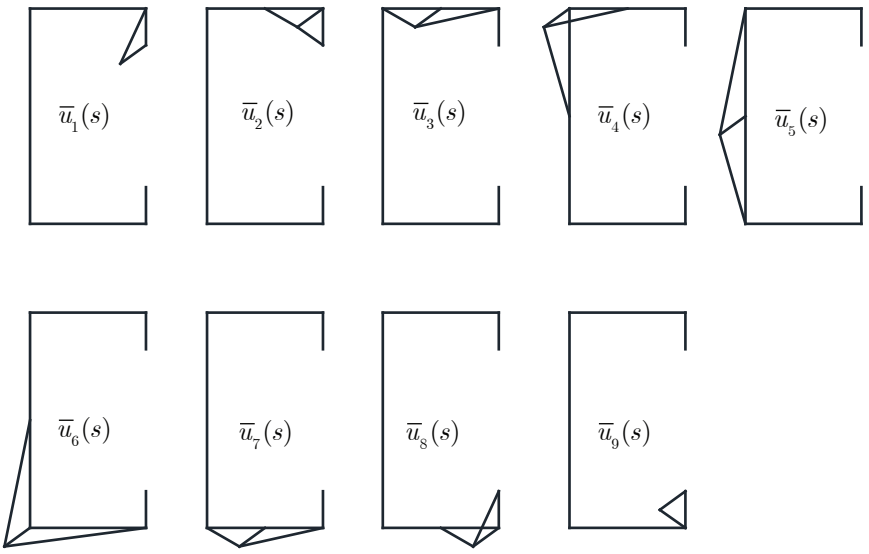

Figure 3.9: Preliminary shear-warping modes

3.4.2.3 GBT modes normalization

The normalization of the first four modes, axial compression, strong/weak axis bending, torsion are ambiguous, i.e., they should agree with Euler-Bernoulli beam theory, and $C_{(1.1)} = A$, $C_{(2.2)} = I_1$, $C_{(3.3)} = I_2$, $C_{(4.4)} = \Gamma$, where A is the area, I_1/I_2 strong/weak axis moment of inertia and Γ the warping constant. And in the case, the GBT modal amplitude ϕ_1 equals axis displacement, ϕ_2/ϕ_3 strong/weak axis rotation and ϕ_4 and tortional angle.

On the other hand, for distortional and local modes there are two conventions for normalization. In the original formulation, these modes are normalized such that the maximum value in the cross-section degrees of freedom is unity, i.e.,

$$max(\mathbf{y_j}) = 1. \tag{3.4.84}$$

Or, distortional and local modes can be normalized such that the maximum in-plane displacement is unity [21], which complies with the definition of *modal participation factor* in Eq. (3.4.102)

$$max(\sqrt{w_j^2(s) + v_j^2(s)}) = 1. \tag{3.4.85}$$

The normalization of shear-warping modes is straightforward, as making the maximum warping equals to unity

$$max(u_j(s)) = 1. \tag{3.4.86}$$

3.4.3 Solving Generalized Beam Theory Governing Equations

3.4.3.1 Finite element approximation of GBT governing equations

To obtain a finite element formulation, Eq. (3.4.35) is rewritten in the variational form

$$\begin{aligned}
&\int_{Le} C_{ik}\phi_{k,xx}\delta\phi_{i,xx} + C_{hk}\phi_{k,xx}\delta\varphi_{h,x} + C_{ij}\varphi_{j,x}\delta\phi_{i,xx} + C_{hj}\varphi_{j,x}\delta\varphi_{h,x} \\
&+ D^I_{ik}\phi_{k,x}\phi_{i,x} + D^I_{hj}\varphi_j\delta\varphi_h + D^{II}_{ik}\phi_k\delta\phi_{i,xx} + D^{II}_{ki}\phi_{k,xx}\delta\phi_i + B_{ik}\phi_k\delta\phi_i \\
&- q_h\delta\varphi_h - q_i\delta\varphi_i + \lambda W^0_m(X_{mik}\phi_{k,x}\phi_{i,x} + X_{mjh}\varphi_{j,x}\delta\varphi_{h,x} + X_{mij}\varphi_{j,x}\delta\phi_{i,xx} + X_{mkh}\phi_{i,xx}\delta\varphi_{h,x}) \\
&= 0
\end{aligned} \tag{3.4.87}$$

where Le stands for the length of the finite element, and λ stands for the parameter of pre-applied reference stress. Likewise in the previous section, i, k correspond to conventional modes and h, j to shear-warping modes. The functions $\phi_k(x)$ (conventional modes except axial extension) are approximated by Hermite polynomials and the function $\phi_{1,x}(x)$ (axial extension mode) and $\varphi_{h,x}$ (shear modes) are approximated by Lagrange polynomials

$$\phi_{1,x} = \zeta_p d_{1.p} \quad \phi_k = \psi_p d_{k.p} \quad \varphi_j = \zeta_p d_{j.p} \quad , \tag{3.4.88}$$

where ψ_p and ζ_p are shape functions of Hermite and Lagrange polynomials in Eq. (3.4.89) and shown in Figure 3.6; and $d_{(\cdot).p}$ stands for the p^{th} FE degree of freedom in Eq. (3.4.90) also shown in Figure 3.10.

$$\begin{aligned}
&\mathbf{\Psi} = \left\{\tfrac{1}{2}(1-\xi)(3\xi-1)(3\xi-2) \quad \tfrac{9}{2}\xi(\xi-1)(3\xi-1) \quad \tfrac{9}{2}\xi(1-\xi)(3\xi-2) \quad \tfrac{1}{2}\xi(3\xi-1)(3\xi-2)\right\}, \\
&\mathbf{Z} = \left\{L_e(\xi^3 - 2\xi^2 + \xi) \quad 2\xi^3 - 3\xi^2 + 1 \quad L_e(\xi^3 - \xi^2) \quad -2\xi^3 + 3\xi^2\right\},
\end{aligned} \tag{3.4.89}$$

$$\begin{array}{llll}
d_{1.1} = \phi_{1.x}(0) & d_{1.2} = \phi_{1.x}(1/3L_e) & d_{1.3} = \phi_{1.x}(2/3L_e) & d_{1.4} = \phi_{1.x}(L_e) \\
d_{k.1} = \phi_{k,x}(0) & d_{k.2} = \phi_k(0) & d_{k.3} = \phi_{k,x}(L_e) & d_{k.4} = \phi_k(L_e) \\
d_{j.1} = \varphi_j(0) & d_{j.2} = \varphi_j(1/3L_e) & d_{j.3} = \varphi_j(2/3L_e) & d_{j.4} = \varphi_j(L_e)
\end{array} \quad . \tag{3.4.90}$$

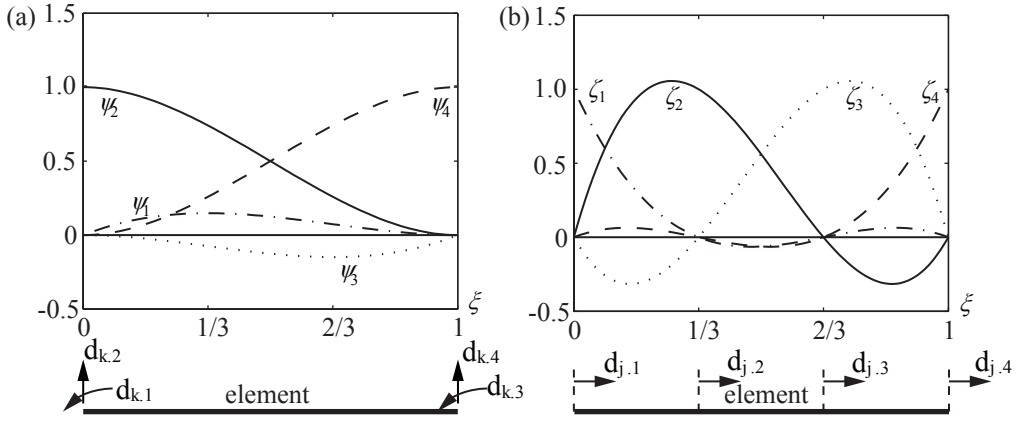

Figure 3.10: Shape functions and FE degrees of freedom of (a) Hermite polynomials, (b) Lagrange polynomials

Perform the integration of Eq. (3.4.87), and the matrix form of finite element approximation can be obtained

$$(\mathbf{k} + \lambda \mathbf{g})\mathbf{d} = \mathbf{f}, \tag{3.4.91}$$

or in the expended form

$$\left(\begin{bmatrix} \mathbf{k}_{11} & \mathbf{0} & \mathbf{k}_{1j} \\ \mathbf{0} & \mathbf{k}_{ik} & \mathbf{k}_{ij} \\ \mathbf{k}_{h1} & \mathbf{k}_{hk} & \mathbf{k}_{hj} \end{bmatrix} + \lambda \begin{bmatrix} \mathbf{0} & \mathbf{0} & \mathbf{g}_{1j} \\ \mathbf{0} & \mathbf{g}_{ik} & \mathbf{g}_{ij} \\ \mathbf{g}_{h1} & \mathbf{g}_{hk} & \mathbf{g}_{hj} \end{bmatrix} \right) \begin{Bmatrix} \mathbf{d}_1 \\ \mathbf{d}_k \\ \mathbf{d}_j \end{Bmatrix} = \begin{Bmatrix} \mathbf{f}_1 \\ \mathbf{f}_k \\ \mathbf{f}_j \end{Bmatrix}, \tag{3.4.92}$$

where $\mathbf{k}$ is the symmetric linear stiffness matrix contains five sub-matrices $\mathbf{k}_{11}$, $\mathbf{k}_{ik}$, $\mathbf{k}_{hj}$, $\mathbf{k}_{1j}$, $\mathbf{k}_{ij}$ reading

$$
\begin{aligned}
\mathbf{k}_{11} &= C_{11}\int_{Le}\mathbf{Z}'^{T}\mathbf{Z}'dx = \frac{C_{11}}{40L_e}\begin{bmatrix} 148 & -189 & 54 & -13 \\ -189 & 432 & -297 & 54 \\ 54 & -297 & 432 & -189 \\ -13 & 54 & -189 & 148 \end{bmatrix}, \\
\mathbf{k}_{ik} &= C_{ik}\int_{Le}\mathbf{\Psi}''^{T}\mathbf{\Psi}''dx + D^{I}_{ik}\int_{Le}\mathbf{\Psi}'^{T}\mathbf{\Psi}'dx + D^{II}_{ik}\int_{Le}\mathbf{\Psi}''^{T}\mathbf{\Psi}dx + D^{II}_{ki}\int_{Le}\mathbf{\Psi}^{T}\mathbf{\Psi}''dx + B_{ik}\int_{Le}\mathbf{\Psi}^{T}\mathbf{\Psi}dx \\
&= C_{ik}\frac{2}{L_e^3}\begin{bmatrix} 2L_e^2 & 3L_e & L_e^2 & -3L_e \\ & 6 & 3L_e & -6 \\ & & 2L_e^2 & -3L_e \\ sim. & & & 6 \end{bmatrix} + D_{ik}\frac{1}{30L_e}\begin{bmatrix} 4L_e^2 & 3L_e & -L_e^2 & -3L_e \\ & 36 & 3L_e & -36 \\ & & 4L_e^2 & -3L_e \\ sim. & & & 36 \end{bmatrix} \\
&+ D^{II}_{ik}\frac{1}{30L_e}\begin{bmatrix} -4L_e^2 & -33L_e & L_e^2 & 3L_e \\ -3L_e & -36 & -3L_e & 36 \\ L_e^2 & -3L_e & -4L_e^2 & 33L_e \\ 3L_e & 36 & 3L_e & -36 \end{bmatrix} + D^{II}_{ik}\frac{1}{30L_e}\begin{bmatrix} -4L_e^2 & -33L_e & L_e^2 & 3L_e \\ -3L_e & -36 & -3L_e & 36 \\ L_e^2 & -3L_e & -4L_e^2 & 33L_e \\ 3L_e & 36 & 3L_e & -36 \end{bmatrix}^{T} \\
&+ B_{ik}\frac{L_e}{420}\begin{bmatrix} 4L_e^2 & 22L_e & -3L_e^2 & 13L_e \\ & 156 & -13L_e & 54 \\ & & 4L_e^2 & -22L_e \\ sim. & & & 156 \end{bmatrix}, \\
\mathbf{k}_{hj} &= C_{hj}\int_{Le}\mathbf{Z}'^{T}\mathbf{Z}'dx + D^{I}_{hj}\int_{Le}\mathbf{Z}^{T}\mathbf{Z}dx \\
&= \frac{C_{hj}}{40L_e}\begin{bmatrix} 148 & -189 & 54 & -13 \\ -189 & 432 & -297 & 54 \\ 54 & -297 & 432 & -189 \\ -13 & 54 & -189 & 148 \end{bmatrix} + \frac{D^{I}_{hj}L_e}{1680}\begin{bmatrix} 128 & 99 & -36 & 19 \\ 99 & 648 & -81 & -36 \\ -36 & -81 & 648 & 99 \\ 19 & -36 & 99 & 128 \end{bmatrix}, \\
\mathbf{k}_{1j} &= C_{1j}\int_{Le}\mathbf{Z}'^{T}\mathbf{Z}'dx + D^{I}_{1j}\int_{Le}\mathbf{Z}^{T}\mathbf{Z}dx \\
&= \frac{C_{hj}}{40L_e}\begin{bmatrix} 148 & -189 & 54 & -13 \\ -189 & 432 & -297 & 54 \\ 54 & -297 & 432 & -189 \\ -13 & 54 & -189 & 148 \end{bmatrix} + \frac{D_{hj}L_e}{1680}\begin{bmatrix} 128 & 99 & -36 & 19 \\ 99 & 648 & -81 & -36 \\ -36 & -81 & 648 & 99 \\ 19 & -36 & 99 & 128 \end{bmatrix}, \\
\mathbf{k}_{ij} &= C_{ij}\int_{Le}\mathbf{\Psi}''^{T}\mathbf{Z}'dx + D^{I}_{ij}\int_{Le}\mathbf{\Psi}'^{T}\mathbf{Z}dx + D^{II}_{ij}\int_{Le}\mathbf{\Psi}^{T}\mathbf{Z}'dx \\
&= C_{ij}\frac{1}{4L_e^2}\begin{bmatrix} 13L_e & -9L_e & -9L_e & 5L_e \\ 18 & -18 & -18 & 18 \\ 5L_e & -9L_e & -9L_e & 13L_e \\ -18 & 18 & 18 & -18 \end{bmatrix} + D^{I}_{ij}\frac{1}{120}\begin{bmatrix} 10L_e & 9L_e & -18L_e & -L_e \\ -6 & -54 & -54 & -6 \\ -L_e & -18L_e & -9L_e & 10L_e \\ 6 & 54 & 54 & 6 \end{bmatrix} \\
&+ D^{II}_{ji}\frac{1}{120}\begin{bmatrix} -10L_e & -9L_e & 8L_e & L_e \\ -114 & 54 & 54 & 6 \\ L_e & 18L_e & -9L_e & -10L_e \\ -6 & -54 & -54 & 114 \end{bmatrix}.
\end{aligned}
\tag{3.4.93}
$$

In Eq. (3.4.93), 1 stands for the uniform compression mode, i, k for the other conventional modes and h, j for shear-warping modes. Such that, $\mathbf{k}_{(\diamond)(\triangle)}$ has the physical meaning correspondingly, for example, $\mathbf{k}_{ij}$ is associated with the coupling stiffness between conventional and shear-warping modes. The sub-matrices in geometric stiffness $\mathbf{g}$ have values

$$\mathbf{g}_{ik} = W_p X_{pik} \int_{Le} \mathbf{\Psi}'^T \mathbf{\Psi}' dx = W_p X_{pik} \frac{1}{30L_e} \begin{bmatrix} 4L_e^2 & 3L_e & -L_e^2 & -3L_e \\ & 36 & 3L_e & -36 \\ & & 4L_e^2 & -3L_e \\ sim. & & & 36 \end{bmatrix}, \tag{3.4.94}$$

$$\mathbf{g}_{hj} = W_m X_{mhj} \int_{Le} \mathbf{Z}'^T \mathbf{Z}' dx = W_m X_{mhj} \frac{1}{40L} \begin{bmatrix} 148 & -189 & 54 & -13 \\ -189 & 432 & -297 & 54 \\ 54 & -297 & 432 & -189 \\ -13 & 54 & -189 & 148 \end{bmatrix}, \tag{3.4.95}$$

$$\mathbf{g}_{1j} = W_m X_{m1j} \int_{Le} \mathbf{Z}'^T \mathbf{Z}' dx = W_m X_{m1j} \frac{1}{40L} \begin{bmatrix} 148 & -189 & 54 & -13 \\ -189 & 432 & -297 & 54 \\ 54 & -297 & 432 & -189 \\ -13 & 54 & -189 & 148 \end{bmatrix}, \tag{3.4.96}$$

$$\mathbf{g}_{ij} = W_m X_{mij} \int_{Le} \mathbf{\Psi}''^T \mathbf{Z}' dx = W_m X_{mij} \frac{1}{4L_e^2} \begin{bmatrix} 13L_e & -9L_e & -9L_e & 5L_e \\ 18 & -18 & -18 & 18 \\ 5L_e & -9L_e & -9L_e & 13L_e \\ -18 & 18 & 18 & -18 \end{bmatrix}, \tag{3.4.97}$$

where $\mathbf{g}_{hj}, \mathbf{g}_{1j}, \mathbf{g}_{ij}$ have negligible effect on the result of a stability problem compared to $\mathbf{g}_{ik}$. Thus a stability problem can be written as

$$\left(\begin{bmatrix} \mathbf{k}_{11} & \mathbf{0} & \mathbf{k}_{1j} \\ \mathbf{0} & \mathbf{k}_{ik} & \mathbf{k}_{ij} \\ \mathbf{k}_{h1} & \mathbf{k}_{hk} & \mathbf{k}_{hj} \end{bmatrix} + \lambda \begin{bmatrix} \mathbf{0} & \mathbf{0} & \mathbf{0} \\ \mathbf{0} & \mathbf{g}_{ik} & \mathbf{0} \\ \mathbf{0} & \mathbf{0} & \mathbf{0} \end{bmatrix} \right) \begin{Bmatrix} \mathbf{d}_1 \\ \mathbf{d}_k \\ \mathbf{d}_j \end{Bmatrix} = \begin{Bmatrix} \mathbf{0} \\ \mathbf{0} \\ \mathbf{0} \end{Bmatrix}. \tag{3.4.98}$$

The right hand side of Eq. (3.4.92) is the generalized force vector with sub-vectors

$$\mathbf{f}_1 = q_1 \int_{Le} \mathbf{Z}^T dx = q_1 \frac{L_e}{8} \begin{bmatrix} 1 & 3 & 3 & 1 \end{bmatrix}^T, \tag{3.4.99}$$

$$\mathbf{f}_i = q_i \int_{Le} \Psi^T dx = q_i \frac{L_e}{12} \begin{bmatrix} L_e & 6 & -L_e & 6 \end{bmatrix}^T, \tag{3.4.100}$$

$$\mathbf{f}_h = q_h \int_{Le} \mathbf{Z}^T dx = q_h \frac{L_e}{8} \begin{bmatrix} 1 & 3 & 3 & 1 \end{bmatrix}^T. \tag{3.4.101}$$

3.4.3.2 Modal participation of GBT solutions

Obviously for different quantities the modal participation factors are different. A modal participation factor that measures the overall participation of in-plane displacement through the member is proposed [21]

$$P_i = \frac{\int_L |\phi_k(x)|dx}{\sum_{k=1}^{n} \int_L |\phi_k(x)|dx}. \tag{3.4.102}$$

This quantity identifies the overall participation of in-plane displacement through the member because by recalling Eq. (3.4.13) and Eq. (3.4.85)

$$v(s,x) = v_k(s)\phi_k(x) \qquad w(s,x) = w_k(s)\phi_k(x), \tag{3.4.103}$$

$$max(\sqrt{u_k^2(s) + v_k^2(s)}) = 1 \quad k \neq 4 \quad , \tag{3.4.104}$$

$|\phi_k(x)|$ equals the maximum in-plane displacement by contribution of mode k. However, mode 4 the torsion of the cross-section is an exception: to keep consistent with the conventional beam theory, $\phi_4(x)$ equals the torsional angle of the cross-section. Hence, in this dissertation, the member-wise modal participation factor is defined as

$$P_k = \frac{\int_L |g_k\phi_k(x)|dx}{\sum_{k=1}^{n} \int_L |g_k\phi_k(x)|dx}, \tag{3.4.105}$$

and corresponding cross-sectional modal participation factor

$$p_k(x) = \frac{|g_k\phi_k(x)|}{\sum_{k=1}^{n} |g_k\phi_k(x)|}, \tag{3.4.106}$$

where g_4 is the largest distance from shear-center to any cross-sectional point for torsional mode, e.g., mode 4 in Figure 4.3, and $g_k = 1$ for all other modes (see Figure 3.11). This conversion from twist to displacement produces modal participation factors that are consistent for all modes, including torsion.

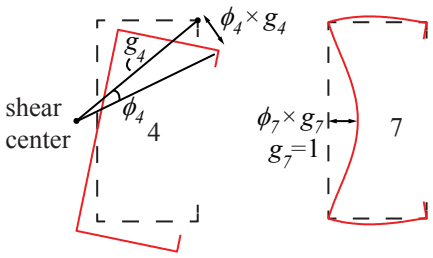

Figure 3.11: For torsional mode the mode amplitude $\phi_4(x)$ equals the torsional angle, while for other GBT modes $\phi_k(x)$ equals maximum in-plane displacement.

Chapter 4

Generalized Beam Theory Elastic Buckling Analysis For Members With Holes

Most thin-walled metallic structural members contain holes that influence buckling load-deformation response. In cold-formed steel framed buildings, studs and joists have pre-punched holes to accommodate utilities (Fig. 1a). Metal storage racks have perforation patterns for adjusting shelf height (Fig. 1b). Holes are placed in aircraft fuselage and ships to reduce weight and to provide maintenance access (Fig. 1c). The goal of this paper is to introduce and demonstrate a theoretical means for characterizing how these holes influence buckling mode participation, which can then inform future design codes and standards.

(a)

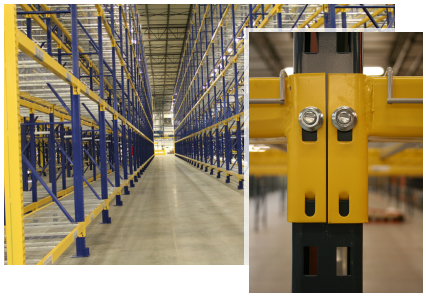

(b)

(c)

Figure 4.1: Examples of cold-formed steel members with holes: (a) studs with pre-punched holes to accommodate utilities; (b) cold-formed steel storage racks; (c) rib with holes spanning between airplane wing spars

It is well known that the presence of holes almost always decreases thin-walled structural capacity [73, 72]. Local buckling can occur in a member at a hole or between holes in

the gross cross-section depending upon the member and hole geometries. New buckling modes, not seen in members without holes, are also created, and these modes can mix with longer wave modes like distortional and global buckling [75, 121]. Holes in a column or beam also decrease the global buckling load or moment [73, 74]. Cold-formed steel framing design treats holes by calculating the critical elastic buckling loads for local, distortional, and global buckling for a member including the influence of holes, which is then reflected in the slenderness and strength equations [72]. The challenge is to identify what buckling modes dominate the load-deformation response for a member with holes, and this is the underlying motivation for the GBT development work presented herein.

Generalized beam theory (GBT) has the ability to calculate pure local, distortional and global buckling loads for a general geometry [28]. In a buckling problem, GBT computes modal amplitudes automatically and each modal contribution to key quantities (e.g., stress, displacement) can be quantified [36]. The GBT's ability to decouple contributions can be employed to identify modes that drive failure [85] which have typically in the past been qualitatively identified with experiments, e.g., [123].

GBT buckling analysis on thin-walled steel frames is presented and validated by Basaglia and Camotim [13, 14, 26]. Thin-walled frames are analyzed in a GBT context by imposing two sets of compatibility conditions to connect structural members: one is for beam generalized displacements and the other is for element (flange, web, etc.) local warping and flexural displacements. The idea of using GBT with compatibility conditions is adopted for members with holes in this paper.

Research concerning GBT analysis for members with holes is limited. Davies [71] used an 'effective thickness/width' method to represent the influence of holes on local and distortional buckling loads, and the gross section properties are used for global buckling, where the thickness and width reductions are based on test data and related empirical equations. Nedelcu [79] employed GBT to perform modal identification of thin shell eigen-buckling analyses assuming the GBT modes for the gross cross-section can be used for the net cross-section with success.

This dissertation builds on previous research to introduce a generally applicable methodology for GBT analysis on members with holes. The approach treats a member with holes as a structural system consisting of prismatic sub-members. These sub-members are connected by enforcing nodal compatibility conditions for the GBT discretization points at the interfaces. To represent the shear lag effect and nonlinear normal stress distribution in the vicinity of a hole, GBT shear modes with nonlinear warping are included. Modifications are made to the GBT geometric stiffness because of the influence from shear lag effect caused by holes. In the following sections, the GBT formulation for a prismatic bar is reviewed and the GBT formulation for members with holes is introduced. Special aspects of analyzing members with holes are defined, namely the compatibility conditions to connect sub-members and the geometric stiffness for members with holes. Validation and three examples are provided.

To analyze members with holes as a structural system, several obstacles need to be overcome.

First, general applicable compatibility conditions are needed for members with holes. Second, because the longitudinal normal stress distribution is nonlinear in the vicinity of a hole, GBT shear modes must be included, and the compatibility conditions have to incorporate shear modes. Third, in a typical GBT analysis, the member-wise geometric stiffness is derived where the reference stress stems from axial load, major axis bending moment, minor axis bending moment, and torsional warping bimoment, as implied by Eq. (3.4.35). The reference stress is nonlinear in the vicinity of a hole and the geometric stiffness is modified to represent this effect. The following sections will focus illustrate the methodology of analyzing members with holes with GBT.

4.1 Compatibility conditions for members with holes

Consider the member with a hole in Figure 4.2. The member with a hole is dissembled into four prismatic sub-members. The cross-section discretization and GBT modes are shown in Fig. 3. In this paper, the discretization nodes of the sub-members are aligned longitudinally as shown in Figure 4.2, e.g., node P_A, P_B. To apply the FE approximation for solving GBT system, each sub-member is further discretized into several finite elements.

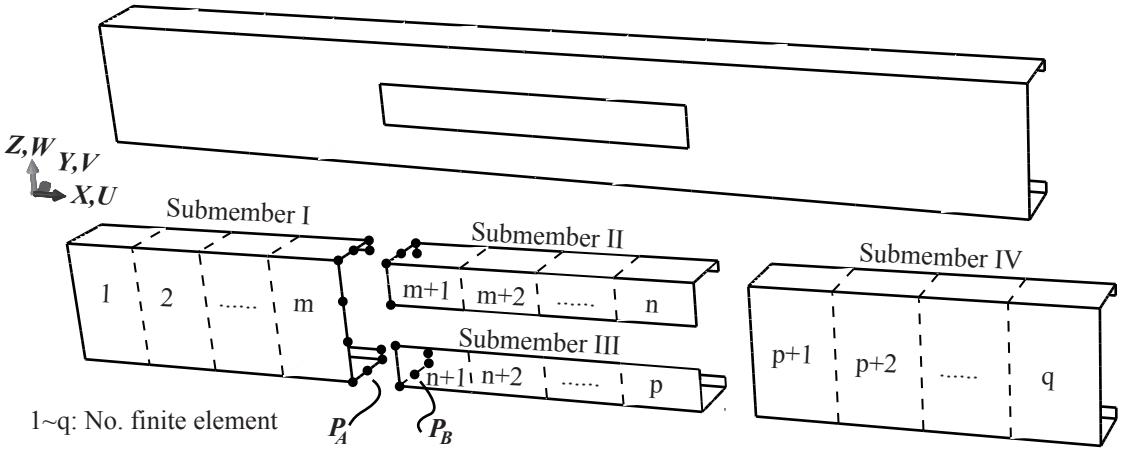

Figure 4.2: Thin-walled member with a hole and decomposed into sub-members

The mechanical compatibility conditions include displacements (U, V, W) continuity and displacement derivatives (U', V', W') continuity of all discretization nodes at the interfaces of sub-members. Taking node P in Figure 4.2 for example, the compatibility conditions associated with this node is

$$
\begin{aligned}
\Pi_P^U &= [U_i(P_A)\phi_{i,x}(x_{P_A}) + U_j(P_A)\varphi_j(x_{P_A})] - [U_i(P_B)\phi_{i,x}(x_{P_B}) + U_j(P_B)\varphi_j(x_{P_B})] = 0,\\
\Pi_P^{U'} &= [U_i(P_A)\phi_{i,xx}(x_{P_A}) + U_j(P_A)\varphi_{j,x}(x_{P_A})] - [U_i(P_B)\phi_{i,x}(x_{P_B}) + U_j(P_B)\varphi_{j,x}(x_{P_B})] = 0,\\
\\
\Pi_P^V &= V_i(P_A)\phi_i(x_{P_A}) - V_i(P_B)\phi_i(x_{P_B}) = 0,\\
\Pi_P^{V'} &= V_i(P_A)\phi_{i,x}(x_{P_A}) - V_i(P_B)\phi_{i,x}(x_{P_B}) = 0,\\
\\
\Pi_P^W &= W_i(P_A)\phi_i(x_{P_A}) - W_i(P_B)\phi_i(x_{P_B}) = 0,\\
\Pi_P^{W'} &= W_i(P_A)\phi_{i,x}(x_{P_A}) - W_i(P_B)\phi_{i,x}(x_{P_B}) = 0,
\end{aligned}
\tag{4.1.1}
$$

where V_i, U_i,W_i and U_j are GBT conventional and shear mode shapes respectively; $\phi_i(x_P)$, $\varphi_i(x_P)$ are the modal amplitudes at the cross-section point P belongs to; and Π stands for the compatibility condition. Applying the same constraints to all discretization nodes at the interface, the two sub-members are connected. In this set of compatibility conditions, the coupling between global modes and local/distortional modes are automatically counted. To implement these constraints when solving the system by finite element method, they are expressed by the FE degrees of freedom.

sub-member I, element n

$$
\begin{aligned}
&\phi_i(x_{P_A}) = d_{i.4} && \varphi_j(x_{P_A}) = d_{j.4} && \phi_{1,x}(x_{P_A}) = d_{1.4} && \phi_{i,x}(x_{P_A}) = d_{i.3}\\
&\phi_{1,xx}(x_{P_A}) = d_{1.r}\frac{\partial \zeta_r}{\partial x}(x_{P_A}) && \phi_{i,xx}(x_{P_A}) = d_{i.r}\frac{\partial \psi_r}{\partial x}(x_{P_A}) && \varphi_{j,x}(x_{P_A}) = d_{j.r}\frac{\partial \zeta_r}{\partial x}(x_{P_A}) &&
\end{aligned}
\tag{4.1.2}
$$

sub-member II, element $n+1$

$$
\begin{aligned}
&\phi_i(x_{P_A}) = d_{i.4} && \varphi_j(x_{P_A}) = d_{j.4} && \phi_{1,x}(x_{P_A}) = d_{1.4} && \phi_{i,x}(x_{P_A}) = d_{i.3}\\
&\phi_{1,xx}(x_{P_A}) = d_{1.r}\frac{\partial \zeta_r}{\partial x}(x_{P_A}) && \phi_{i,xx}(x_{P_A}) = d_{i.r}\frac{\partial \psi_r}{\partial x}(x_{P_A}) && \varphi_{j,x}(x_{P_A}) = d_{j.r}\frac{\partial \zeta_r}{\partial x}(x_{P_A}) &&
\end{aligned}
\tag{4.1.3}
$$

where summation convention applies to r; $d_{i.r}$ stands for the r^{th} FE degree of freedom for the i^{th} modal amplitude (refer to Figure 3.10); and ϕ_i and φ_j are shape functions of Hermite and Lagrange polynomials (also refer toFigure 3.10). Substituting Eq. (4.1.2)Eq. (4.1.3) into Eq. (4.1.1), and repeating the procedure for all discretization nodes at the interfaces connecting two sub-members, a set of constraint equations with FE degrees of freedom as variables can be obtained. These equations can be used in the FE solver, written in matrix form:

$$\Omega d = 0, \tag{4.1.4}$$

in which Ω contains the constraints of compatibility conditions expressed by the FE degrees of freedom, and d is the vector of FE degrees of freedom.

To reflect the constraints in the first order and eigen-buckling analysis, one considers solving a linear system and an eigenvalue problem under linear constraints:

$$Kd = F \quad \text{subject to} \Omega d = 0, \tag{4.1.5}$$

$$Kd = \lambda K_G d \quad \text{subject to} \Omega d = 0. \tag{4.1.6}$$

Let Z be a matrix with columns that span the null space of Ω, i.e., $null(\Omega)$, then the equivalent unconstrained formulations are be obtained

$$(Z^T K Z)y = Z^T F d = Z y' \quad , \tag{4.1.7}$$

$$(Z^T K Z)y = \lambda (Z^T K_G Z) d d = Z y' \quad , \tag{4.1.8}$$

and the unknown FE degrees of freedom d can be solved for.

4.2 Geometric stiffness matrix including a nonlinear normal stress distribution

Because the pre-buckling normal stress distribution is nonlinear near a hole (Fig. 7), it is necessary to make modifications to the geometric stiffness term $W_p^0 X_{pik}$ in Eq. (3.4.35), which is derived from Eq. (3.4.29) to Eq. (3.4.33) under the assumption that the normal stress stems from four common force resultants N, $M1$, $M2$ and bi-moment B. Revisiting Eq. (3.4.29), the geometric stiffness arises from pre-buckling normal stress σ_{xx}^0. Using Eq. (3.4.23) to Eq. (3.4.26), the pre-buckling normal stress in a general case is

$$\sigma_{xx}^0(x,s) = E u_{,x}(x,s) = E[u_k(s)\phi_{k,xx}^0(x) + u_j(s)\varphi_{j,x}^0(x)] \tag{4.2.1}$$

where ϕ_k^0 and φ_k^0 are modal amplitudes corresponding to the pre-buckling state obtained from first-order analysis. Substituting Eq. (4.2.1) into Eq. (3.4.29), the geometric stiffness term $W_p^0 X_{pik}$ in the differential equations system Eq. (3.4.35) may be replaced by tensor X_{ik}, where

$$\begin{aligned} X_{ik}(x,s) &= \int_b \sigma^0_{xx}(v_i v_k + w_i w_k)ds \\ &= \int_b E[u_p \phi^0_{p,xx}(x) + u_j \varphi^0_{j,x}(x)](v_i v_k + w_i w_k)ds \\ &= \phi^0_{p,xx}(x)\int_b E u_p(v_i v_k + w_i w_k)ds + \varphi^0_{j,xx}(x)\int_b E u_j(v_i v_k + w_i w_k)ds \\ &= \phi^0_{p,xx}(x)\chi_{pik} + \varphi^0_{j,xx}(x)\chi_{jik} \end{aligned} \tag{4.2.2}$$

in which χ_{pik}, χ_{jik} are defined as

$$\begin{aligned} \chi_{pik} &= \int_b E u_p(v_i v_k + w_i w_k)ds, \\ \chi_{jik} &= \int_b E u_j(v_i v_k + w_i w_k)ds. \end{aligned} \tag{4.2.3}$$

Now that the coefficient X_{ik} in the governing differential equation has been altered, the geometric stiffness g_{ik} Eq. (3.4.94) in the finite element formulation Eq. (3.4.98) is updated accordingly:

$$\begin{aligned} g_{ik} &= \int_{L_e} X_{ik} {\Psi'_1}^T \Psi'_1 dx \\ &= \chi_{pik}\int_{L_e} \phi^0_{p,xx}(x){\Psi'_1}^T\Psi'_1 dx + \chi_{jik}\int_{L_e} \varphi^0_{j,x}(x){\Psi'_1}^T\Psi'_1 dx. \end{aligned} \tag{4.2.4}$$

Once $\phi^0_k(x)$ and $\varphi^0_j(x)$ are obtained from first order analysis, g_{ik} can be readily calculated with the knowledge that $\phi^0_k(x)$ and $\varphi^0_j(x)$ are approximated by Lagrange and Hermite polynomials.

4.3 Verification and illustrative examples

To verify and illustrate GBT analysis for members with holes, three examples with various buckling types, boundary conditions, and hole quantity are shown. The first example is a 900 mm long member with the boundary condition of one end warping-fixed and the other pinned-warping free; the dominant buckling mode is local. The second example is a 1600 mm long member with both ends pinned-warping free, and the dominant buckling mode is global. The third example shown is a 1600 mm long member with one end warping-fixed and the other pinned-warping free. There are two rectangular holes where the spacing and end distances are consistent with typical U.S. industry practice [8], and in this case the

dominant mode is distortional. The results are compared with shell finite element method results given by ABAQUS [120]. For GBT analysis, the cross-section discretization and GBT mode shapes are shown in Figure 4.3. For shell finite element analysis (SFEA) in ABAQUS, S4R elements are used and all elements are rectangular with an aspect ratio between 1:1 and 2:1. In the cross-sectional directions (Y,Z in Fig. 6), the discretization is identical with GBT shown in Figure 4.3, and in the longitudinal direction, the discretization is made every 10 mm.

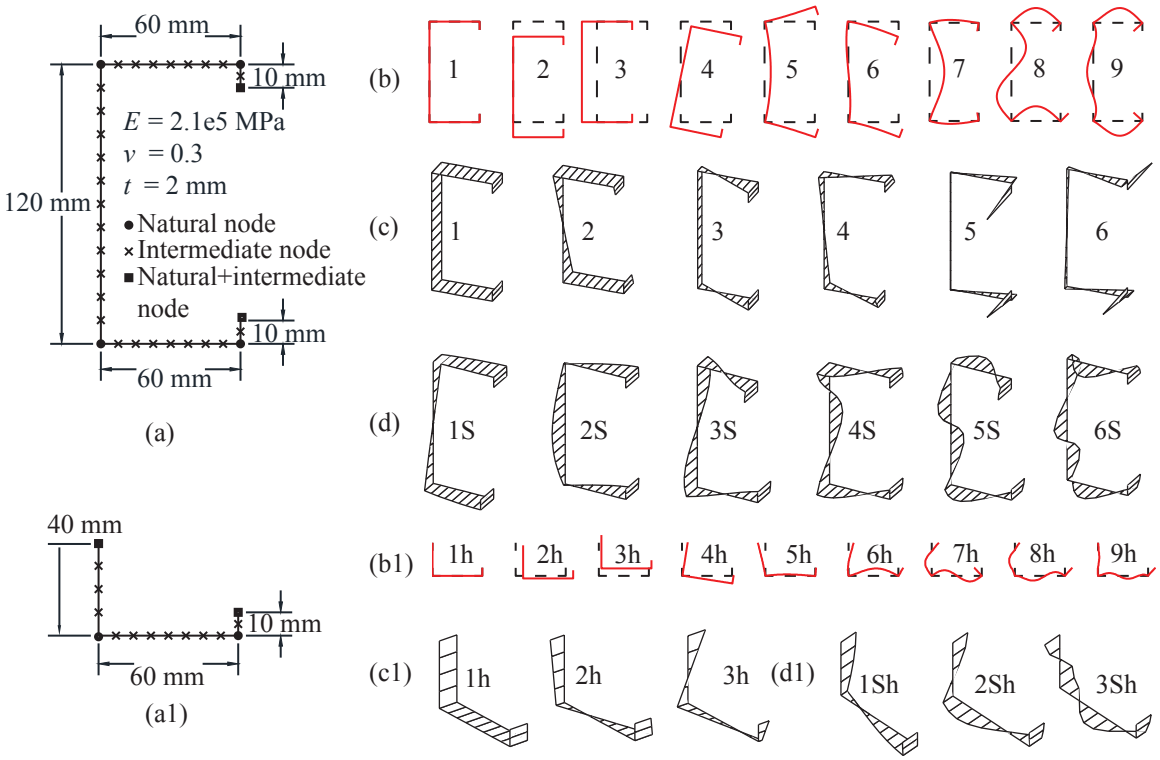

Figure 4.3: GBT mode shapes: (a) cross-section dimensions and discretization; (b, b1) in-plane components of conventional modes; (c, c1) warping components of conventional modes; and (d1, d2) shear modes for gross and net cross-sections respectively

4.3.1 Example 1: local buckling, single hole

A perforated thin-walled structural member with a Cee cross-section is shown in Figure 4.4, with the gross and net cross-sections and GBT modes summarized in Figure 4.3. The member is warping-fixed at one end and pinned-warping free at the other. It is viewed as an assembly of four sub-members for GBT analysis as shown in Figure 4.4, where the sub-member I/II/III/IV is discretized into 8/1/1/8 finite elements respectively. The first order analysis is carried out by both GBT and SFEA under a compression of 1 kN from

the pinned-warping free end. The longitudinal stress distribution in the web is shown in Figure 4.5. It can be seen the distribution and amplitude of normal stresses agree, and the nonlinear stress distribution in the vicinity of the hole is predicted by GBT. The stress is not strictly continuous across the interface of net and gross cross-sections in the GBT analysis because the FE method is an approximation of the differential equations and equilibrium may not be satisfied at the element interfaces.

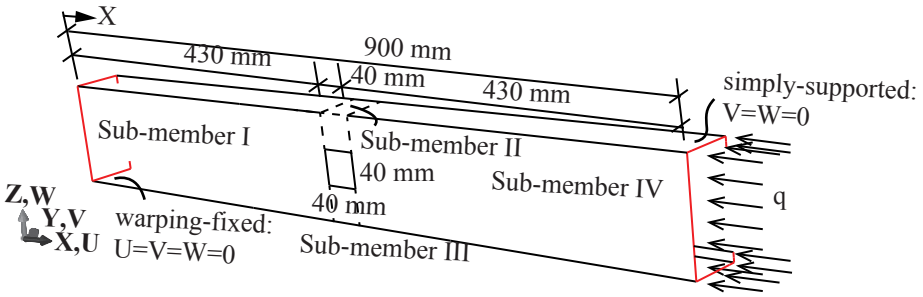

Figure 4.4: Local buckling example: dimensions and loading/boundary conditions.

Figure 4.5: Local buckling example: first order analysis normal stress distributions: (a) GBT, (b) SFEA

The GBT eigen-buckling analysis is conducted by using the geometric stiffness matrix calculated from the first-order analysis result using Eq. (4.2.4). The first critical buckling load calculated by SFEA is 147.0 kN, while GBT yields 150.4 kN (2.3% difference). The buckling modes generated by GBT and SFEA are compared in Figure 4.6. It can be seen that the buckling modes are consistent, as both have four local buckling half-waves near the pinned-warping free end. Dominant modal amplitudes and participation along the member are provided in Figure 4.7 and Figure 4.8. From Figure 4.7, it is confirmed that local buckling dominates at the right half of the member, where four half-waves are present (see ϕ_7, ϕ_9). Local buckling mixes with distortional buckling, see mode 5,6 in Figure 4.7 and Figure 4.8. Unstiffened strip local buckling (mode 5h), flange local buckling (mode 6h), and flexural unstiffened strip buckling (mode 3h) are all observed at the net cross-section as shown in Figure 4.7c and Figure 4.8c.

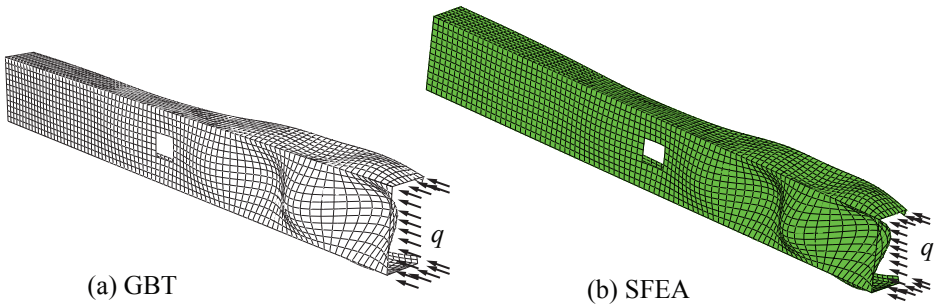

Figure 4.6: Example 1: most relevant modal amplitudes along the member: (a) gross cross-section, (b) net cross-section, sub-member II, (c) net cross-section, sub-member III

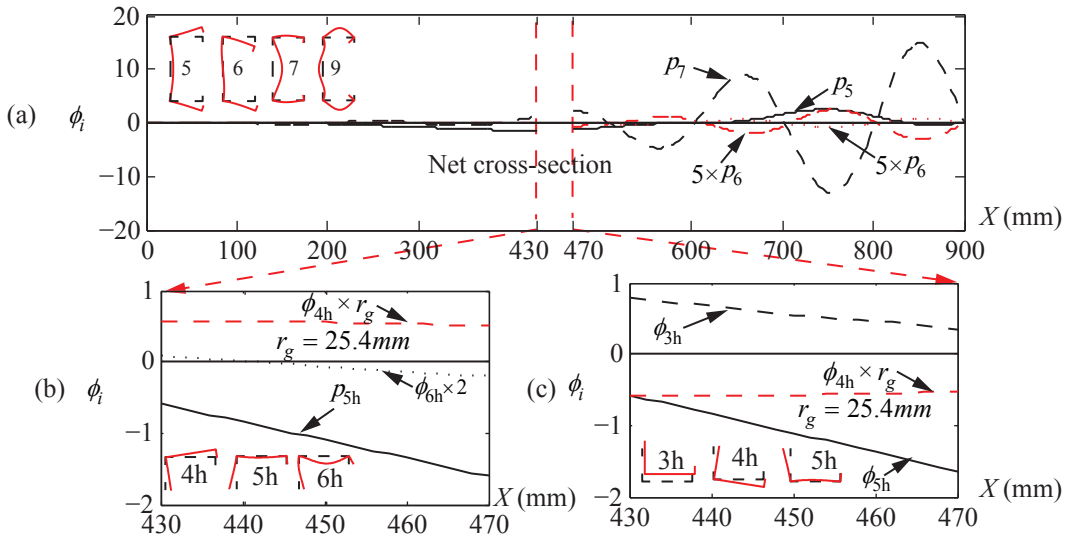

Figure 4.7: Example 1: most relevant modal amplitudes along the member: (a) gross cross-section, (b) net cross-section, sub-member II, (c) net cross-section, sub-member III

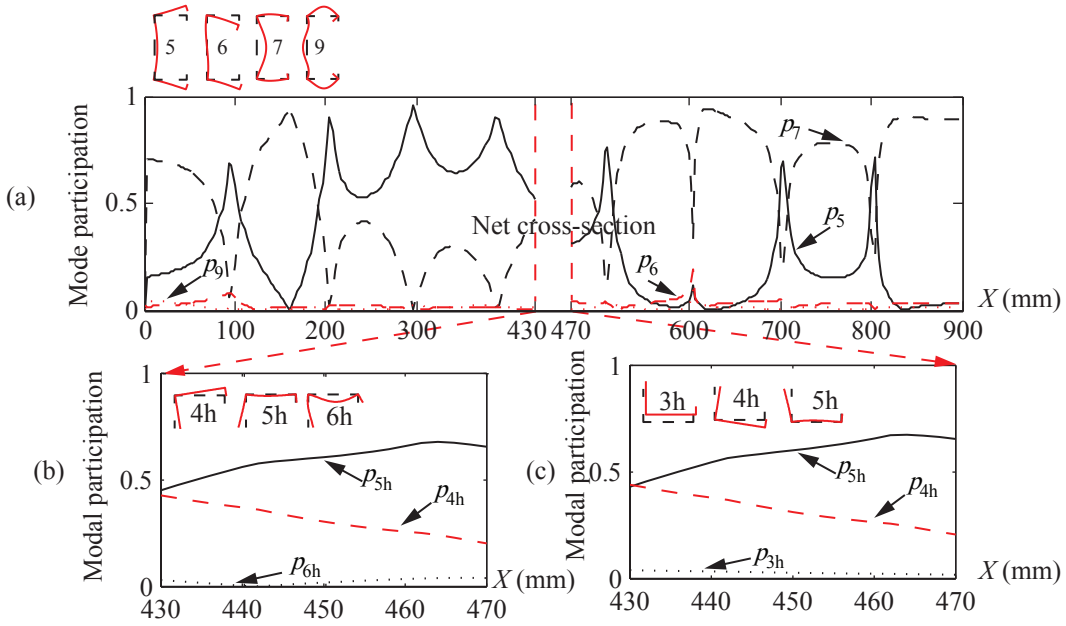

Figure 4.8: Example 1: most relevant displacement modal participations along the member: (a) gross cross-section, (b) net cross-section, sub-member II, (c) net cross-section, sub-member III

4.3.2 Example 2: global buckling, single hole

The second example involves a 1600 mm long member, with a rectangular hole at the middle. The cross-section and material properties are identical to the previous example. The member is pinned-warping free at both ends and loaded at both ends by uniform compression. It has sub-member I/II/III/IV which are further discretized into 6/1/1/6 finite elements for GBT analysis.

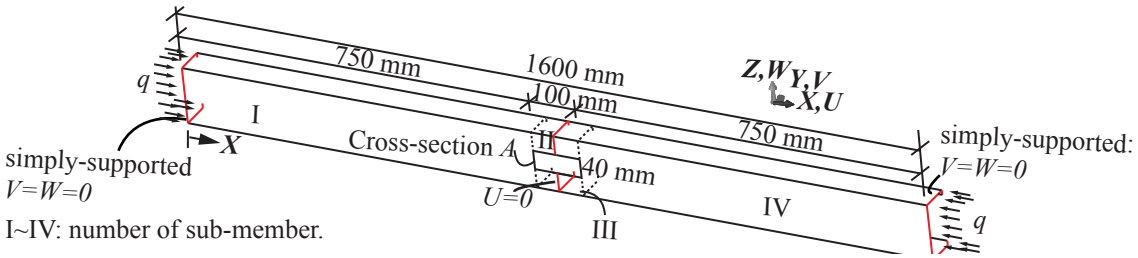

Figure 4.9: Global buckling example: dimensions and loading/boundary conditions.

The first mode buckling load calculated by GBT is 118.3 kN, in comparison with SFEA result of 116.9 kN (1.2% difference). The modes generated by GBT and SFEA are compared

in Fig. 8 with both showing flexural-torsional (global) buckling. The shape generated by GBT agrees with SFEA as shown in Figure 4.10.

Modal amplitudes and participation along the member are presented in Figure 4.11 and Figure 4.12 (only the lower half of the net-cross section are depicted because of symmetry). For the gross cross-section, the dominant GBT mode is flexural-torsional buckling (mode 4, 2) mixing with distortional buckling mode 6 Figure 4.11a, Figure 4.12a), and the variation of ϕ_4, ϕ_2, ϕ_6 agree with the mode shape in Figure 4.10, as the magnitude of twisting grows from the ends to the middle. For the net cross-section, the dominant modes are rigid body modes 2,3, and 4 (Figure 4.11b,c, Figure 4.12b,c).

The contributions of GBT modes is further illustrated in Figure 4.12 by the in-plane deformation of the cross-section A, which is an interface of the net and gross cross-section (see Figure 4.9). The displacements of the gross cross-section coincides with that of net cross-section at A, which verifies the effectiveness of the compatibility conditions enforced. From Fig. Figure 4.12b, it can be concluded that the torsional mode 4 dominates the deformation of the gross cross-section. And from Fig. Figure 4.12c, it can be observed that twisting at the net cross-section consists of the contribution from modes 2h, 3h, and 4h, which are flexural and torsional modes of the upper and lower half of the net cross-section.

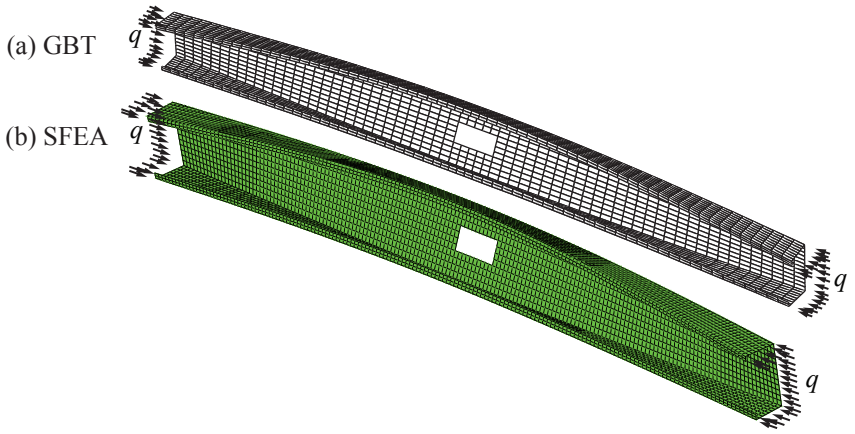

Figure 4.10: Global buckling example: eigen-buckling shapes, (a) GBT, (b) SFEA

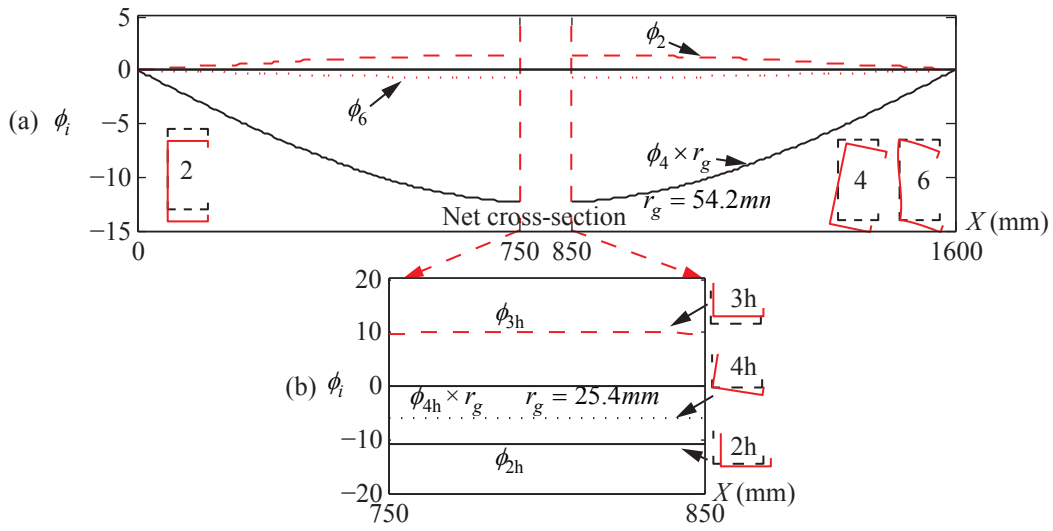

Figure 4.11: Example 2: most relevant modal amplitudes along the member: (a) gross cross-section, (b) net cross-section, sub-member III

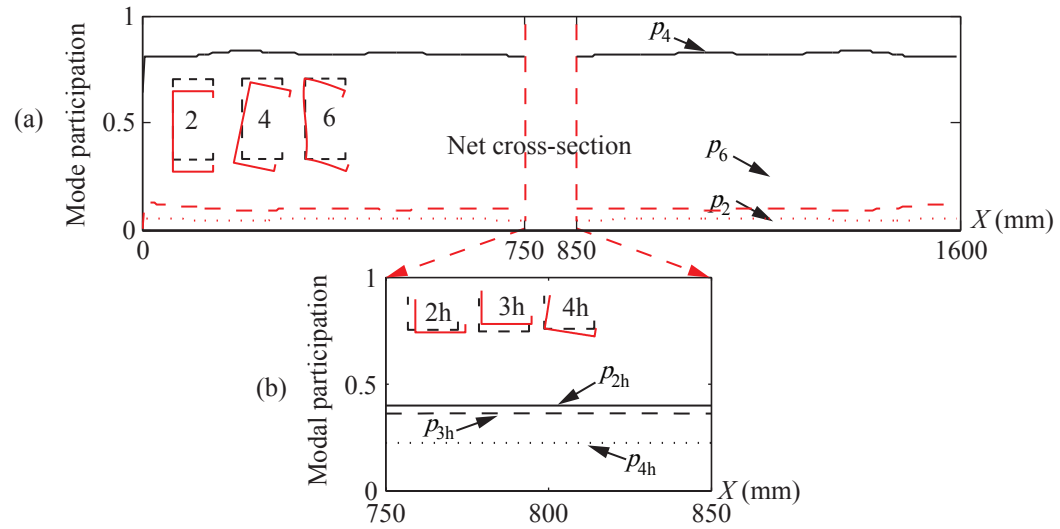

Figure 4.12: Example 2: most relevant modal amplitudes along the member: (a) gross cross-section, (b) net cross-section, sub-member III

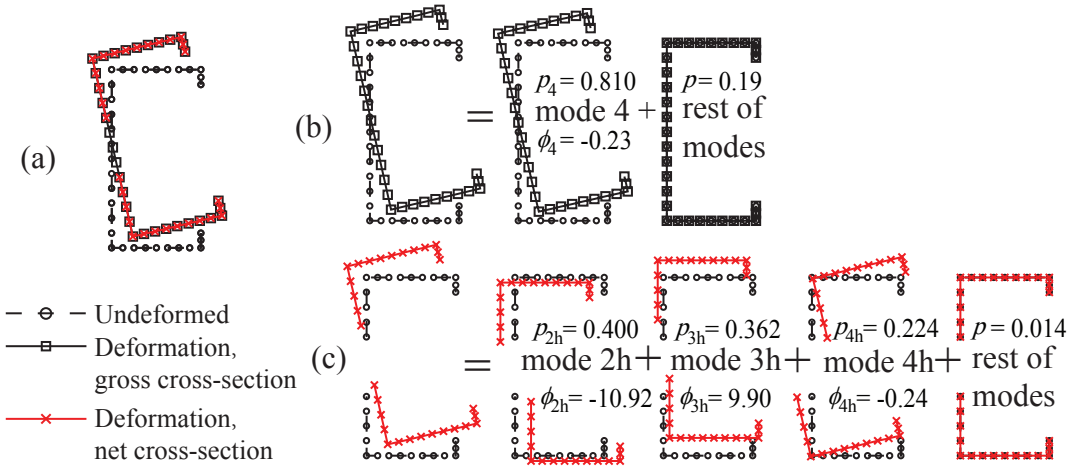

Figure 4.13: Example 2: in-plane deformation at cross-section A: (a) displacement of gross cross-section agreeing with that of net cross-section, (b) displacement decomposition for gross cross-section, (c) displacement decomposition for net cross-section

4.3.3 Example 3: distortional buckling, two holes

The third example is a 1600 mm long member with the same cross-section as in Example 1 and 2 Figure 4.3. There are two holes with the same size of 100 mm by 40 mm. Their locations are shown in Figure 4.14, where the spacing and hole-edge to end distance satisfy standard industry practice [8]. The member is warping-fixed at the left end and pinned-warping fixed at the right, and an axial load is present at the right end. The sub-member I˜VII is discretized into 8/2/2/12/2/2/8 finite elements for GBT analysis.

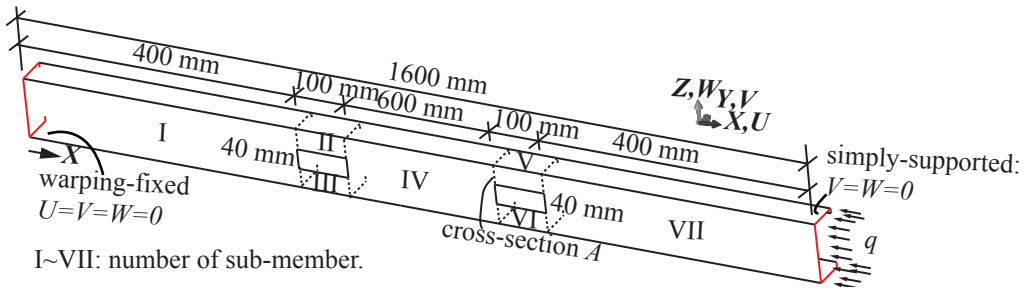

Figure 4.14: Distortional buckling example: dimensions and loading/boundary conditions.

Buckling mode shapes from GBT and SFEA are shown in Figure 4.15. The first mode buckling load is 135.8 kN (GBT) and 132.8 kN (SFEA), corresponding to a difference of 2.2%. The buckling mode shapes are consistent, and the tendency for distortional buckling to initiate at the location of holes [62] is observed in this example. Modal amplitudes and

participation along the member are shown in Figure 4.16 and Figure 4.17. For the gross cross-section, distortional mode 5 is dominant as shown in Figure 4.17a and the variation of its amplitude in Figure 4.16a agrees with visual inspection of the buckling shape inFigure 4.15. For the net cross-section, the main mode is mode 4 (Figure 4.16b,c, Figure 4.17b,c), which is the torsional mode for the sub-member. The contribution of GBT modes is further illustrated in Fig. 20 by the decomposition of in-plane deformation for cross-section A, which is an interface of net and gross cross-section, in Fig. 16. Similar to the previous example, the compatibility condition is satisfied as the displacement of gross cross-section coincides with that of the net cross-section. The in-plane displacement of the gross cross-section is mode-wise decomposed in Figure 4.18b, which confirms that the distortional mode 5 governs the gross cross-section and local mode 7 contributes a minor part of the deformation. For the net cross-section, it can be seen from Figure 4.18c, the twisting (mode 4h) of both the upper and lower half the net cross-section constitute the buckling displacement that 'matches' the distortional mode 5 of the gross cross-section.

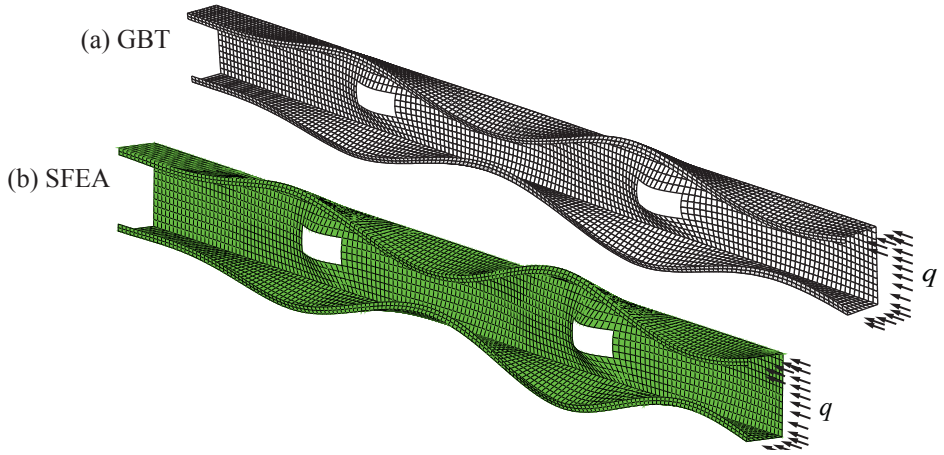

Figure 4.15: Distortional buckling example: eigen buckling shapes, (a) GBT, (b) SFEA

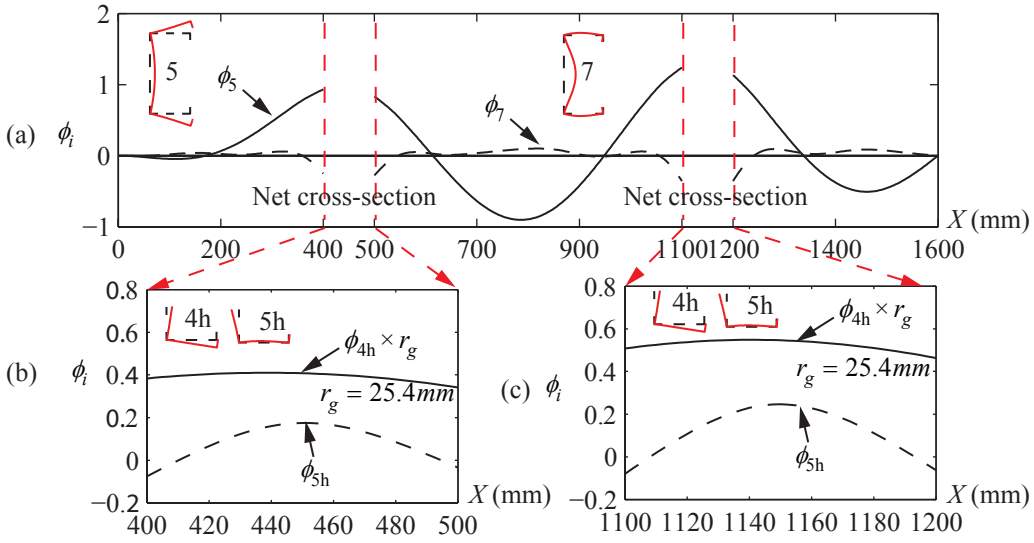

Figure 4.16: Example 3: most relevant modal amplitudes along the member: (a) gross cross-section, (b) net cross-section, sub-member III, (c) net cross-section, sub-member VI

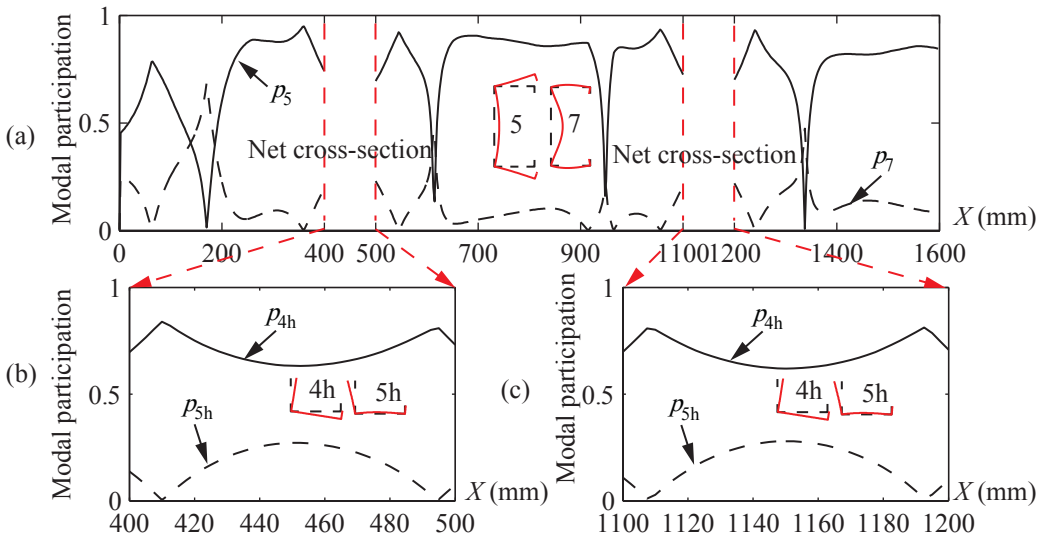

Figure 4.17: Example 3: most relevant modal participations along the member: (a) gross cross-section, (b) net cross-section, sub-member III, (c) net cross-section, sub-member VI

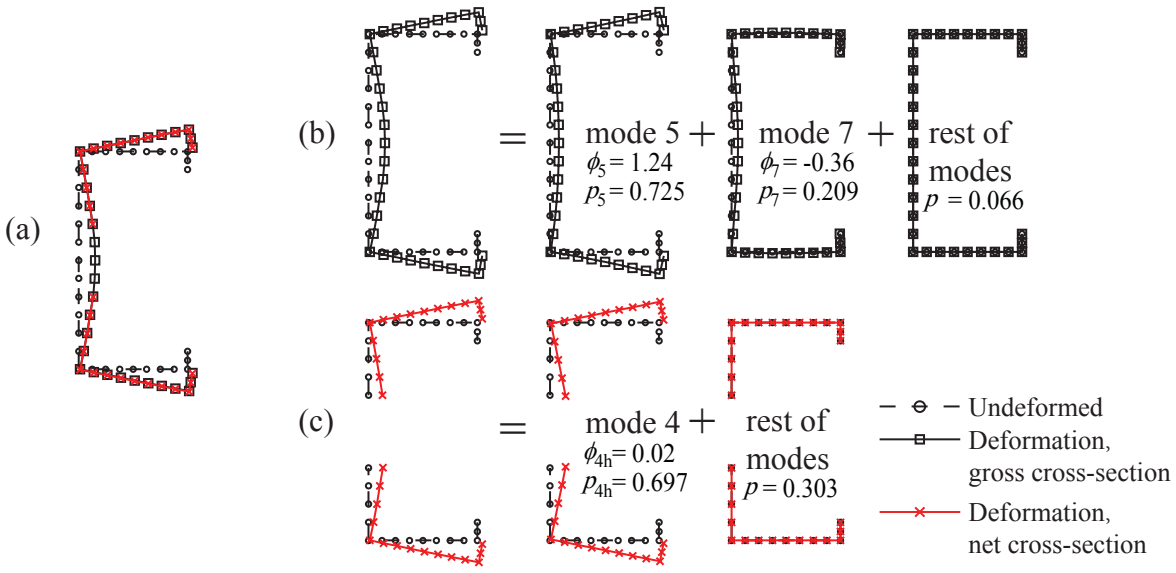

Figure 4.18: Example 3: in-plane deformation at cross-section A: (a) displacement of gross cross-section agreeing with that of net cross-section, (b) displacement decomposition for gross cross-section, (c) displacement decomposition for net cross-section

4.4 Summary

GBT analysis for members with holes is introduced and validated in this paper. Members with holes are viewed as an assembly of multiple prismatic sub-members, and the compatibility conditions to connect them involve displacements and displacement derivative continuities across the interfaces of gross and net cross-sections. The finite element method is utilized as a numerical technique for solving the GBT governing differential equations system, and these compatibility conditions are expressed in terms of FE degrees of freedom for first-order and eigen-buckling analysis. The geometric stiffness term in the GBT governing differential equation is modified to include the nonlinear normal stress distribution in the vicinity of holes caused by the presence of holes, which requires a first-order analysis determining the stress state prior to the eigen-buckling analysis.

Three examples highlighting local, global, distortional buckling are presented. Mode critical buckling loads and shapes are consistent with the shell finite element method. Local buckling at the net cross-section was identified as local buckling of the unstiffened strip on either side of the hole, while distortional and global buckling are represented as rigid body flexural and torsional modes of the unstiffened strip and connected flange. The authors are currently

extending this GBT approach to circular and oval holes and also formalizing ideas for how to include this new quantitative information about buckling mode composition at a net cross-section in codes and standards.

Chapter 5

Elastic Buckling Mode Decomposition for Thin-walled Members Based on Generalized Beam Theory

For thin-walled structural members, elastic buckling modes become mixed and the additional modes can erode the load-carrying capacity. When the walls become sufficiently thin, even relatively pure global buckling modes have a small participation from local buckling. Elastic buckling mode decomposition can be used to identify the global (G), distortional (D) and local (L) dominating modes from Finite Element Analysis or experimental point clouds, and then the elastic buckling mode can be used for strength prediction for the corresponding failure mode using Direct Strength Method. It is worth noting that Direct Strength Method takes the minimum of G,D,L limit state capacity as the nominal strength of the member. However, when the lowest elastic buckling mode is highly mixed, it is very likely the failure mode being interactive buckling as well. The interactive buckling limit state has not been fully formulated in the context of Direct Strength Method. The buckling mode participation information will be used as input for this dissertation's research on interactive buckling strength prediction.

This chapter introduces a method utilizing GBT mode shapes as basis functions, and obtains modal amplitudes by solving a small-scale least squares problem at discrete cross-sections along a thin-walled member. The method utilizes concepts from both existing cFSM and GBT methods and has the following merits: (i) a single set of basis functions that can be used for any boundary conditions or member length; (ii) basis functions are easy to obtain as simply being GBT mode shapes; (iii) once GBT mode shapes and displacement fields are known, modal identification can be carried out without the knowledge of GBT assumptions about the displacement fields and constitutive law for calculating the stiffness terms, and without complex integrals for evaluating stiffness terms. Derivation and validation are provided in the following sections, demonstrating the method's general applicability.

5.1 Buckling mode decomposition for prismatic members using GBT

In a general buckling problem, several buckling modes are mixed and they interact with each other [36]. In the context of GBT, the interaction is taken into account by coupled stiffness terms, e.g., matrix D and X in Eq. (3.4.35) above are coupled as off-diagonal terms are present. However in-plane displacement fields are linear combinations of buckling mode shapes without coupling, where the weighting function is the modal amplitude vector, as shown in Eq. (3.4.13).

Therefore, in this paper, the modal amplitude vector $\phi_k(x)$ in Eq. (3.4.13) is solved by substituting $u_k(s)$, $v_k(s)$, and $w_k(s)$ obtained by 'cross-sectional analysis' and $u(s,x)$, $v(s,x)$, $w(s,x)$ obtained from a general 3d displacement field, for example, a specific mode from a thin shell finite element eigen-buckling analysis or from measured point cloud data during a column or beam test. Once the modal amplitude vector $\phi_k(x)$ is obtained at multiple discrete cross-sections along the member, member-wise modal participation can be evaluated as described in the next section.

5.1.1 Calculation of Modal Amplitudes at Given Cross-Section

If an open cross-section is discretized by n nodes, there are $n+2$ GBT modes. Beyond mode 1 for uniform compression, amplitudes of n+1 modes are to be quantified. These amplitudes, i.e., $\phi_k(x)$, can be found by solving the least squares problem in Eq. (5.1.1):

$$\sum_{k=2}^{n} \begin{bmatrix} V_k \\ W_k \end{bmatrix}_{2n\times(n+1)} \{\phi_k(x)\}_{(n+1)\times 1} \overset{\substack{least\\ square}}{=} \begin{Bmatrix} V \\ W \end{Bmatrix}_{2n\times 1} \tag{5.1.1}$$

in which (i) V_k, W_k are displacement components at discretization nodes of GBT mode k in the global coordinate system; once the GBT mode shapes $u_k(s)$, $v_k(s)$, and $w_k(s)$ as shown in Figure 4.3 are obtained from the GBT cross-section analysis [91, 53] or by free software which conduct cross-sectional analysis [23, 25] , V_k, W_k can be readily obtained by coordinate transformation; (ii) $\phi_k(x)$ is the modal amplitude vector of mode k at location x along the member, (iii) V, W are in-plane displacements in the global coordinate system Figure 3.1 obtained by FEA or by test measurements, (iv) the subscript denotes the dimensions of the matrix with n being the number of discretization nodes. The above equation is a linear optimization problem with $n+1$ input arguments and $2n$ objectives. For a general mathematical problem without physical meaning, the solution is challenging and possibly undefined because there are far more equations to solve than input arguments. However, because of Generalized Beam Theory kinematics, many of these $2n$ equations are 'related', and the least squares problem can be solved with minimal error.

The justification for Eq. (5.1.1) is provided next. It is shown that: (i) only kinematics are used in the method once the mode shapes are known, i.e., no stiffness matrix is involved; (ii) the method is applicable to different loading and boundary conditions; and (iii) the error of the mode identification comes from the incompleteness of the GBT displacement field. Specifically, GBT utilizes Vlasov's null membrane strain assumption, which forces the local displacement v to be a constant in each fold line, and transverse extension is not captured.

The justification of Eq. (5.1.1) is demonstrated through an illustrative example shown in Figure 5.1 by four steps. The cross-section has eight nodes and ten GBT modes with nine modal amplitudes to be identified.

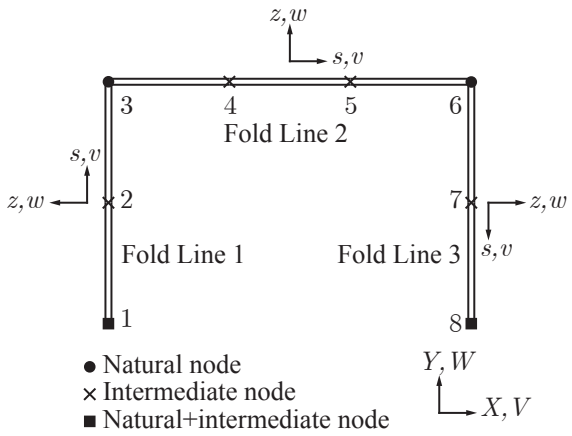

Figure 5.1: Illustrative cross-section

5.1.1.1 Step 1 - Assuming Vlasov's assumption applies for the displacement field, and using v of fold lines and w of intermediate nodes to solve for $\{\phi_k\}$

Since Vlasov's assumption applies at this stage, the displacement v is a constant in each fold line (FL). Once v of all fold lines and w of intermediate nodes are obtained, a linear system to solve for $\{\phi_k\}$ can be written down as:

$$\begin{bmatrix} v_2^{FL.1} & v_3^{FL.1} & \dots & v_{10}^{FL.1} \\ v_2^{FL.2} & v_3^{FL.2} & \dots & v_{10}^{FL.2} \\ v_2^{FL.3} & v_3^{FL.3} & \dots & v_{10}^{FL.3} \end{bmatrix} \begin{Bmatrix} \phi_2 \\ \phi_3 \\ \dots \\ \phi_{10} \end{Bmatrix} = \begin{Bmatrix} v^{FL.1} \\ v^{FL.2} \\ v^{FL.3} \end{Bmatrix}, \tag{5.1.2a}$$

$$\begin{bmatrix} w_2^1 & w_3^1 & ... & w_{10}^1 \\ w_2^2 & w_3^2 & ... & w_{10}^2 \\ w_2^4 & w_3^4 & ... & w_{10}^4 \\ w_2^5 & w_3^5 & ... & w_{10}^5 \\ w_2^7 & w_3^7 & ... & w_{10}^7 \\ w_2^8 & w_3^8 & ... & w_{10}^8 \end{bmatrix} \begin{Bmatrix} \phi_2 \\ \phi_3 \\ ... \\ \phi_{10} \end{Bmatrix} = \begin{Bmatrix} w^1 \\ w^2 \\ w^4 \\ w^5 \\ w^7 \\ w^8 \end{Bmatrix}, \tag{5.1.2b}$$

where: (i) superscript $(\cdot)^{FL.i}$ stands for the i^{th} fold line; (ii) $(\cdot)^j$ stands for the jth node, noting that nodes (1,2,4,5,7,8) are intermediate nodes; and (iii) subscript $(\cdot)_k$ stands for the k^{th} GBT mode. Eq. (5.1.2b), Eq. (5.1.2b) can be written compactly as:

$$\sum_{k=2}^{n} \begin{bmatrix} v_k^{FoldLine} \\ w_k^{Inter.Node} \end{bmatrix} \{\phi_k\} = \begin{Bmatrix} v^{FoldLine} \\ w^{Inter.Node} \end{Bmatrix}. \tag{5.1.3}$$

(Eq. (5.1.3))is a linear system with nine equations to solve for nine unknowns (ϕ_2~ϕ_{10}). Since the mode shapes are linearly independent as displacement-field basis functions, the solution is readily obtained by solving a determined linear system.

5.1.1.2 Step 2 - Still assuming Vlasov's assumption applies, but using v and w of all nodes (intermediate and natural) to solve for $\{\phi_k\}$

(Eq. (5.1.3)) in Step 1 can generate the modal amplitude vector $\{\phi_k\}$ if Vlasov's assumption applies. In Step 2, another linear system is shown to yield $\{\phi_k\}$ as well by illustrating the equivalence between Step 2 and Step 1. The linear system in Step 2 corresponds to displacements v and w of all nodes in local coordinate system (see Figure 3.1 for convention of local coordinate system) as follows: :

$$\cdot \begin{bmatrix} v_2^1 & v_3^1 & ... & v_{10}^1 \\ v_2^2 & v_3^2 & ... & v_{10}^2 \\ \vdots & \vdots & \vdots & \vdots \\ v_2^8 & v_3^8 & ... & v_{10}^8 \end{bmatrix} \begin{Bmatrix} \phi_2 \\ \phi_3 \\ \vdots \\ \phi_{10} \end{Bmatrix} = \begin{Bmatrix} v^1 \\ v^2 \\ \vdots \\ v^8 \end{Bmatrix}, \tag{5.1.4a}$$

$$\begin{bmatrix} w_2^1 & w_3^1 & ... & w_{10}^1 \\ w_2^2 & w_3^2 & ... & w_{10}^2 \\ \vdots & \vdots & \vdots & \vdots \\ w_2^8 & w_3^8 & ... & w_{10}^8 \end{bmatrix} \begin{Bmatrix} \phi_2 \\ \phi_3 \\ \vdots \\ \phi_{10} \end{Bmatrix} = \begin{Bmatrix} w^1 \\ w^2 \\ \vdots \\ w^8 \end{Bmatrix}. \tag{5.1.4b}$$

Compactly:

$$\sum_{k=2}^{n} \begin{bmatrix} v_k \\ w_k \end{bmatrix} \{\phi_k\} = \begin{Bmatrix} v \\ w \end{Bmatrix}. \tag{5.1.5}$$

For interpretation, Eq. (5.1.4a), Eq. (5.1.4b) is annotated in Figure 5.2. In Eq. (5.1.4a), since local displacement v is constant in each fold line, rows 1 to 3 in the red box all correspond to v in the first fold line, because nodes 1 to 3 belong to the first fold line (Natural nodes belong to two fold lines. For the justification, the local coordinate system of the natural node is taken with the fold line before it, e.g., node 3 uses the local coordinate system of fold line 1). The same consideration applies for the second and third fold lines, and thus Eq. (5.1.4a) is equivalent with Eq. (5.1.2a) in Step 1, as both of them involve v of all fold lines.

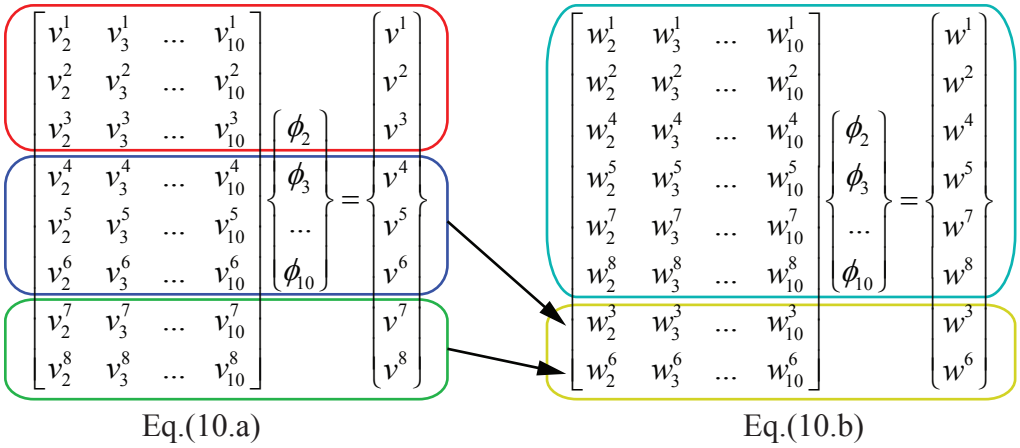

Figure 5.2: Eq. (5.1.3), Eq. (5.1.4b) rewritten with annotations

For Eq. (5.1.4b), the order of nodes 1 to 10 is rearranged in Figure 5.2. The first part with intermediate nodes (1,2,4,5,7,8) in the cyan box is identical to Eq. (5.1.2b) . The second part, in the yellow box, involves w^3 and w^6. Because node 3 and node 6 are at intersections of fold lines, w translations of intersections are equivalent to v displacements of adjacent fold lines.

Taking node 3 for example (see Figure 5.3), $w^{3'}$ is the horizontal displacement at node 3. This translation is related to local shifting in the second fold line as $w^3 = -v^{FL.2}$, in which $v^{FL.2}$ is already taken into account in Eq. (5.1.2a) and Eq. (5.1.4a). The same type of derivation applies for node 6 as well.

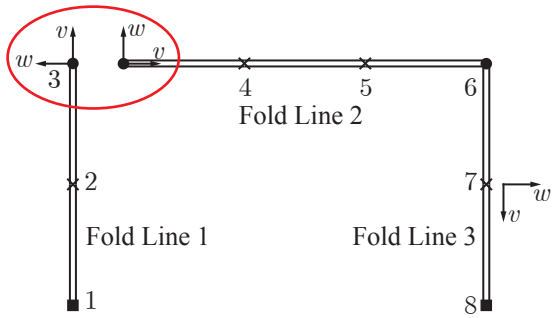

Figure 5.3: w^3 equals local shifting v in fold line 2 with a opposite sign

For a general case where fold lines do not meet at 90 degrees, it can still be shown that w of natural nodes (or intersections of fold lines) can be derived from v of adjacent fold lines from the kinematics in Figure 5.4 and Eq. (5.1.6). Since v of fold lines are already taken into account in Eq. (5.1.2a) and Eq. (5.1.4a), these equations with intersections are linearly dependent on those equations (w^3 and w^6 in our example):

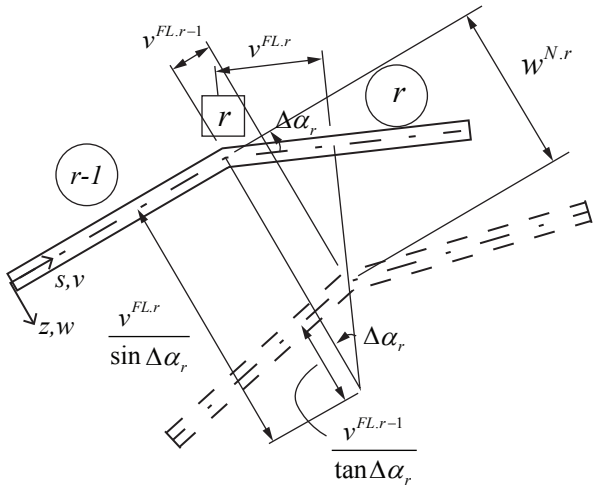

Figure 5.4: Dependence of w at natural node upon v of adjacent fold lines

$$w^r = \frac{v^{FL.r}}{sin\Delta\alpha_r} - \frac{v^{FL.r-1}}{tan\Delta\alpha_r} \tag{5.1.6}$$

Overall, the linear system in Step 2 is equivalent to the linear system in Step 1, as shown in Eq. (5.1.7). The kinematical relations are: (i) Vlasov's assumption makes v a constant in each fold line; (ii) w of any natural node (intersection of fold lines) is dependent upon v of adjacent fold lines. Hence, 9 linearly independent equations exist to solve for 9 unknowns (ϕ_2~ϕ_{10}), and the Step 2 system is linearly determined.

$$\sum_{k=2}^{n}\begin{bmatrix} v_k^{FoldLine} \\ w_k^{Inter.Node}\end{bmatrix}\{\phi_k\}=\begin{bmatrix} v^{FoldLine} \\ w^{Inter.Node}\end{bmatrix}\Leftrightarrow\sum_{k=2}^{n}\begin{bmatrix} v_k \\ w_k\end{bmatrix}\{\phi_k\}=\begin{Bmatrix} v \\ w\end{Bmatrix} \tag{5.1.7}$$

5.1.1.3 Step 3 - Expressing linear system in Step 2 in the global coordinate system

In Step 3, all the coordinates of Step 2 are written in the global coordinate system:

$$\cdot\begin{bmatrix} V_2^1 & V_3^1 & ... & V_{10}^1 \\ V_2^2 & V_3^2 & ... & V_{10}^2 \\ \vdots & \vdots & \vdots & \vdots \\ V_2^8 & V_3^8 & ... & V_{10}^8\end{bmatrix}\begin{Bmatrix}\phi_2 \\ \phi_3 \\ \vdots \\ \phi_{10}\end{Bmatrix}=\begin{Bmatrix} V^1 \\ V^2 \\ \vdots \\ V^8\end{Bmatrix}, \tag{5.1.8a}$$

$$\begin{bmatrix} W_2^1 & W_3^1 & ... & W_{10}^1 \\ W_2^2 & W_3^2 & ... & W_{10}^2 \\ \vdots & \vdots & \vdots & \vdots \\ W_2^8 & W_3^8 & ... & W_{10}^8\end{bmatrix}\begin{Bmatrix}\phi_2 \\ \phi_3 \\ \vdots \\ \phi_{10}\end{Bmatrix}=\begin{Bmatrix} W^1 \\ W^2 \\ \vdots \\ W^8\end{Bmatrix}. \tag{5.1.8b}$$

Compactly:

$$\sum_{k=2}^{n}\begin{bmatrix} V_k \\ W_k\end{bmatrix}\{\phi_k\}=\begin{Bmatrix} V \\ W\end{Bmatrix}. \tag{5.1.9}$$

The concept of coordinate transformation is used to prove the equivalence between Stage 3 and Stage 2. Equations for an arbitrary node r in Stage 2 and Stage 3 are respectively:

$$\begin{bmatrix} v_k^r \\ w_k^r\end{bmatrix}\{\phi_k\}=\begin{Bmatrix} v^r \\ w^r\end{Bmatrix}, \tag{5.1.10}$$

$$\begin{bmatrix} V_k^r \\ W_k^r\end{bmatrix}\{\phi_k\}=\begin{Bmatrix} V^r \\ W^r\end{Bmatrix}. \tag{5.1.11}$$

Multiplying both sides of Eq. (5.1.10) by the coordinate transformation matrix between global and local coordinate systems (see Figure 5.5), Eq. (5.1.12) is acquired:

$$\begin{bmatrix} \cos\alpha & \sin\alpha \\ -\sin\alpha & \cos\alpha\end{bmatrix}\begin{bmatrix} V_k^r \\ W_k^r\end{bmatrix}\{\phi_k\}=\begin{bmatrix} \cos\alpha & \sin\alpha \\ -\sin\alpha & \cos\alpha\end{bmatrix}\begin{Bmatrix} V^r \\ W^r\end{Bmatrix} \tag{5.1.12}$$

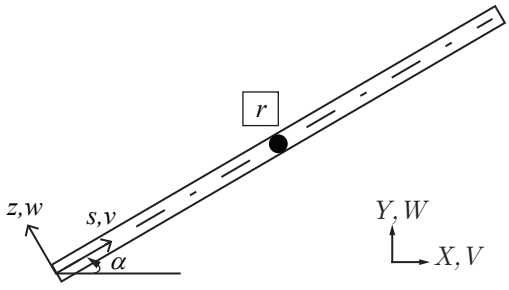

Figure 5.5: Coordinate transformation between global and local coordinate system

Because the coordinate transformation matrix is always invertible (the determinant of it is $\cos^2\alpha + \sin^2\alpha = 1$), Eq. (5.1.10) can be derived from Eq. (5.1.12). Applying the same derivation to all nodes, it is shown that Step 3 is equivalent to Step 2, as shown in Eq. (5.1.13):

$$\sum_{k=2}^{n} \begin{bmatrix} v_k \\ w_k \end{bmatrix} \{\phi_k\} = \begin{Bmatrix} v \\ w \end{Bmatrix} \Leftrightarrow \sum_{k=2}^{n} \begin{bmatrix} V_k \\ W_k \end{bmatrix} \{\phi_k\} = \begin{Bmatrix} V \\ W \end{Bmatrix} \tag{5.1.13}$$

5.1.1.4 Step 4 - Realizing that Vlasov's assumption is not strictly applicable to FEA/experimental results, and transferring the linear system in Step 3 to a least squares problem

Generalized Beam Theory adopts Vlasov's assumption, which puts constraints on the local translation v in each fold line. However, in finite element analysis or test-measured point clouds, this constraint does not exist. Specifically, due to the presence of transverse membrane strain, local displacement v is not strictly constant (for better interpretation, Fig. 13 can be observed, as it shows a numerical example).

Because the transverse extension strain is always present in FEA or test-based measurement for a general case, no matter whether the 'GBT stiffness matrix method' or the method of this paper is used, the displacement fields cannot be perfectly reconstructed by GBT modes (in the context of conventional GBT modes without 'transverse extension' modes), and the Step 3 equation is now overdetermined. However, since the influence of transverse extension is minimal, GBT modal amplitudes can be found by reformulating Eq. (5.1.9) as a linear least squares problem

$$\min\left(\left|\sum_{k=2}^{n} \begin{bmatrix} V_k \\ W_k \end{bmatrix} \{\phi_k\} - \begin{Bmatrix} V \\ W \end{Bmatrix}\right|\right) \qquad \text{or} \qquad \sum_{k=2}^{n} \begin{bmatrix} V_k \\ W_k \end{bmatrix} \{\phi_k\} \overset{\substack{least \\ square}}{=} \begin{Bmatrix} V \\ W \end{Bmatrix}. \tag{5.1.14}$$

This operation projects the in-plane displacement fields (V and W obtained from FEA for example) onto the sub-space of GBT solutions , as shown in Figure 5.6.

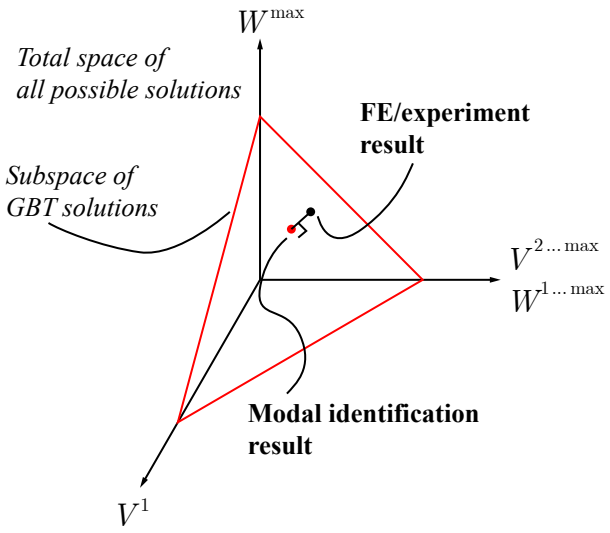

Figure 5.6: Displacement field projection for calculating $\{\phi_k\}$

5.1.1.5 Summary: four-step justification of modal amplitudes calculation method

The four-step justification modal amplitude calculation method is summarized in Eq. (5.1.15). The equivalence of Step 1 and 2 results because of GBT kinematics, and for Steps 2 and 3 by coordinate transformation. Any equation in the first three steps will generate the exact solution of the modal amplitudes vector if the in-plane displacement field falls in the subspace of GBT solutions. The linear system in Step 3 is transferred to a least squares problem in Step 4 because of the presence of transverse extension. One reason for providing this four-step example is to show that the scheme is made possible by the rationality of GBT kinematics; otherwise the Step 4 equation generally does not give a satisfactory solution as a purely mathematical problem, because the number of objectives (2n, e.g., 16 in the example above) to be optimized is more than the number of input arguments (n+1, e.g., 9 in the example above).

$$\begin{aligned}\left(\sum_{k=2}^{n}\begin{bmatrix}v_k^{FoldLine}\\ w_k^{Inter.Node}\end{bmatrix}\{\phi_k\}=\begin{bmatrix}v^{FoldLine}\\ w^{Inter.Node}\end{bmatrix}\right)&\Leftrightarrow\left(\sum_{k=2}^{n}\begin{bmatrix}v_k\\ w_k\end{bmatrix}\{\phi_k\}=\begin{Bmatrix}v\\ w\end{Bmatrix}\right)\\ \Leftrightarrow\left(\sum_{k=2}^{n}\begin{bmatrix}V_k\\ W_k\end{bmatrix}\{\phi_k\}=\begin{Bmatrix}V\\ W\end{Bmatrix}\right)&\Rightarrow\left(\sum_{k=2}^{n}\begin{bmatrix}V_k\\ W_k\end{bmatrix}\{\phi_k\}\overset{\substack{least\\ square}}{=}\begin{Bmatrix}V\\ W\end{Bmatrix}\right)\end{aligned}\tag{5.1.15}$$

5.1.1.6 Modal participation factors and error evaluation8

Formulae to calculated modal participation factors using modal amplitudes have been introduced in Chapter 2

$$P_k = \frac{\int_L |g_k \phi_k(x)| dx}{\sum_{k=1}^{n} \int_L |g_k \phi_k(x)| dx}, \tag{5.1.16}$$

$$p_k(x) = \frac{|g_k \phi_k(x)|}{\sum_{k=1}^{n} |g_k \phi_k(x)|}. \tag{5.1.17}$$

Once the modal amplitudes of discrete cross-sections along the member are obtained as described in the previous section, Eq. (5.1.1), modal participation can be determined by the discrete form of Eq. (5.1.16), Eq. (5.1.17), as shown in Eq. (5.1.18) and Eq. (5.1.19):

$$P_k = \frac{\sum_{section=1}^{N} |g_k \phi_k(x)| dx}{\sum_{k=1}^{n} \sum_{section=1}^{N} |g_k \phi_k(x)| dx}, \tag{5.1.18}$$

$$p_k(x) = \frac{|g_k \phi_k(x)|}{\sum_{k=1}^{n} |g_k \phi_k(x)|}. \tag{5.1.19}$$

The error of the reconstructed displacement field can be evaluated by

$$error = \sqrt{\frac{\sum[(V_{SFEA} - V_{reconstructed})^2 + (W_{SFEA} - W_{reconstructed})^2]}{\sum({V_{SFEA}}^2 + W_{SFEA}^2)}}, \tag{5.1.20}$$

where $\sum$ means it applies to all the discretization nodes; V_{SFEA}, W_{SFEA} are out-of-plane displacement components read from shell finite element solution; $V_{reconstructioned}, W_{reconstructed}$ are reconstructed displacement components calculated by using $\phi_{k-reconstructed}$.

5.1.2 Reconstruction of GBT modal amplitude field

By retrieving the modal amplitudes at discrete cross-section, the out-of-plane displacement - (v, w) or (V, W) in Figure 3.1 - can be decomposed into modal contributions by knowing Eq. (5.1.15). The objectives of this section include the decomposition of displacement,

strain energy and bending stress regarding the contribution from GBT modes. From Eq. (3.4.23)˜ Eq. (3.4.26) and Eq. (3.4.93), that requires the information of full variation of modal amplitude. To retrieve modal amplitudes field, it is assumed $\phi_k(x)$ can be piece-wisely approximated by polynomials like shown in (Eq. (3.4.88)). The member is divided into several sub-domains each containing 4 discrete cross-sections, as shown in Figure 5.7. Because Hermitian polynomial is used to approximate $\phi_k(x)$, (Eq. (3.4.88)) applies and

$$\begin{aligned}
&\phi_k(0) = \psi_1(0)d_{k.1} + \psi_2(0)d_{k.2} + \psi_3(0)d_{k.3} + \psi_4(0)d_{k.4},\\
&\phi_k(1/3L^e) = \psi_1(1/3L^e)d_{k.1} + \psi_2(1/3L^e)d_{k.2} + \psi_3(1/3L^e)d_{k.3} + \psi_4(1/3L^e)d_{k.4},\\
&\phi_k(2/3L^e) = \psi_1(2/3L^e)d_{k.1} + \psi_2(2/3L^e)d_{k.2} + \psi_3(2/3L^e)d_{k.3} + \psi_4(2/3L^e)d_{k.4},\\
&\phi_k(L^e) = \psi_1(L^e)d_{k.1} + \psi_2(L^e)d_{k.2} + \psi_3(L^e)d_{k.3} + \psi_4(L^e)d_{k.4},
\end{aligned} \tag{5.1.21}$$

where L^e denotes the domain under consideration; $\phi_k(\alpha L^e)$ is modal amplitude calculated by Eq. (5.1.15) at x; $\psi_i(\alpha L^e)$ corresponds to the value of i^{th} Hermitian shape function ((Eq. (3.4.88)), Figure 3.10) at the location αL^e; $d_{k,i}$ denotes the i^{th} FE degree-of-freedom of the k^{th} GBT mode ((Eq. (3.4.88)), Figure 3.10). d_k can be solved for by using Eq. (5.1.22) and the continuous distribution of ϕ_k is approximated. The concept is depicted in Figure 5.7.

$$\begin{Bmatrix} d_{k.1} \\ d_{k.2} \\ d_{k.3} \\ d_{k.4} \end{Bmatrix} = \begin{bmatrix} \psi_1(0) & \psi_2(0) & \psi_3(0) & \psi_4(0) \\ \psi_1(1/3L^e) & \psi_2(1/3L^e) & \psi_3(1/3L^e) & \psi_4(1/3L^e) \\ \psi_1(2/3L^e) & \psi_2(2/3L^e) & \psi_3(2/3L^e) & \psi_4(2/3L^e) \\ \psi_1(L^e) & \psi_2(L^e) & \psi_3(L^e) & \psi_4(L^e) \end{bmatrix}^{-1} \begin{Bmatrix} d_{k.1} \\ d_{k.2} \\ d_{k.3} \\ d_{k.4} \end{Bmatrix} . \tag{5.1.22}$$

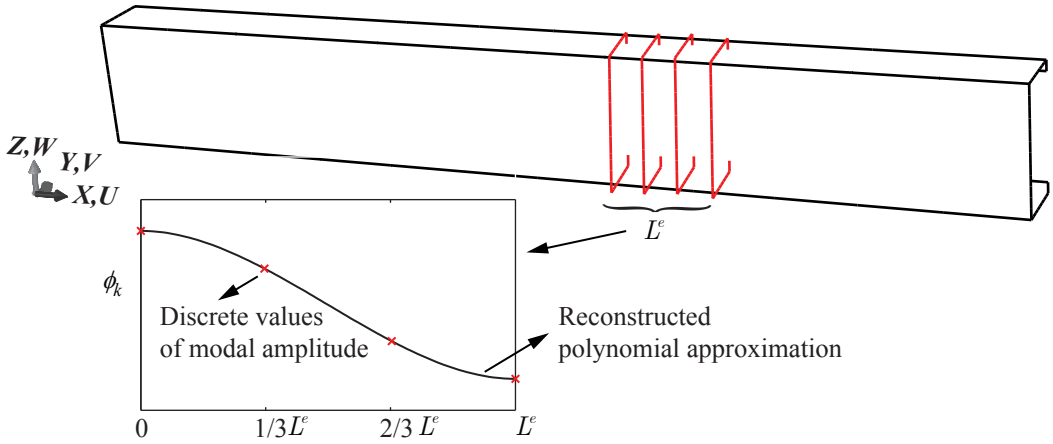

Figure 5.7: Concept of using polynomials to piece-wisely approximate the modal amplitude ϕ_k.

5.1.3 Decomposition of strain energy and bending stresses

The energy stored in the interaction of conventional mode i and k is

$$E_{ik} = \frac{1}{2} d_i k_{ik} d_k, \tag{5.1.23}$$

where k_{ik} stands for the linear, interactive stiffness matrix of mode i and k as shown in Eq. (3.4.93); d_i, d_k are the finite element degree of freedom vectors for the domain where piece-wise approximation is applied; shear-warping modes are not considered. Obviously E_{ii} stands for the energy stored in mode i. And the strain energy in total is

$$E_{total} = \sum_i \sum_k E_{ik}. \tag{5.1.24}$$

Strain energy can be used as an ambiguous modal participation indicator because the strain energy distribution is independent with the GBT mode normalization. The transverse and longitudinal bending stress, according to Eq. (3.4.23)˜ Eq. (3.4.26), they are

$$\sigma^F_{ss}(x,s,t) = \frac{E}{1-\nu^2} w_{k,ss}(s,t)\phi_k(x) + \frac{\nu E}{1-\nu^2} w_k(s,t)\phi_{k,xx}(x), \tag{5.1.25}$$

$$\sigma^F_{xx}(x,s,t) = \frac{\nu E}{1-\nu^2} w_{k,ss}(s,t)\phi_k(x) + \frac{E}{1-\nu^2} w_k(s,t)\phi_{k,xx}(x), \tag{5.1.26}$$

$$\sigma^M_{xx}(x,s,0) = E u_k(s,0)\phi_{k,x}(x), \tag{5.1.27}$$

where summation convention applies; σ^F_{ss}, σ^F_{xx} and σ^M_{xx} denote transverse, longitudinal bending stresses and longitudinal membrane respectively; w_k, u_k are plate transverse defection and longitudinal warping component of the k^{th} GBT mode shape as inEq. (3.4.13), and ϕ_k is the k^{th} GBT mode amplitude that can be obtained by using d_k and (Eq. (3.4.88)).

5.2 Summary

This chapter introduced buckling mode decomposition of normalized displacements, bending stresses, and strain energy from any thin-walled structure interactive eigen-buckling solution is performed with GBT. Normalized displacement field, bending stress components and strain energy can all be reconstructed with quantitative participation known that can be useful for future design approaches. The method first extracts GBT modal amplitudes at discrete cross-sections and then reconstructs the continuous modal amplitude field piecewisely using polynomials. The normalized displacement field, bending stresses and strain energy are all retrieved and decomposed using GBT modal amplitude field and associated GBT constitutive laws.

Chapter 6

Applications of Buckling Mode Decomposition

The purpose of this chapter is to enable engineers with the ability to utilize buckling mode decomposition method derived in Chapter 4, either for finding global, distortional and local dominating elastic buckling modes for strength prediction using current method, or obtaining the modal participation information for interactive buckling strength prediction using this dissertation's method. The goal is to free engineers from needing to know the specifics of Generalized Beam Theory but being able to draw modal participation information from an elastic buckling mode.

The benefits of this proposed method are explicit. First, the input of the method uses only out-of-plane displacement at discrete measuring nodes, which are measurable for engineers because the out-of-plane displacement components are much larger than that of warping displacement. Second, even though merely displacements at discrete nodes are used, a fully continuous stress field can be reconstructed and decomposed, as well as the strain energy decomposed for the whole member (the warping energy is included even though warping displacement is not required as an input).

Currently, the method applies to eigen buckling and is not yet fully applicable for progressive loading. The displacement decomposition and bending stress composition can be readily applied to progressive loading because displacement field can still be viewed as superposition of basis functions. Meanwhile, the modal contribution for normal stress and energy become coupled and the nonlinearity must be accounted for. Also, the energy stored in uniform compression become significant for progressive loading and need to be included. Nevertheless, the work paves the road for mode decomposition of progressive loading and the author intends to work on that later.

6.1 Modal identification for shell finite element results

6.1.1 Example 1 – thin-walled lipped Cee-section column

For the first illustrative example, modal identification is carried out on the result of an FEA eigen-buckling analysis of a column. The column cross section is the Cee shown in Figure 4.3, with the thickness of the channel being t = 2mm and the member length being L = 1240mm. The cross section is discretized into 32 sub-segments (two equally wide pieces in each flange lip, eight equally wide pieces in each flange, and 12 equally wide pieces in the web) for GBT cross-sectional analysis. A total of 35 GBT mode shapes are produced, and the first nine GBT mode shapes are shown in Figure 4.3.

To obtain the displacement field for performing modal identification, a shell finite element analysis (SFEA) is conducted using the commercial finite element program ABAQUS [120]. The first 50 eigen-buckling solutions are recorded for further analysis. The member is meshed into 3936 rectangular elements. In the cross-sectional plane, the discretization is identical with GBT (shown in Figure 6.1). In the longitudinal direction, the discretization is made every 10 mm, which results in 124 cross sections. The ABAQUS S4 element with finite membrane strain is used. In-plane translations (U_x, U_z) of nodes on both ends are fixed, and the longitudinal warping (U_y) is prescribed at all nodes on the mid-length cross section. Shell edge tractions $q = 3.846 N/mm$ are applied to both ends of the member, which corresponds to $1000N$ of compression force. FEA modal is shown in Figure 6.1 and buckling modes in Figure 6.2.

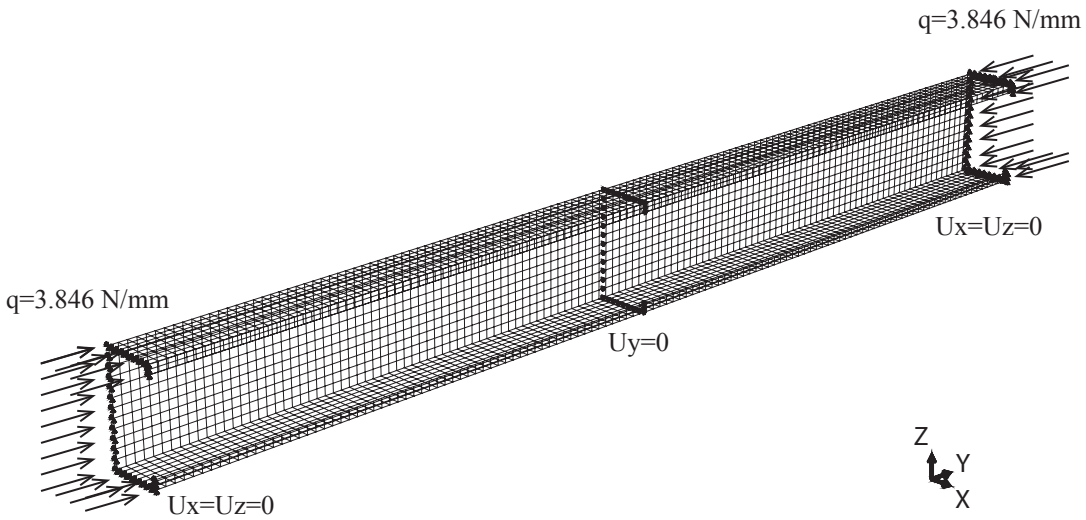

Figure 6.1: Example 1 - FEA modal boundary conditions

The displacement fields generated by SFEA are treated as input for the 'Buckling Cracker'. Modal participation and errors are evaluated by the code and shown in Table 6.1. Also, buckling mode shapes and corresponding modal amplitudes of the first five buckling modes are shown in Figure 6.2.

Table 6.1: Example 1 - Modal participation and error for the first 10 buckling modes

Buckling mode from FEA	GBT mode							error (%)
	2G	3G	4G	5D	6D	7L	8-35L	
1	0.0	0.7	0.0	59.4	0.0	36.7	3.1	0.058
2	0.0	0.4	0.0	28.1	0.0	66.3	5.1	0.077
3	0.0	0.9	0.0	84.3	0.0	12.5	2.2	0.048
4	0.0	0.3	0.0	29.9	0.0	64.5	5.4	0.078
5	0.0	0.4	0.0	30.7	0.0	64.9	4.0	0.076
6	0.0	0.3	0.0	15.1	0.0	77.2	7.4	0.081
7	0.0	0.5	0.0	42.6	0.0	53.4	3.5	0.075
8	0.0	0.4	0.0	39.2	0.0	54.6	5.8	0.078
9	0.0	0.7	0.0	65.6	0.0	29.8	4.0	0.069
10	0.0	0.4	0.0	47.7	0.0	47.2	4.6	0.090

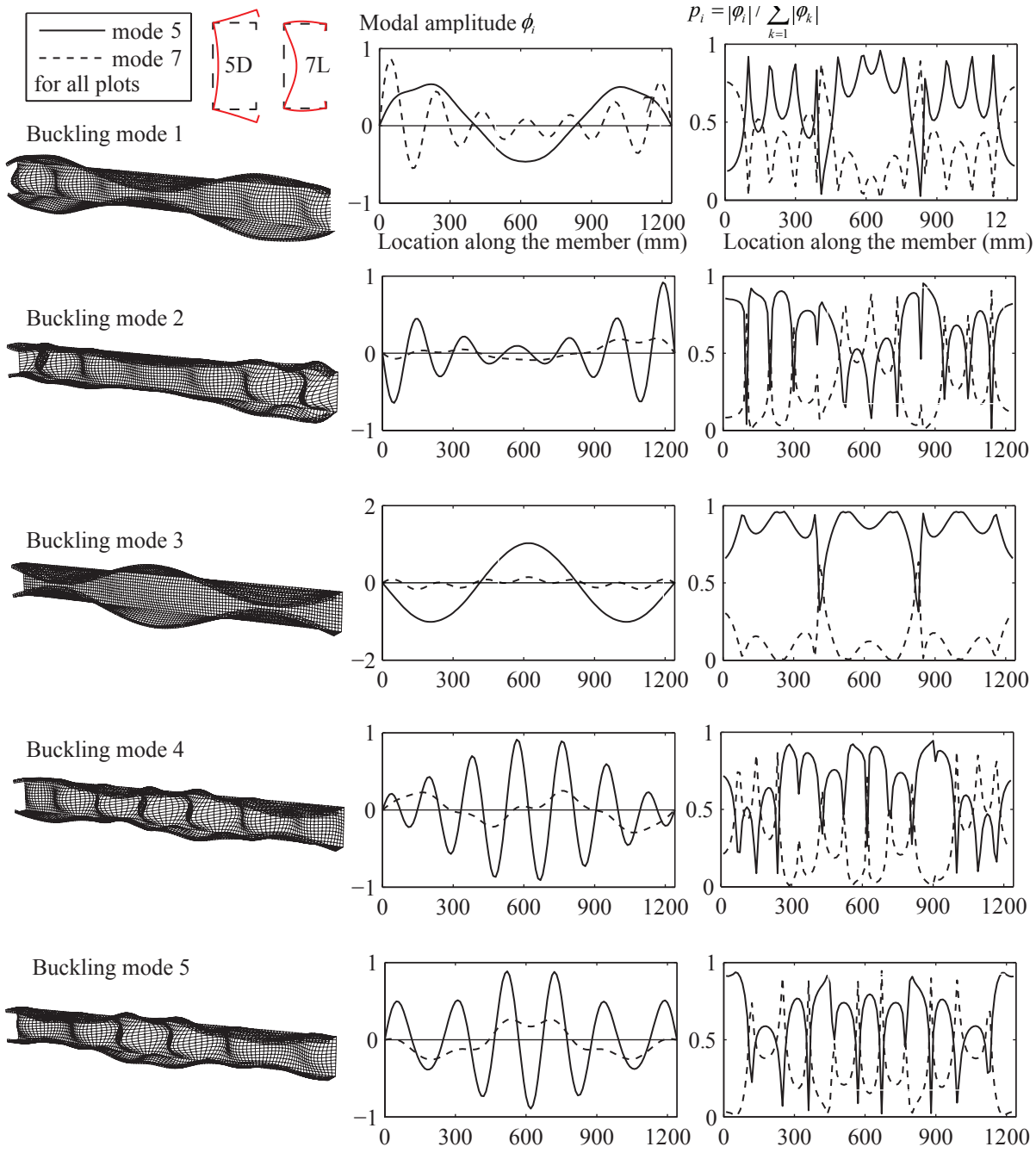

Figure 6.2: Example 1 - Buckling shapes and modal amplitudes of first five buckling modes (modal amplitude has no unit and the unit of length is associated with GBT mode shapes)

From Table 6.1 and Figure 6.2, it can be concluded that: (i) the largest normalized error between reconstructed displacement fields and displacement fields from FEA evaluated using Eq. (26) is 0.090%; (ii) FEA buckling modes 1˜10 are distortional buckling modes dominated

by GBT mode 5 or mode 7 respectively; (iii) GBT mode 5 (distortional) and mode 7 (local) are the two most significant modes for FEA buckling modes 1˜5; (iv) the varying trends of GBT mode amplitudes along the member agree with visual inspection. Taking FEA mode 3 from Figure 6.2 for example, the flanges of the Cee are 'closing - opening - closing' from the left end to the right, which is reflected by the amplitude of mode 5 - 'negative - positive - negative'.

Another ability of the modal identification scheme is to decompose the in-plane deformation into combinations of pure modes. The mid-length cross section for buckling mode 1 in Figure 6.2 are shown in Figure 6.3 demonstrating that the reconstructed displacement fields can be decomposed into contributions of pure modes.

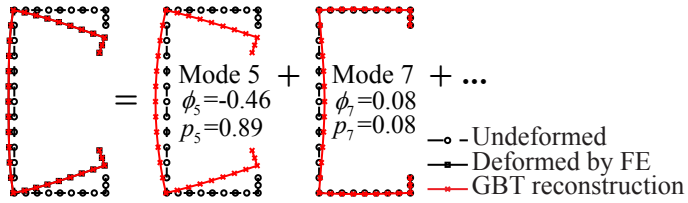

Figure 6.3: Disp. field reconstruction and decomposing into GBT modes contributions for mid cross section in buckling mode 1

Figure 6.4 shows the cross section in Figure 6.3 redepicted with annotation of local displacement v. It is seen that v are close but not strictly the same in each fold line, which 'shifts' the displacement fields slightly out of the sub-domain of GBT solutions. It can be observed the v displacement by GBT reconstruction is constant in each fold line as discussed above.

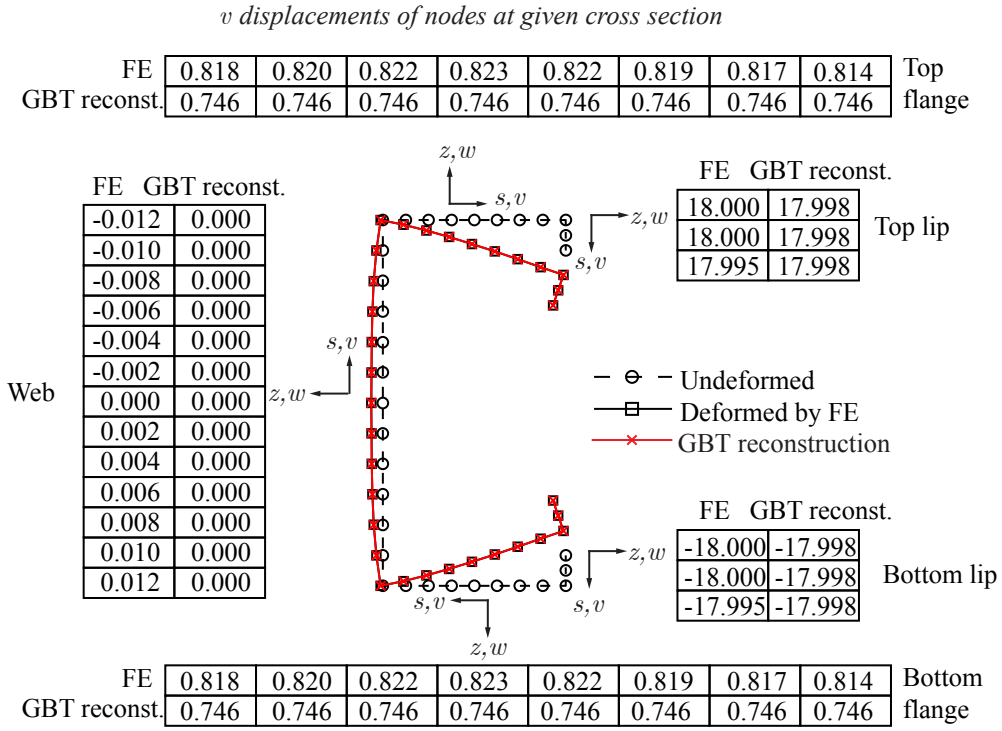

Figure 6.4: Displacement v for mid cross section in buckling mode 1

6.1.2 Example 2 – thin-walled lipped Cee-section beam-column

The second example is conducted on the same structural member and FEA mesh in example 1 but now serving as a beam-column. The left end of the member is fixed against warping for this second analysis. A shell edge traction of $q = 16.6667 N/mm$ is applied to the top flange of the right end. Loading and boundary conditions are shown in Figure 6.5.

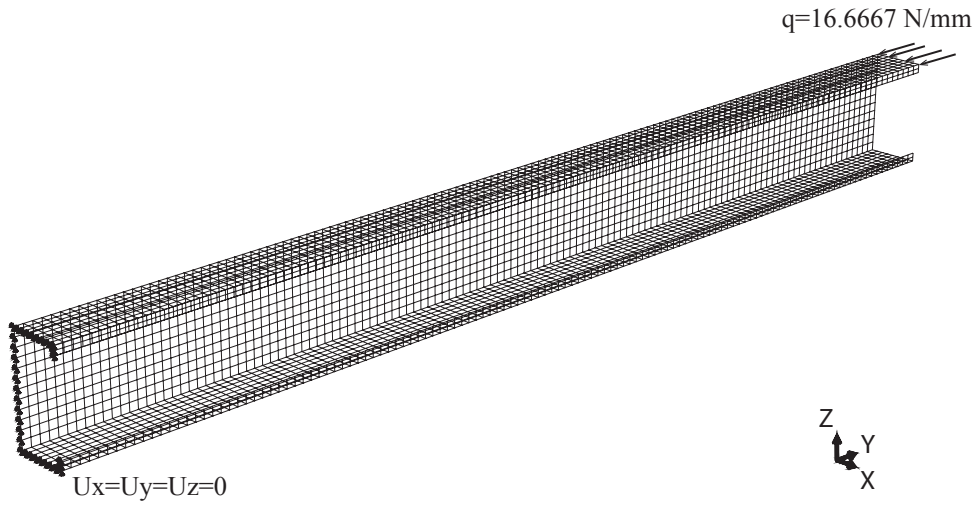

Figure 6.5: Example 2 - FEA modal boundary conditions

Modal participation and error are evaluated by 'Buckling Cracker' and shown in Table 6.2. Also, buckling mode shapes and corresponding modal amplitudes of the first five buckling modes are shown in Figure 6.6.

Table 6.2: Example 2 - Modal participation and error for the first 10 buckling modes

Buckling mode from FEA	GBT mode						error (%)
	2G	3G	4G	5D	6D	7-35L	
1	4.34	21.25	0.72	50.21	22.50	0.97	0.018
2	0.62	20.73	0.40	47.41	29.78	1.05	0.024
3	0.26	2.49	0.01	58.55	37.84	0.84	0.061
4	0.21	2.12	0.02	59.49	37.26	0.90	0.061
5	0.29	3.14	0.03	61.50	34.12	0.92	0.055
6	0.32	3.08	0.03	60.60	34.72	1.24	0.064
7	0.70	4.44	0.01	56.77	36.10	1.98	0.077
8	1.69	8.27	0.02	56.63	31.18	2.22	0.051
9	2.56	10.71	0.05	58.83	26.66	1.19	0.034
10	2.98	11.21	0.07	55.75	27.39	2.60	0.038

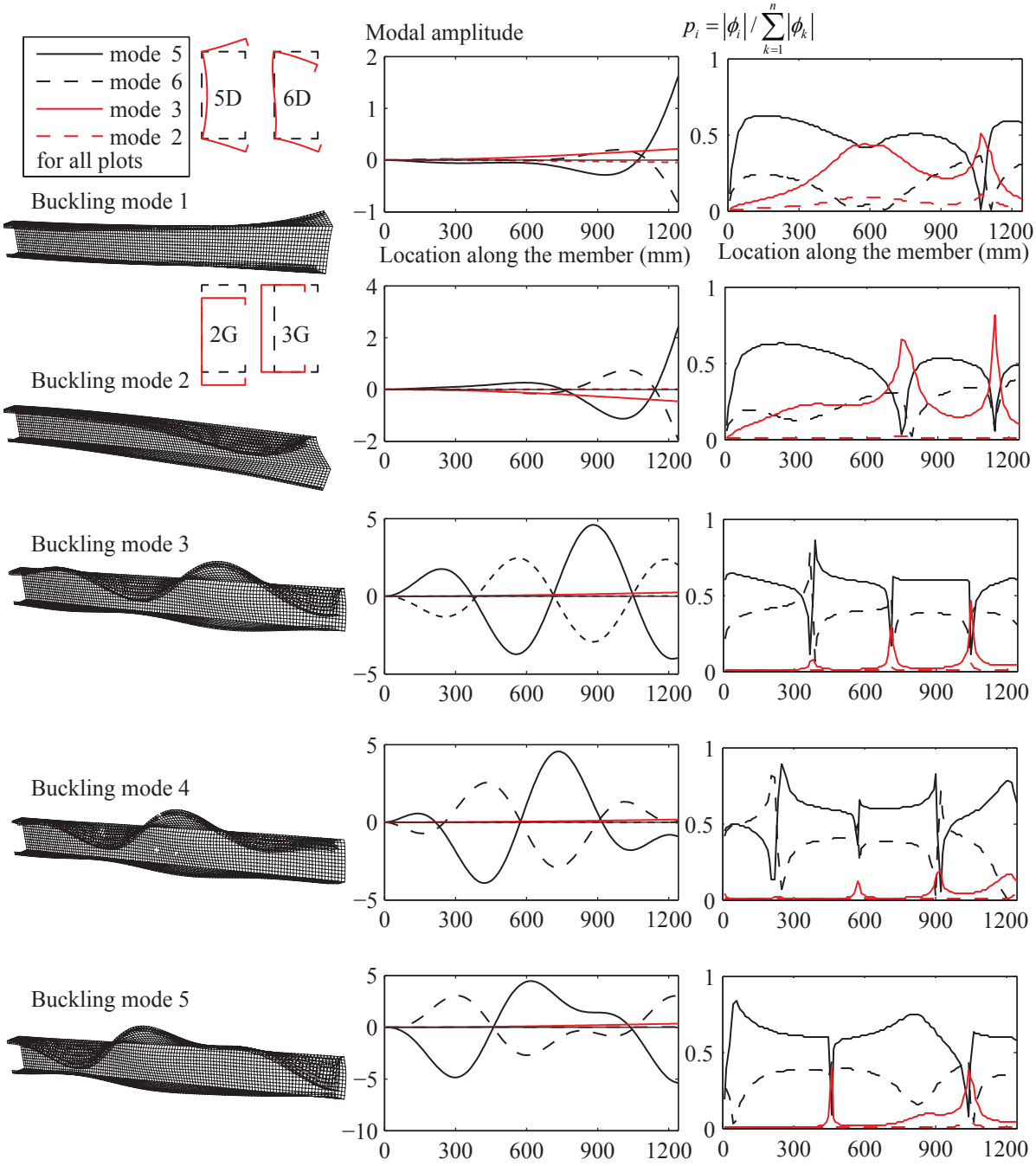

Figure 6.6: Example 2 - Buckling shapes and modal amplitudes of first 5 buckling modes (modal amplitude has no unit and the unit of length is associated with GBT mode shapes)

From Table 6.2 and Figure 6.6, it can be concluded that: (i) the largest error between reconstructed displacement fields and displacement fields from FEA evaluated using Eq. (26) is 0.077%; (ii) FEA buckling modes 1˜10 are distortional buckling modes with domination

by GBT mode 5 (distortional); (iii) GBT mode 5 and mode 6 (distortional) are the two most significant modes for FEA buckling modes 1~5; (iv) varying trends of GBT mode amplitudes along the member agree with visual inspection.

6.1.3 Example 3

The example is a $870\,mm$ long member with the same cross-section as in the previous example (see Figure 4.3). The member is warping-fixed at the left end and pinned-warping fixed at the right, and loaded with a compressive traction q at the pinned-warping free end. For shell finite-element modeling in ABAQUS, the discretization is identical with GBT in the cross-sectional directions, as shown in Figure 4.3. In longitudinal direction, the discretization is made every $10mm$. The lowest buckling load is $146.4kN$ and the out-of-plane displacements (V, W in Figure 3.1) of all the discretization nodes are read from ABAQUS for modal decomposition analysis.

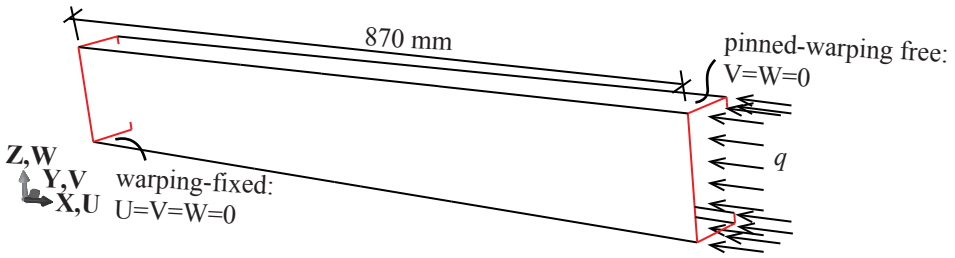

Figure 6.7: Example III: dimensions and loading/boundary conditions.

Reconstructed modal amplitudes and participations along the member are retrieved by using Eq. (5.1.1) and Eq. (5.1.22) and shown in Figure 6.8. The error of the reconstructed out-of-plane displacement field is 0.08% according to Eq. (5.1.20). Local mode 7 is dominant as shown in Figure 6.8 and the variation of its amplitude in Figure 6.8a is consistent with the buckling shape in Figure 6.10. For member-wise out-of-plane displacement participation, they read $P_7 = 70.9\%$ and$P_5 = 24.9\%$ by using Eq. (5.1.18). Distortional buckling occurs (mode 5) and mixes with local buckling. The strain energy decomposition is conducted per Eq. (5.1.23) as shown in Figure 6.9, where the grid (i, j) indicates the strain energy stored in the interaction of mode i and j. The total strain energy is computed to be $1518.8N \cdot mm$ according to Eq. (5.1.24), comparing to ABAQUS yielding of $1468.4N \cdot mm$ (3.4% difference). It is confirmed that energy-wise mode 7 dominates as it contributes to 94.2% of the strain energy.

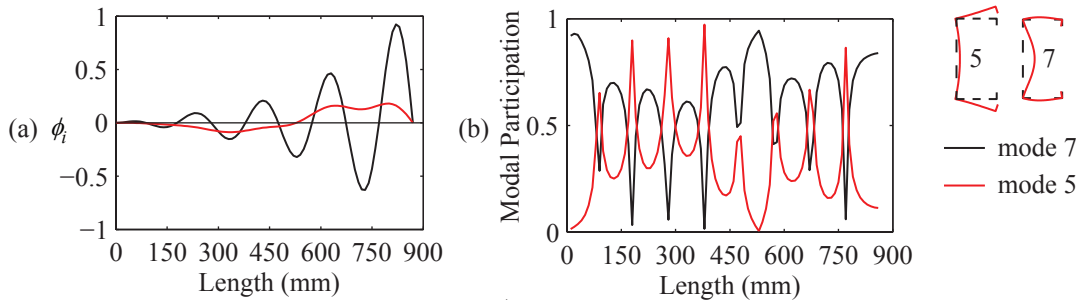

Figure 6.8: Example III: GBT buckling mode amplitudes and modal participation: local buckling along the member.

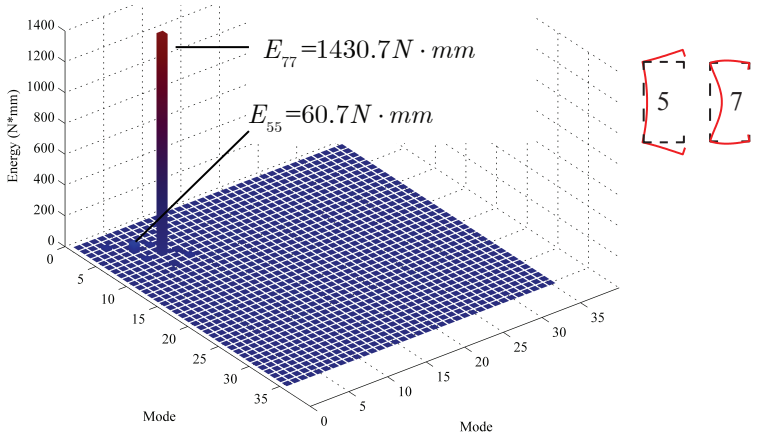

Figure 6.9: Example III: Strain Energy decomposition.

The bending stresses in the transverse and longitudinal directions are reconstructed by using Eq. (5.1.25) and Eq. (5.1.26) respectively. The results are compared with SFEA results in Figure 6.10 and Figure 6.11, SFEA transverse bending stress is read from ABAQUS from the cross-section top fiber positions, because the transverse membrane stress is negligible as assumed by GBT [91]. For SFEA result of longitudinal stress, the bending stress is obtained by taking out the membrane stress from the stress at cross-section top fiber, i.e.,

$$\sigma^F_{xx-FE}(x,s) = \sigma_{xx-FE}(x,s,1/2t) - \sigma_{xx-FE}(x,s,0). \tag{6.1.1}$$

It can be seen the magnitude and distribution of reconstructed stress field are consistent with SFEA result. Because the reconstruction process uses merely the out-of-plane displacement field (V, W in Figure 3.1), it is hoped the method be used in conjunction with 3D displacement field measurement to analyze experiment point cloud in the future. Because small

displacement is considered herein, the bending stress and displacement field can be decomposed into modal contributions and the transverse bending shown is shown in Figure 6.12. For this example the transverse bending stress is dominated by mode 7 (local).

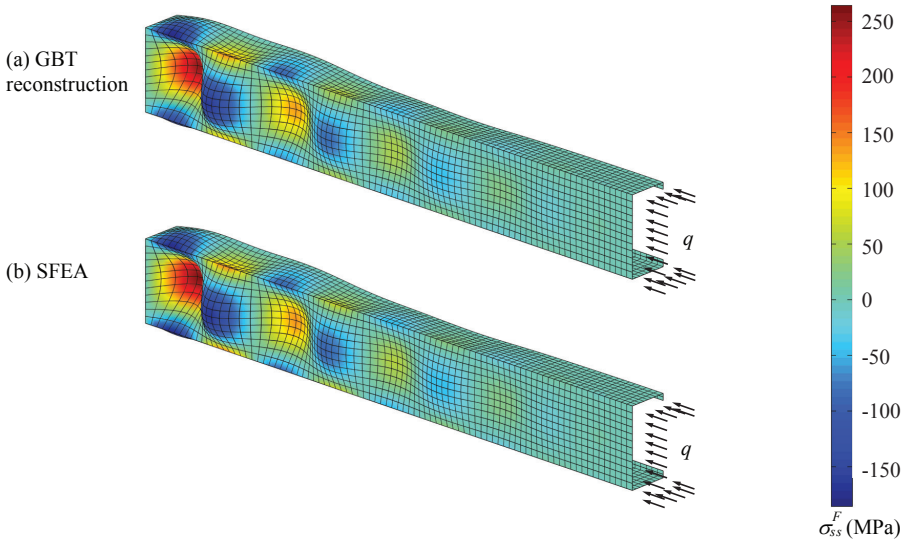

Figure 6.10: Example III: Transverse bending stress comparison for prismatic member: (a) GBT reconstruction; (b) SFEA.

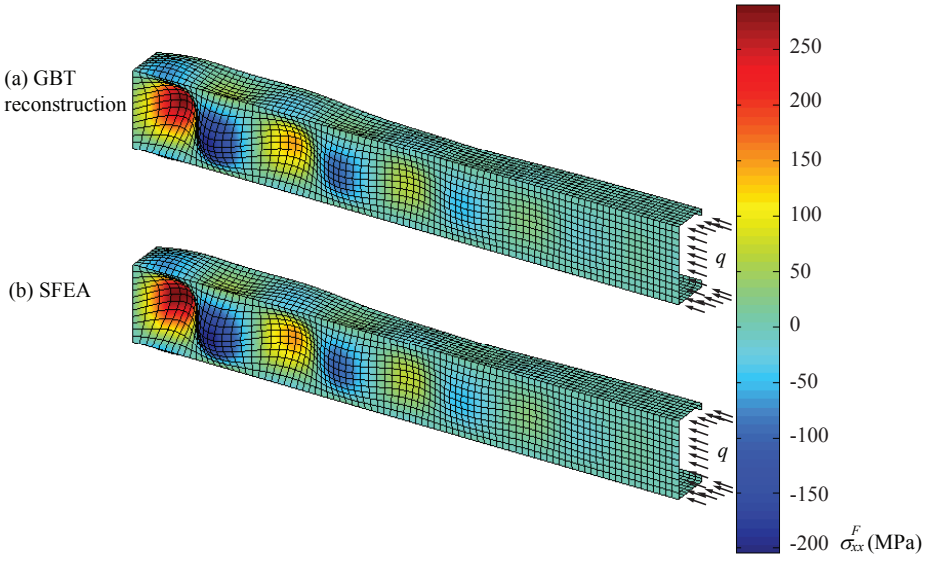

Figure 6.11: Example III: Longitudinal bending stress comparison for prismatic member: (a) GBT reconstruction; (b) SFEA.

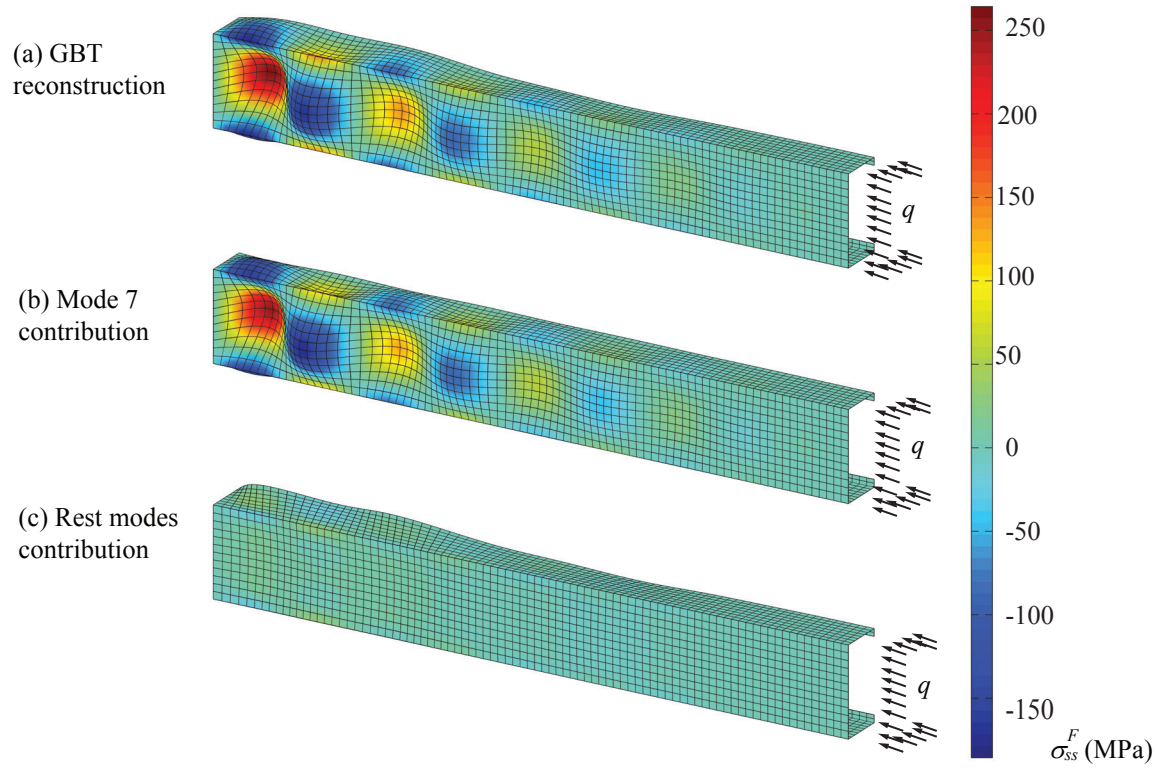

Figure 6.12: Example III: Transverse bending stress decomposition: (a) GBT reconstruction; (b) contribution from mode 7 and (c) contribution from other modes.

6.1.4 Example 4

The example involves a 1260 mm long member pinned-warping free at both ends and loaded at both ends by uniform compression, and warping is prevented from mid-length cross-section in Figure 6.13. The cross-section and material properties are identical to the previous example.

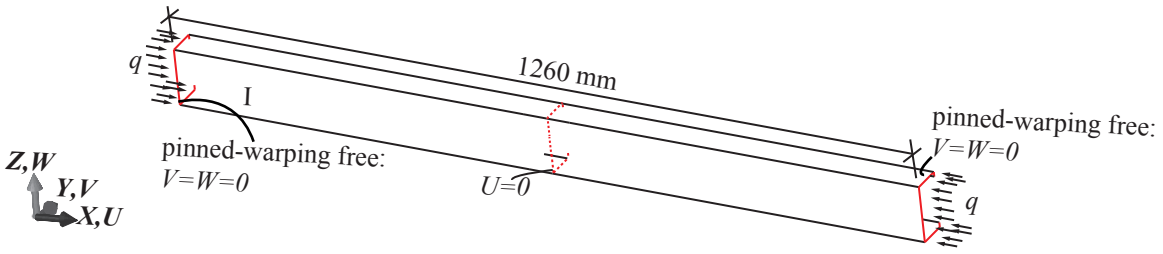

Figure 6.13: Example IV: dimensions and loading/boundary conditions.

The first mode buckling load calculated by GBT is $146.6\,kN$. Modal amplitude and participation along the member are presented in Figure 6.14. It is shown the dominant GBT mode is local buckling (mode 7) mixing with symmetric distortional buckling mode 5, and the variation of ϕ_7, ϕ_5 agree with the mode shape in Figure 6.14, Displacement field error by Eq. (5.1.20) is calculated to be 0.07%. Using Eq. (3.4.105), the member-wise displacement participations read $P_7 = 64.2\%$ and $P_5 = 31.8\%$ for mode 7 and 5 respectively. From strain energy perspective, mode 7 is responsible for 93.9% of the total energy Figure 6.15. Transverse and longditudinal bending stress are also retrieved by using Eq. (5.1.25), Eq. (5.1.26) respectively and shown in Figure 6.16, Figure 6.17. The reconstructed bending stress field are consistent with that read from SFEA.

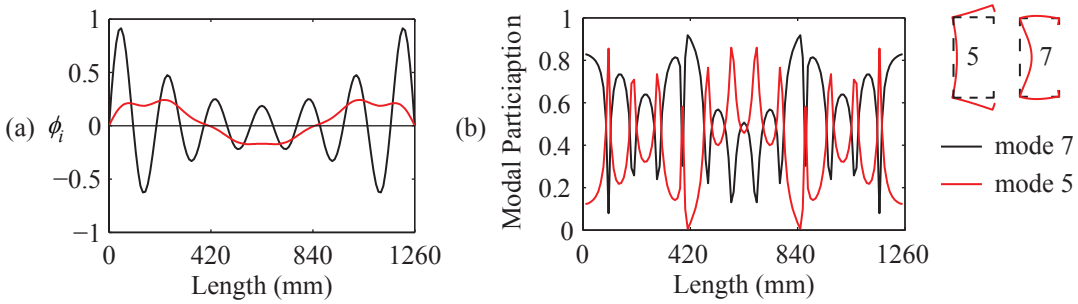

Figure 6.14: Example IV: GBT buckling mode amplitudes and modal participation: local buckling along the member.

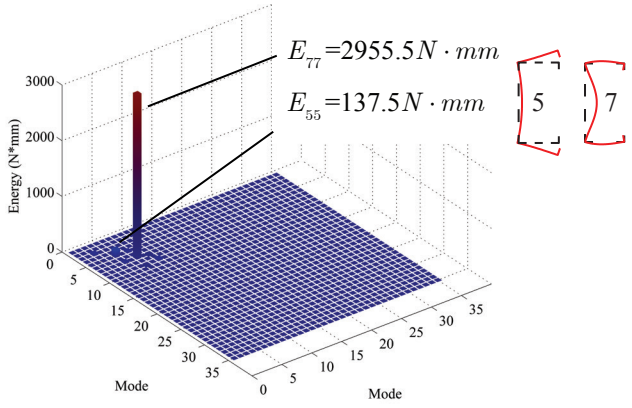

Figure 6.15: Example IV: Strain Energy decomposition

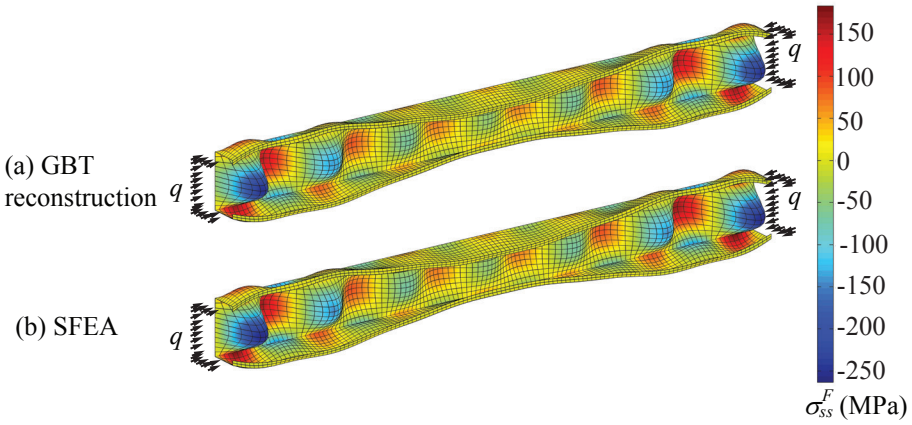

Figure 6.16: Example IV: Transverse bending stress comparison: (a) GBT reconstruction; (b) SFEA.

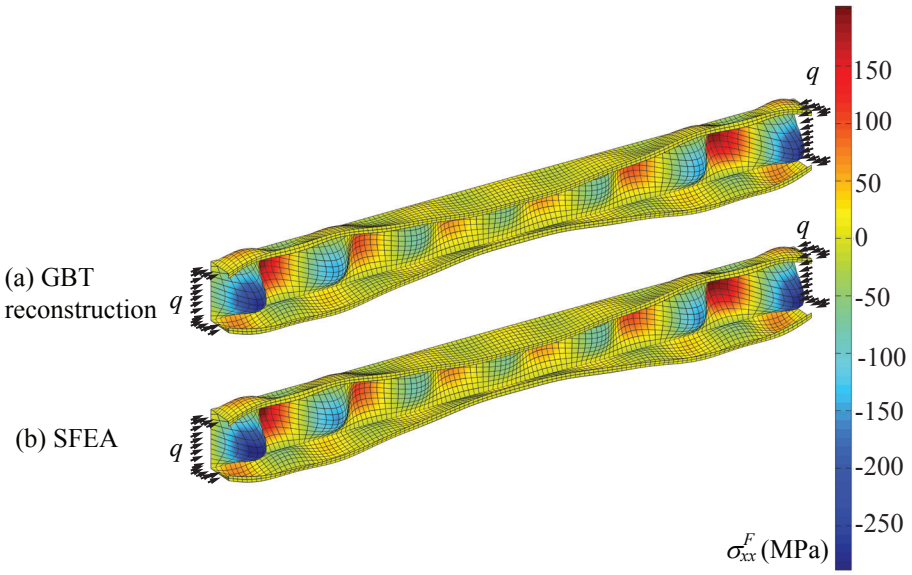

Figure 6.17: Example IV: Longitudinal bending stress comparison: (a) GBT reconstruction; (b) SFEA.

6.2 Modal identification for point clouds

6.2.1 Experimental program

Cold-formed steel 362S162-33 Cee-section studs, 890 mm long between warping fixed supports, were subjected to compression testing until failure as shown in Figure 6.18. Specimen

1 was marked with a grid and Specimen 2 was marked with random dots to explore different techniques for creating the image reconstructions. (A specimen without markings was also tested however the lighting was not adequate to complete the image-based reconstruction, a lesson learned that was adjusted on the following two tests presented here). Full details of the testing program, including tested capacities and load-deformation response, are detailed in [122], [63].

(a) (b)

Figure 6.18: Cold-formed steel stud column test specimens: (a) Specimen 1 with grid pattern and (b) Specimen 2 with random dots applied

For both tests, image reconstruction was performed before loading, at 22 kN of compression, 44 kN (near peak load), and then after peak load at 22 kN again. A digital single-lens reflex (DSLR) Nikon D7100 camera was used to take the specimen pictures with 24 megapixels resolution. At each load step, a sequence of approximately 120 images were taken covering a 360 degree view, making sure to overlap the image frame as each picture was taken. Both specimens experienced local-global buckling with three distortional buckling half-waves forming along the column length and this deformation was captured by the imaged-based reconstruction.

The digital images from each test were input into a commercial computer program called Agisoft PhotoScan [82] which uses Structure From Motion (SFM) techniques [125] to estimate the three-dimensional coordinates of a structure from two-dimensional image sequences. The results from each 3d reconstruction are shown in Figure 6.19 and Figure 6.20.

(a) (b) (c) (d)

Figure 6.19: 3d image-based reconstruction point clouds for Specimen 1: (a) 0 kN, (b) 22 kN, (c) 44 kN, (d) 22 kN

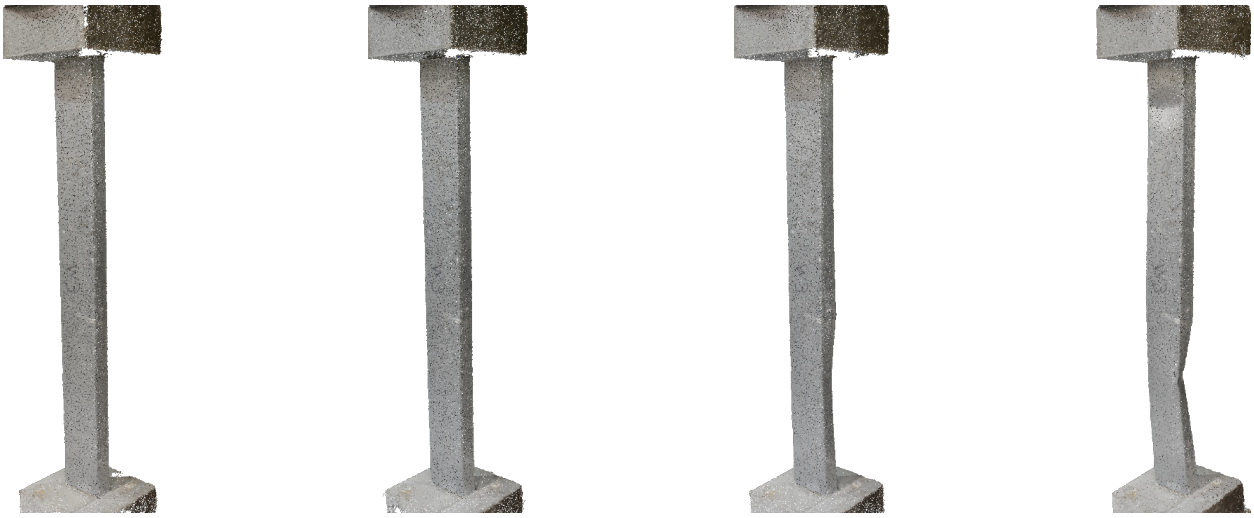

(a) (b) (c) (d)

Figure 6.20: 3d image-based reconstruction point clouds for Specimen 1: (a) 0 kN, (b) 22 kN, (c) 44 kN, (d) 22 kN

6.2.2 Buckling mode participation using 3d point clouds

The cross-sectional dimensions and material properties of each specimen are inputted into Buckling Cracker and generalized beam theory (GBT) mode shapes of Specimen 1 are generated as shown in Figure 6.21 (Specimen 2 mode shapes are similar and not shown).

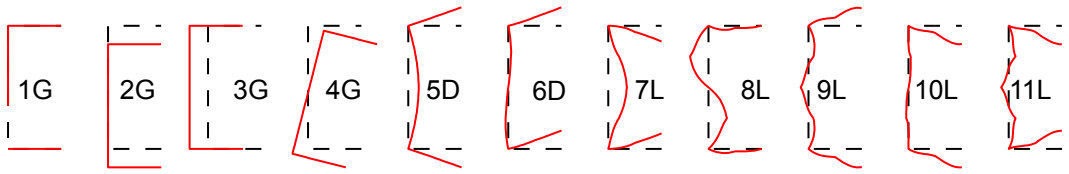

Figure 6.21: GBT mode shapes for Specimen 1, G global, D distortional, L local buckling

The displacement field at 200 cross-sections along each specimen is then used as input for GBT bucking mode identification. Buckling Cracker calculates the modal amplitudes and mode participation factors. Relative participation of the dominant modes along the height of Specimens 1 and 2 are shown in Figure 6.22 and Figure 6.23. The member modal participation factors are recorded in Table 6.3 and Table 6.4. Note that the participation factor at 0 kN (initial imperfections) should be considered separately from the participation factors under load because the factors with load are calculated assuming the initial imperfection as the baseline geometry (i.e., with the initial imperfections removed).

For both Specimen 1 and Specimen 2, distortional and local buckling modes mix in the deformed shape up to peak load which is to be expected for this cross-section. Weak axis flexural buckling dominates after peak load as the flanges and web developed plastic folds and hinges. The modal participation results are consistent with observations during the experiments.

Table 6.3: Specimen 1 –Member modal participations - G global, D distortional, L local buckling

Load (kN)	G	D	L
0 *(imp.)*	*0.24*	*0.34*	*0.42*
22	0.09	0.43	0.48
44	0.25	0.40	0.35
22	0.46	0.30	0.24

Table 6.4: Specimen 2 - Modal participations. G denotes global, D denotes distortional, L denotes local

Load (kN)	G	D	L
0 *(imp.)*	*0.51*	*0.23*	*0.26*
22	0.25	0.36	0.39
44	0.25	0.40	0.36
22	0.37	0.35	0.28

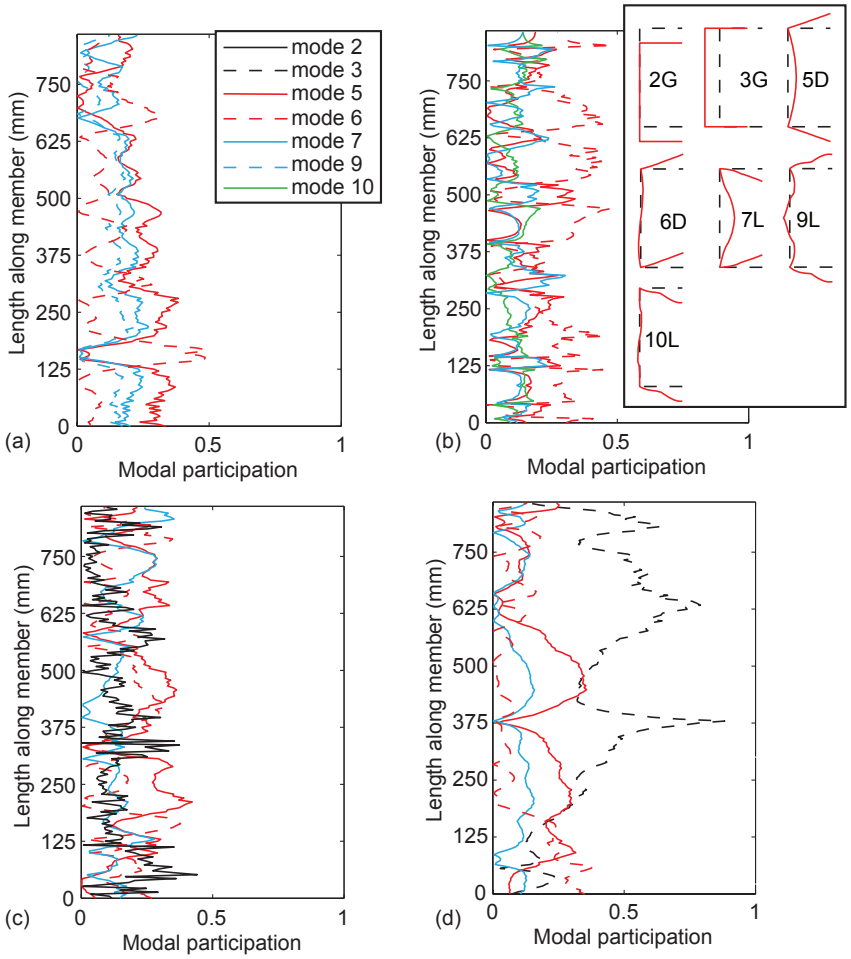

Figure 6.22: Specimen 1–cross-section modal amplitudes at load: (a) 0 kN (initial imp); (b) 22 kN; (c) 44kN;(d) 22 kN

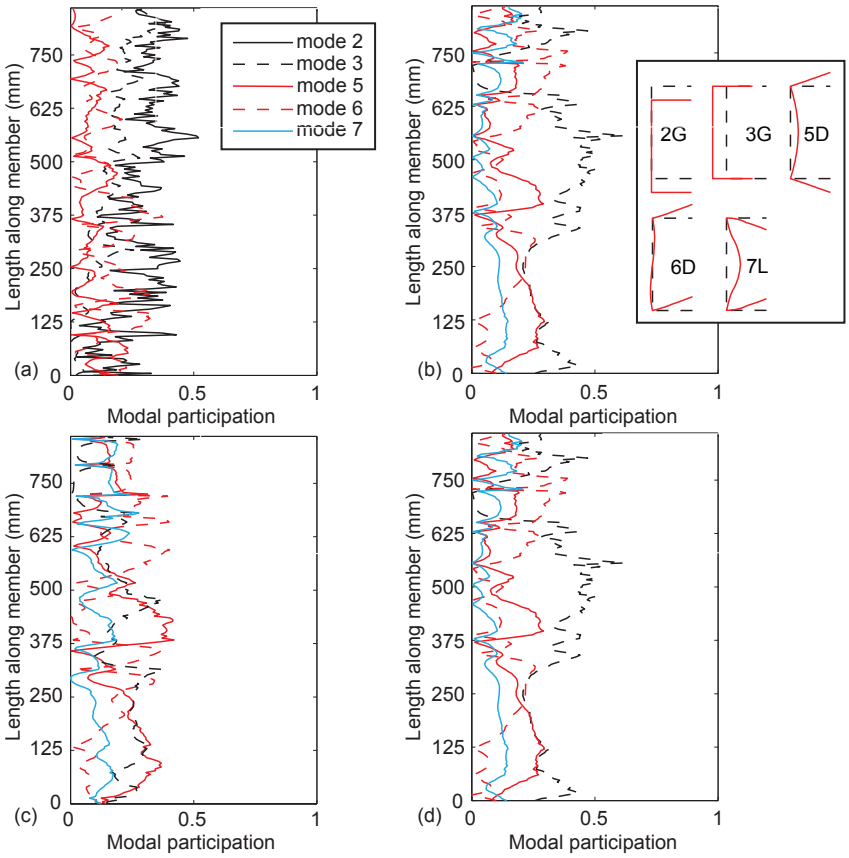

Figure 6.23: Specimen 2–cross-section modal amplitudes at load: (a) 0 kN (initial imp); (b) 22 kN; (c) 44kN;(d) 22 kN

6.3 Summary

This chapter applies buckling mode decomposition to FEA result and experimental points cloud. First, illustrative examples are provided for displacement decomposition of thin-shell finite element eigen-buckling analysis results. The error of displacement reconstruction is under 0.1%. Two examples are provided for stress and energy decomposition and the results are validated against SFEA results. The errors are minimum reading 0.08% and 3.4% (displacement and energy) for Example I and, 0.07% and 3.9% (displacement and energy) for Example II. Lastly, modal decomposition is applied to experimental points cloud. The image reconstructions were used to measure initial geometric imperfections and to track cross-section deformation at column mid-height including distortional buckling and weak axis flexure deformation at peak load. Modal participation throughout the load-deformation response was also characterized.

Chapter 7

Buckling mode decomposition for post-buckling by performing geometrically nonlinear GBT analysis

The current AISI strength prediction method for cold-formed steel members covers local, distortional, global and global-local interactive buckling limit states. For the other interactive buckling limit states, design methods need to be developed. The mechanism of modal interaction should be understood first. Then experiments can be incorporated which eventually lead to a design method. By performing post-buckling analysis using Generalized Beam Theory, the interaction of modes is revealed and their contribution to key quantities, e.g., displacement, can be quantified.

Chapter 7, 8 aim to address geometrically nonlinear GBT formulations and its numerical and analytical solutions. The purpose is to gain deeper understanding of buckling mode coupling in the post-buckling range. Chapter 7 first introduces the geometrically nonlinear GBT formulations, which establish equations with unknown displacement field to be solved by numerical and analytical ways.

7.1 Components of Geometrically Nonlinear Generalized Beam Theory

7.1.1 Kinematics of Thin-Walled Member

The coordinate system of thin-walled member is identical with that of small-displacement formulations of GBT as shown in Figure 3.1 with the global/local coordinates systems being $(X, Y, Z)/(x, s, z)$ and corresponding displacement components $(U, V, W)/(u, v, w)$. Fig-

ure 3.1 is re-shown here as Figure 7.1 for convenience.

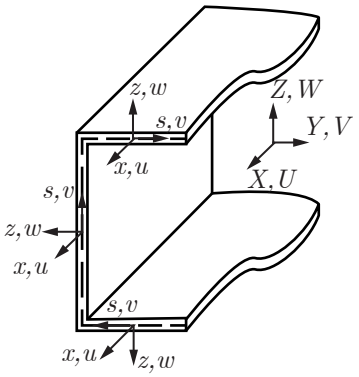

Figure 7.1: Coordinate system and translations for a thin-walled member

Kinematic relations The kinematic relations of geometrically nonlinear GBT formulations take into account the affect of initial imperfection read

$$\varepsilon_{xx} = u_{,x} + \frac{1}{2}(v_{,x}^2 + w_{,x}^2) - zw_{,xx} - \bar{u}_{,x} - \frac{1}{2}(\bar{v}_{,x}^2 + \bar{w}_{,x}^2) + z\bar{w}_{,xx} \tag{7.1.1}$$

$$\varepsilon_{ss} = v_{,x} + \frac{1}{2}(v_{,s}^2 + w_{,s}^2) - zw_{,ss} - \bar{v}_{,x} + \frac{1}{2}(\bar{v}_{,x}^2 + \bar{w}_{,x}^2) + z\bar{w}_{,xx} \tag{7.1.2}$$

$$\gamma_{xs} = u_{,s} + v_{,x} + v_{,x}v_{,s} + w_{,x}w_{,s} - 2zw_{,xs} - \bar{u}_{,s} - \bar{v}_{,x} - \bar{v}_{,x}\bar{v}_{,s} - \bar{w}_{,x}\bar{w}_{,s} + 2z\bar{w}_{,xs} \tag{7.1.3}$$

7.1.2 Constitutive law of Thin-Walled Member

Constitutive law does not change referring to small-displacement GBT formulations:

$$\begin{Bmatrix} \sigma_{xx} \\ \sigma_{ss} \\ \tau_{xs} \end{Bmatrix} = \begin{bmatrix} \frac{E}{1-\nu^2} & \frac{\nu E}{1-\nu^2} & 0 \\ \frac{\nu E}{1-\nu^2} & \frac{E}{1-\nu^2} & 0 \\ 0 & 0 & G \end{bmatrix} \begin{Bmatrix} \varepsilon_{xx} \\ \varepsilon_{ss} \\ \gamma_{xs} \end{Bmatrix}. \tag{7.1.4}$$

7.1.3 Modal representation of the displacement field in geometrically nonlinear Generalized Beam Theory

Geometric nonlinear GBT belongs to total Lagrangian formulations, and the displacement is measured with respect to the non-deformed configuration, more specifically, to the ideal configuration not accounting for the initial imperfection. Accordingly, the displacement field is represented as linearly combination of GBT mode shapes

$$u(s,x) = u_k(s)\phi_{k,x}(x) \qquad v(s,x) = v_k(s)\phi_k(x) \qquad w(s,x) = w_k(s)\phi_k(x), \tag{7.1.5}$$

where $u_k(s), v_k(s), w_k(s)$ are the functions specifying GBT cross-sectional mode shapes; $\phi_k(x)$ is the modal amplitude vector of conventional GBT modes at length x along the member. Along the same line, the initial imperfection is represented as

$$\bar{u}(s,x) = u_k(s)\bar{\phi}_{k,x}(x) \qquad v(s,x) = v_k(s)\bar{\phi}_k(x) \qquad w(s,x) = w_k(s)\bar{\phi}_k(x), \tag{7.1.6}$$

Substitute Eq. (7.1.5) and Eq. (7.1.6) into Eq. (7.1.1)-Eq. (7.1.3), the strain components are

$$\varepsilon_{xx} = u_k\phi_{k,xx}+1/2(v_kv_i+w_kw_i)\phi_{k,x}\phi_{i,x}-zw_k\phi_{k,xx}-u_k\bar{\phi}_{k,xx}-1/2(v_kv_i+w_kw_i)\bar{\phi}_{k,x}\bar{\phi}_{i,x}+zw_k\bar{\phi}_{k,xx}, \tag{7.1.7}$$

$$\varepsilon_{ss} = v_{k,s}\phi_k+1/2(v_{k,s}v_{i,s}+w_{k,s}w_{i,s})\phi_k\phi_i-zw_{k,ss}\phi_k-v_{k,s}\bar{\phi}_k-1/2(v_{k,s}v_{i,s}+w_{k,s}w_{i,s})\bar{\phi}_k\bar{\phi}_i+zw_{k,ss}\bar{\phi}_k, \tag{7.1.8}$$

$$\gamma_{xs} = (u_{k,s}+v_k)\phi_{k,x}+(v_{k,s}v_{i,s}+w_kw_{i,s})\phi_{k,x}\phi_i-2zw_{k,s}\phi_{k,x}-(u_{k,s}+v_k)\bar{\phi}_{k,x}-(v_{k,s}v_{i,s}-w_kw_{i,s})\bar{\phi}_{k,x}\bar{\phi}_i+2zw_{k,s}\bar{\phi}_{k,x} \tag{7.1.9}$$

7.1.4 Establishment of governing equilibrium equations for geometrically nonlinear Generalized Beam Theory

To acquire a differential equation system of equilibrium, the Principle of Virtual Work is utilized, i.e.,

$$\delta V = \delta U+\delta\Pi = 0 \tag{7.1.10}$$

where δV is the variation in total potential energy, δU is the variation in elastic strain energy, and $\delta\Pi$ is the variation of potential energy with respect to the applied external force and traction.

Internal elastic strain energy The strain energy variation is given by

$$\begin{aligned}\delta U &= \int_L \int_B \int_t (\sigma_{xx}\delta\varepsilon_{xx} + \sigma_{ss}\delta\varepsilon_{ss} + \tau_{xs}\delta\gamma_{xs}) \\ &= \delta U_1 + \delta U_2 + \delta U_3 - \delta\bar{U}_1 - \delta\bar{U}_2 - \delta\bar{U}_3, \end{aligned} \tag{7.1.11}$$

where $\delta U_1, \delta U_2, \delta U_3, \delta\bar{U}_1, \delta\bar{U}_2, \delta\bar{U}_3$ are

$$\delta U_1 = \int_L (C_{kh}\phi_{k,xx}\delta\phi_{h,xx} + B_{kh}\phi_k\delta\phi_h + D^I_{kh}\phi_{k,x}\delta\phi_{h,x} + D^{II}_{kh}\phi_k\delta\phi_{h,xx} + D^{II}_{hk}\phi_{k,xx}\delta\phi_h)dx \tag{7.1.12}$$

$$\begin{aligned}\delta U_2 = \int_L &(C_{kjh}\phi_{k,xx}\phi_{j,x}\delta\phi_{h,x} + 1/2C_{hjk}\phi_{k,x}\phi_{j,x}\delta\phi_{h,xx} \\ &+ (B_{kjh} + 1/2B_{hjk})\phi_k\phi_j\delta\phi_h + D^I_{kjh}\phi_{k,x}\phi_{j,x}\delta\phi_h + (D^I_{hkj} + D^I_{khj})\phi_{k,x}\phi_j\delta\phi_{h,x} \\ &+ 1/2D^{II}_{hjk}\phi_k\phi_j\delta\phi_{h,xx} + D^{II}_{kjh}\phi_{k,xx}\phi_j\delta\phi_h + D^{III}_{kjh}\phi_k\phi_{j,x}\delta\phi_{h,x} + 1/2D^{III}_{hjk}\phi_{k,x}\phi_{j,x}\delta\phi_h)dx \end{aligned} \tag{7.1.13}$$

$$\begin{aligned}\delta U_3 = \int_L &(1/2C_{kijh}\phi_{k,x}\phi_{i,x}\phi_{j,x}\delta\phi_{h,x} + 1/2B_{kijh}\phi_k\phi_i\phi_j\delta\phi_h \\ &+ D^I_{kijh}\phi_{k,x}\phi_i\phi_j\delta\phi_{h,x} + D^I_{kihj}\phi_{k,x}\phi_i\phi_{j,x}\delta\phi_h \\ &+ 1/2D^{II}_{kijh}\phi_{k,x}\phi_{i,x}\phi_j\delta\phi_h + 1/2D^{II}_{jhki}\phi_k\phi_i\phi_{j,x}\delta\phi_{h,x})dx \end{aligned} \tag{7.1.14}$$

$$\delta\bar{U}_1 = \int_L (C_{kh}\bar{\phi}_{k,xx}\delta\phi_{h,xx} + B_{kh}\bar{\phi}_k\delta\phi_h + D^I_{kh}\bar{\phi}_{k,x}\delta\phi_{h,x} + D^{II}_{kh}\bar{\phi}_k\delta\phi_{h,xx} + D^{II}_{hk}\bar{\phi}_{k,xx}\delta\phi_h)dx \tag{7.1.15}$$

$$\begin{aligned}\delta\bar{U}_2 = \int_L &(C_{kjh}\bar{\phi}_{k,xx}\phi_{j,x}\delta\phi_{h,x} + 1/2C_{hjk}\bar{\phi}_{k,x}\phi_{j,x}\delta\phi_{h,xx} \\ &+ \bar{B}_{kjh}\bar{\phi}_k\phi_j\delta\phi_h + 1/2B_{hjk}\bar{\phi}_k\bar{\phi}_j\delta\phi_h + D^I_{kjh}\bar{\phi}_{k,x}\phi_{j,x}\delta\phi_h + D^I_{khj}\bar{\phi}_{k,x}\phi_j\delta\phi_{h,x} + D^I_{hkj}\bar{\phi}_{k,x}\bar{\phi}_j\delta\phi_{h,x} \\ &+ D^{II}_{kjh}\bar{\phi}_{k,xx}\phi_j\delta\phi_h + 1/2D^{II}_{hjk}\bar{\phi}_k\bar{\phi}_j\delta\phi_{h,xx} + D^{III}_{kjh}\bar{\phi}_k\phi_{j,x}\delta\phi_{h,x} + 1/2D^{III}_{hjk}\bar{\phi}_{k,x}\bar{\phi}_{j,x}\delta\phi_h)dx \end{aligned} \tag{7.1.16}$$

$$\begin{aligned}\delta U_3 = \int_L (&1/2 C_{kijh}\bar{\phi}_{k,x}\bar{\phi}_{i,x}\phi_{j,x}\delta\phi_{h,x} + 1/2 B_{kijh}\bar{\phi}_k\bar{\phi}_i\phi_j\delta\phi_h \\ &+ D^I_{kijh}\bar{\phi}_{k,x}\bar{\phi}_i\phi_j\delta\phi_{h,x} + D^I_{kihj}\bar{\phi}_{k,x}\phi_i\phi_{j,x}\delta\phi_h \\ &+ 1/2 D^{II}_{kijh}\bar{\phi}_{k,x}\phi_{i,x}\phi_j\delta\phi_h + 1/2 D^{II}_{jhki}\bar{\phi}_k\bar{\phi}_i\phi_{j,x}\delta\phi_{h,x})dx\end{aligned} \tag{7.1.17}$$

where $\delta U_1, \delta U_2, \delta U_3$ are first, second and third order term with respect to the modal amplitude ϕ; $\delta\bar{U}_1, \delta\bar{U}_2, \delta\bar{U}_3$ are first, second and third order term with respect to the product of initial imperfection $\bar{\phi}$ and modal amplitude ϕ. Tensors denoted by C, D and B are calculated using GBT mode shapes, cross-sectional dimensions and material properties:

$$C_{kh} = \int_b \frac{E}{(1-\nu^2)} t u_k u_h ds + \int_b \frac{Et^3}{12(1-\nu^2)} w_k w_h ds, \tag{7.1.18}$$

$$D^I_{kh} = \int_b \frac{Et}{2(1+\nu)}(v_k + u_{k,s})(v_h + u_{h,s}) + \frac{Gt^3}{3} w_{k,s} w_{h,s} ds, \tag{7.1.19}$$

$$D^{II}_{kh} = \int_b \frac{\nu Et}{1-\nu^2} v_{k,s} u_h + \frac{\nu Et^3}{12(1-\nu^2)} w_i w_{k,ss} ds, \tag{7.1.20}$$

$$B_{kh} = \int_b \frac{Et}{1-\nu^2} v_{k,s} v_{h,s} + \frac{t^3}{12(1-\nu^2)} w_{i,ss} w_{k,ss} ds, \tag{7.1.21}$$

$$B_{kjh} = \int_b \frac{Et}{1-\nu^2} v_{k,s} w_{j,s} w_{h,s} ds, \tag{7.1.22}$$

$$D^I_{kjh} = \int_b \frac{Et}{2(1+\nu)}(v_k + u_{k,s}) w_j w_{h,s} ds, \tag{7.1.23}$$

$$D^{II}_{kjh} = \int_b \frac{Eet}{1-\nu^2} u_k w_{j,s} w_{h,s} ds, \tag{7.1.24}$$

$$D^{III}_{kjh} = \int_b \frac{Eet}{1-\nu^2} v_{k,s}(v_j v_h + w_j w_h) ds, \tag{7.1.25}$$

$$C_{kijh} = \int_b \frac{Et}{1-\nu^2}(v_j v_h + w_j w_h)(v_j v_h + w_j w_h) ds, \tag{7.1.26}$$

$$D^I_{kijh} = \int_b \frac{Et}{2(1+\nu)} w_k w_{i,s} w_{j,s} w_h ds, \tag{7.1.27}$$

$$D^{II}_{kijh} = \int_b \frac{Et\nu}{1-\nu^2}(v_k v_i + w_k w_i) w_{j,s} w_{h,s} ds, \tag{7.1.28}$$

$$B_{kijh} = \int_b \frac{Et}{1-\nu^2} w_{k,s} w_{i,s} w_{j,s} w_{h,s} ds, \tag{7.1.29}$$

where subscripts h, i, j, k correspond to the index of GBT mode.

Loading and external potential energy For the virtual work $\delta\Pi_q$ with respect traction q_x, q_s, and q_z along the local coordinate axes x, s, z (Figure 7.2) applied at the center line of the thin-plate. Under the variation of $\delta\phi_h$:

$$\delta\Pi_q = -\int_L \int_b (q_x\delta u + q_s\delta v + q_z\delta w)dsdx = -\int_L q_h\delta\phi_h dx - \int_L q_h^*\delta\phi_{h,x}dx \tag{7.1.30}$$

where q_h is force vector corresponds to mode h:

$$q_h = \int_b (q_s v_h + q_z w_h)ds \qquad q_h^* \qquad = \int_b (q_x u_h)ds \tag{7.1.31}$$

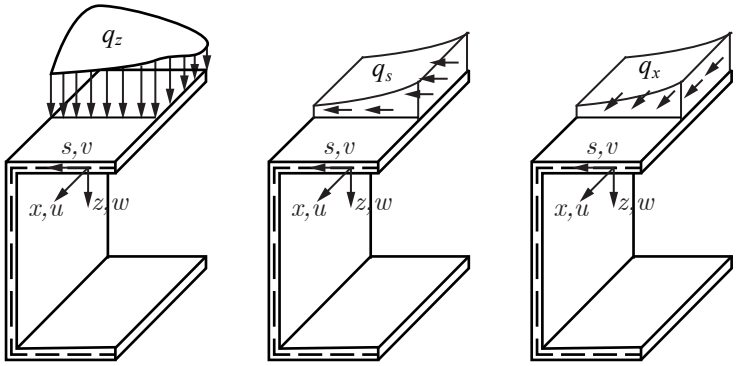

Figure 7.2: Distributed loading

For end applied traction $\sigma(s)$ and $\tau(s)$ applied on the center line at the end cross-section. Under the variation of $\delta\phi_h$:

$$\delta\Pi_W = -\int_b (\sigma(s)u_h\delta\phi_{h,x} + \tau(s)w_h\delta\phi_h)ds \mid_0^L = -W_h^\sigma\delta\phi_{h,x} \mid_0^L - W_h^\tau\delta\phi_h \mid_0^L, \tag{7.1.32}$$

where W_h^σ and W_h^τ mean modal force vectors resulted from normal and shear traction respectively. For example, for mode 2 the flexural mode , W_2^σ is applied moment usually denoted as M, and W_h^τ is applied shear force usually denoted as V.

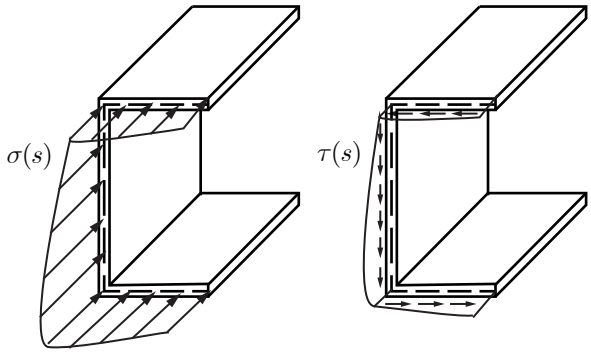

Figure 7.3: End loading

7.1.5 Establishment of governing equilibrium equations for Generalized Beam Theory post-buckling analysis

To acquire a differential equation system of equilibrium, the Principle of Virtual Work is utilized, i.e.,

$$\delta V = \delta U_1 + \delta U_2 + \delta U_3 - \delta \bar{U}_1 - \delta \bar{U}_2 - \delta \bar{U}_3 + \delta \Pi_q + \delta \Pi_W = 0 \tag{7.1.33}$$

where δV is the variation in total potential energy, δU is the variation in elastic strain energy, $\delta \Pi_q$ is the variation in the potential energy with respect to distributed traction, and $\delta \Pi_W$ is the variation of potential energy with respect to the member-end applied traction.

7.2 Finite element formulation for the Generalized Beam Theory post-buckling analysis

Eq. (7.1.33) is a variation formula with modal amplitude vector $\phi(x)$ to solve for. Note the nature of $\phi(x)$ is unknown. In the spirit of using piece-wise approximation and finite-element method to solve for variational problem, $\phi(x)$ is approximated by cubic functions. For modes with out-of-plane deformation v and w, namely conventional modes and extension modes, Hermitian polynomials are used as shape function. For modes with null out-of-plane deformation but merely warping u, namely the uniform compression mode and shear-warping modes, Lagrangian polynomials are used as shape functions:

Uniform compression & shear warping modes:

$$\phi_{k,x} = \psi_{1,x} d_{k.1} + \psi_{2,x} d_{k.2} + \psi_{3,x} d_{k.3} + \psi_{4,x} d_{k.4} + \psi_5 \cdot 0 + \psi_6 \cdot 0 + \psi_7 \cdot 0 + \psi_8 \cdot 0, \tag{7.2.1}$$

Conventional & extension modes:

$$\phi_k = \psi_1 \cdot 0 + \psi_2 \cdot 0 + \psi_3 \cdot 0 + \psi_4 \cdot 0 + \psi_5 d_{k.5} + \psi_6 d_{k.6} + \psi_7 d_{k.7} + \psi_8 d_{k.8}, \tag{7.2.2}$$

where $\psi_{1,x\sim4,x}$ are Hermitian polynomials and $\psi_{5\sim8}$ Lagrangian as shown in Figure 7.4; $d_{k.5\sim8}$ are null for warping only modes and $d_{k.1\sim4}$ for other modes. In the same spirit, the initial imperfection uses the same approximation:

Uniform compression & shear warping modes:

$$\bar{\phi}_{k,x} = \psi_{1,x}\bar{d}_{k.1} + \psi_{2,x}\bar{d}_{k.2} + \psi_{3,x}\bar{d}_{k.3} + \psi_{4,x}\bar{d}_{k.4} + \psi_5 \cdot 0 + \psi_6 \cdot 0 + \psi_7 \cdot 0 + \psi_8 \cdot 0, \tag{7.2.3}$$

Conventional & extension modes:

$$\bar{\phi}_k = \psi_1 \cdot 0 + \psi_2 \cdot 0 + \psi_3 \cdot 0 + \psi_4 \cdot 0 + \bar{\psi}_5 d_{k.5} + \bar{\psi}_6 d_{k.6} + \bar{\psi}_7 d_{k.7} + \bar{\psi}_8 d_{k.8}, \tag{7.2.4}$$

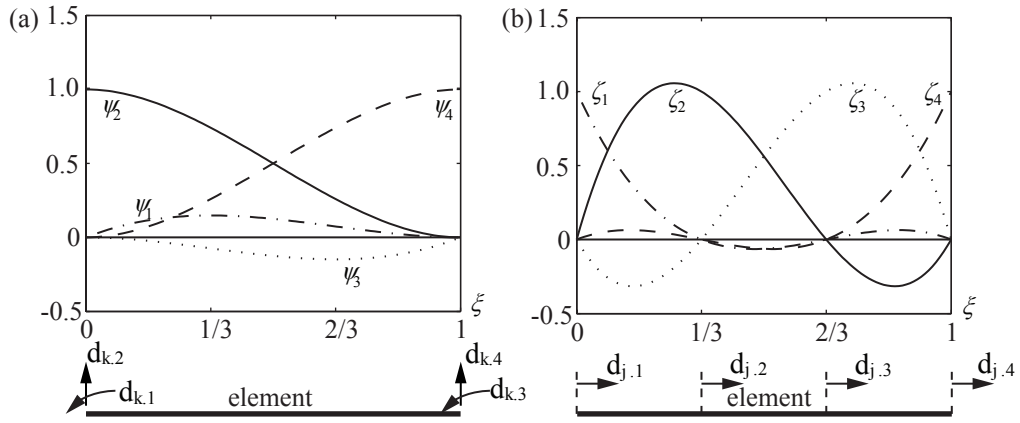

Figure 7.4: Shape functions and FE degrees of freedom of (a) Hermite polynomials, (b) Lagrange polynomials

Plug the shape functions of Eq. (7.2.2) into Eq. (7.1.33) by substituting the variation $\delta\phi$ using variation of finite element degrees of freedom:

$$\delta\phi_h = \psi_\beta \cdot \delta d_{h\beta}. \tag{7.2.5}$$

The equilibrium path is found that internal force equals external force. Internal forces by definition are the derivatives of internal energy with respect to degrees of freedom (generalized displacements):

$$f_{h\beta} = \frac{\partial U}{\partial d_{h\beta}}, \tag{7.2.6}$$

where U stands for internal strain energy as shown in Eq. (7.1.33); $d_{h\beta}$ means the β^{th} degree of freedom of the h^{th} GBT mode; $f_{h\beta}$ means the internal force component associated with $d_{h\beta}$. Organizing the terms of f based on the order of d and $\bar{d}$:

$$f_{h\beta} = f^1_{h\beta} + f^2_{h\beta} + f^3_{h\beta} - \bar{f}^1_{h\beta} - \bar{f}^2_{h\beta} - \bar{f}^3_{h\beta}, \tag{7.2.7}$$

where $f^1_{h\beta}$, $f^2_{h\beta}$, , $f^3_{h\beta}$ correspond to first, second and third order terms involves only d, $\bar{f}^1_{h\beta}$, $\bar{f}^1_{h\beta}$, , $f^3_{h\beta}$ correspond to first, second and third order terms involves both d and initial imperfection $\bar{d}$ (d and $\bar{d}$ are treated as same order),

$$f^1_{h\beta} = (C_{kh}k^1_{\alpha\beta} + D^I_{kh}k^2_{\alpha\beta} + D^{II}_{kh}k^3_{\alpha\beta} + D^{II}_{hk}k^3_{\alpha\beta} + B_{kh}k^4_{\alpha\beta})d_{k\alpha}, \tag{7.2.8}$$

$$\begin{aligned} f^2_{h\beta} = {} & (C_{kjh}k^1_{\alpha\eta\beta} + \frac{1}{2}C_{hjk}k^1_{\beta\eta\alpha} + (B_{kjh} + \frac{1}{2}B_{hjk})k^2_{\alpha\eta\beta} + D^I_{kjh}k^3_{\alpha\eta\beta} + (D^I_{hkj} + D^I_{khj})k^3_{\alpha\eta\beta} + \frac{1}{2}D^{II}_{hjk}k^4_{\alpha\eta\beta} \\ & + D^{II}_{kjh}k^4_{\beta\eta\alpha} + D^{III}_{kjh}k^3_{\beta\eta\alpha} + \frac{1}{2}D^{III}_{hjk}k^3_{\alpha\eta\beta})d_{k\alpha}d_{j\eta}, \end{aligned} \tag{7.2.9}$$

$$\begin{aligned} f^3_{h\beta} = {} & (\frac{1}{2}C_{kijh}k^1_{\alpha\chi\eta\beta} + \frac{1}{2}B_{kijh}k^2_{\alpha\chi\eta\beta} + D^I_{kijh}k^3_{\alpha\chi\eta\beta} + D^I_{kihj}k^3_{\alpha\chi\beta\eta} + \frac{1}{2}D^{II}_{kijh}k^3_{\alpha\beta\eta\chi} \\ & + \frac{1}{2}D^{II}_{jhki}k^3_{\eta\chi\alpha\beta})d_{k\alpha}d_{i\chi}d_{j\eta}, \end{aligned} \tag{7.2.10}$$

$$\bar{f}^1_{h\beta} = (C_{kh}k^1_{\alpha\beta} + D^I_{kh}k^2_{\alpha\beta} + D^{II}_{kh}k^3_{\alpha\beta} + D^{II}_{hk}k^3_{\alpha\beta} + B_{kh}k^4_{\alpha\beta})\bar{d}_{k\alpha}, \tag{7.2.11}$$

$$\begin{aligned} \bar{f}^2_{h\beta} = {} & (C_{kjh}k^1_{\alpha\eta\beta} + B_{kjh}k^2_{\alpha\eta\beta} + D^I_{kjh}k^3_{\alpha\eta\beta} + D^I_{khj}k^3_{\alpha\beta\eta} + D^{II}_{kjh}k^4_{\beta\eta\alpha} + D^{III}_{kjh}k^3_{\beta\eta\alpha})\bar{d}_{k\alpha}d_{j\eta} \\ & + \frac{1}{2}(C_{hjk}k^1_{\beta\eta\alpha} + B_{hjk}k^2_{\alpha\eta\beta} + 2D^I_{hkj}k^3_{\alpha\beta\eta} + D^{II}_{hjk}k^4_{\alpha\eta\beta} + D^{III}_{hjk}k^3_{\alpha\eta\beta})\bar{d}_{k\alpha}\bar{d}_{j\eta}, \end{aligned} \tag{7.2.12}$$

$$\begin{aligned} \bar{f}^3_{h\beta} = {} & (\frac{1}{2}C_{kijh}k^1_{\alpha\chi\eta\beta} + \frac{1}{2}B_{kijh}k^2_{\alpha\chi\eta\beta} + D^I_{kijh}k^3_{\alpha\chi\eta\beta} + D^I_{kihj}k^3_{\alpha\chi\beta\eta} + \frac{1}{2}D^{II}_{kijh}k^3_{\alpha\beta\eta\chi} \\ & + \frac{1}{2}D^{II}_{jhki}k^3_{\eta\chi\alpha\beta})\bar{d}_{k\alpha}\bar{d}_{i\chi}d_{j\eta}. \end{aligned} \tag{7.2.13}$$

where matrices $k_{(\cdot)}$ are terms gathering the integration of shape functions over the finite element length:

$$k^1_{\alpha\beta} = \int_{L_e} \psi_{\alpha,xx}\psi_{\beta,xx}dx, \tag{7.2.14}$$

$$k^2_{\alpha\beta} = \int_{L_e} \psi_{\alpha,x}\psi_{\beta,x}dx, \tag{7.2.15}$$

$$k^3_{\alpha\beta} = \int_{L_e} \psi_{\alpha}\psi_{\beta,xx}dx, \tag{7.2.16}$$

$$k^4_{\alpha\beta} = \int_{L_e} \psi_{\alpha}\psi_{\beta}dx, \tag{7.2.17}$$

$$k^1_{\alpha\eta\beta} = \int_{L_e} \psi_{\alpha,xx}\psi_{\eta,x}\psi_{\beta,x}dx, \tag{7.2.18}$$

$$k^2_{\alpha\eta\beta} = \int_{L_e} \psi_{\alpha}\psi_{\eta}\psi_{\beta}dx, \tag{7.2.19}$$

$$k^3_{\alpha\eta\beta} = \int_{L_e} \psi_{\alpha,x}\psi_{\eta,x}\psi_{\beta}dx, \tag{7.2.20}$$

$$k^4_{\alpha\eta\beta} = \int_{L_e} \psi_{\alpha}\psi_{\eta}\psi_{\beta,xx}dx, \tag{7.2.21}$$

$$k^1_{\alpha\chi\eta\beta} = \int_{L_e} \psi_{\alpha,x}\psi_{\chi,x}\psi_{\eta,x}\psi_{\beta,x}dx, \tag{7.2.22}$$

$$k^2_{\alpha\chi\eta\beta} = \int_{L_e} \psi_{\alpha}\psi_{\chi}\psi_{\eta}\psi_{\beta}dx, \tag{7.2.23}$$

$$k^3_{\alpha\chi\eta\beta} = \int_{L_e} \psi_{\alpha,x}\psi_{\chi}\psi_{\eta}\psi_{\beta,x}dx. \tag{7.2.24}$$

In Eq. (7.2.14) to Eq. (7.2.24), $\psi_{(\cdot)}$ means the shape function for the modal amplitude. It should be noted for warping only modes, the first derivative is approximated by Lagrangian polynomials, and thus, $\psi_{1,x} \sim \psi_{4,x}$ refers to Lagrangian polynomials as shown in Eq. (7.2.2). If this is not noticed error will arise in the followed computer programming. The force vector associated with degrees of freedom can be found by taking derivative with d of the force potential energy in Eq. (7.1.30) and Eq. (7.1.32),

$$f^E_{h\beta} = \frac{\partial(\Pi_q + \Pi_W)}{\partial d_{h\beta}}. \tag{7.2.25}$$

Along the same line of getting the internal force vector, plug the finite element approximation of ϕ into expressions of Π_q, Π_W and start taking derivative with respect to $d_{h\beta}$,

$$f^E_{h\beta} = q_h \int_{L_e} \psi_\beta dx + q^*_h \int_{L_e} \psi_{\beta,x} dx + W^\sigma_h \psi_{\beta,x} \mid^{L_e}_0 + W^\tau_h \psi_\beta \mid^{L_e}_0, \tag{7.2.26}$$

where q_h, q^*_h are force component derived from traction applied that keeps unchanged along the finite element length as shown in Eq. (7.1.31) and Figure 7.2; W^σ_h and W^τ_h are force component derived from traction applied at a cross-section, like shown in Eq. (7.1.32) and .

In many path following techniques for solving the equilibrium equation, the stiffness matrix, or Jacobian of the internal force vector, is used. They can be found by taking derivative of internal force vector with respect to generalized displacement vector that defines the displacement field,

$$\begin{aligned} T_{hp\beta u} &= \frac{\partial f_{h\beta}}{\partial d_{pu}} \\ &= \frac{\partial f^1_{h\beta}}{\partial d_{pu}} + \frac{\partial f^2_{h\beta}}{\partial d_{pu}} + \frac{\partial f^3_{h\beta}}{\partial d_{pu}} - \frac{\partial \bar{f}^1_{h\beta}}{\partial d_{pu}} - \frac{\partial \bar{f}^2_{h\beta}}{\partial d_{pu}} + \frac{\partial \bar{f}^3_{h\beta}}{\partial d_{pu}} \\ &= T^1_{hp\beta u} + T^2_{hp\beta u} + T^3_{hp\beta u} - \bar{T}^1_{hp\beta u} - \bar{T}^2_{hp\beta u} - \bar{T}^3_{hp\beta u}, \end{aligned} \tag{7.2.27}$$

where

$$T^1_{hp\beta u} = C_{kh} k^1_{u\beta} + D^I_{ph} k^2_{u\beta} + D^{II}_{ph} k^3_{u\beta} + D^{II}_{hp} k^3_{\beta u} + B_{ph} k_{u\beta}, \tag{7.2.28}$$

$$\begin{aligned} T^2_{hp\beta u} = (&C_{pkh} k^1_{u\alpha\beta} + C_{kph} k^1_{\alpha u\beta} + C_{hkp} k^1_{\beta\alpha u} + 3B_{hkp} k^2_{u\beta\alpha} + D^I_{pkh} k^3_{u\alpha\beta} + D^I_{kph} k^3_{\alpha u\beta} \\ &+ (D^I_{hpk} + D^I_{phk}) k^3_{u\beta\alpha} + (D^I_{hkp} + D^I_{hkp}) k^3_{\alpha\beta u} + D^{II}_{pkh} k^4_{\beta\alpha u} + D^{II}_{kph} k^4_{\beta u\alpha} + D^{II}_{hkp} k^4_{u\alpha\beta} \\ &+ D^{III}_{pkh} k^3_{\beta\alpha u} + D^{III}_{pkh} k^3_{\beta u\alpha} + D^{III}_{hkp} k^3_{u\alpha\beta}) d_{k\alpha}, \end{aligned} \tag{7.2.29}$$

$$\begin{aligned} T^3_{hp\beta u} = (&C_{kpjh} k^1_{\alpha u\eta\beta} + \frac{1}{2} C_{kjph} k^1_{\alpha\eta u\beta} + \frac{3}{2} B_{kpjh} k^3_{\alpha u\eta\beta} + \frac{1}{2} D^I_{pkjh} k^3_{u\alpha\eta\beta} + D^I_{kpjh} k^3_{\alpha u\eta\beta} \\ &+ D^I_{kjhp} k^3_{\alpha\eta\beta u} + D^I_{pkhj} k^3_{\alpha u\beta\eta} + D^I_{kpjh} k^3_{\alpha u\beta\eta} + D^{II}_{kpjh} k^3_{\alpha\beta\eta u} + \frac{1}{2} D^{II}_{kpjh} k^3_{\alpha\beta\eta u} \\ &+ D^{II}_{jhpk} k^3_{\eta\alpha u\beta} + \frac{1}{2} D^{II}_{phkj} k^3_{\alpha\beta\eta u}) d_{k\alpha} d_{j\eta} \end{aligned} \tag{7.2.31}$$

$$\bar{T}^1_{hp\beta u} = 0, \tag{7.2.33}$$

$$\bar{T}^2_{hp\beta u} = (C_{kph}k^1_{\alpha u\beta} + B_{kph}k^2_{\alpha u\beta} + D^I_{kph}k^3_{\alpha u\beta} + D^I_{khp}k^3_{\alpha\beta u} + D^{II}_{kph}k^4_{\beta u\alpha} + D^{III}_{kph}k^3_{\beta u\alpha})\bar{d}_{k\alpha} \tag{7.2.34}$$

$$\begin{aligned}\bar{T}^3_{hp\beta u} = (&\frac{1}{2}C_{kjph}k^1_{\alpha\eta u\beta} + \frac{1}{2}B_{kjph}k^2_{\alpha\eta u\beta} + D^I_{kjph}k^3_{\alpha\eta u\beta} + D^I_{kjhp}k^3_{\alpha\eta\beta u} + \frac{1}{2}D^{II}_{kjph}k^3_{\alpha\beta u\eta} \\ &+ \frac{1}{2}D^{II}_{phkj}k^3_{u\eta\alpha\beta})\bar{d}_{k\alpha}\bar{d}_{j\eta}.\end{aligned} \tag{7.2.35}$$

7.3 Computer program implementation of nonlinear GBT formulation

A computer program based on geometrically nonlinear GBT formulations is implemented in MATLAB. The code accepts arbitrary loading and open cross-section for a geometrically nonlinear analysis based on GBT. The calculation of internal force and stiffness vector is introduced in the previous sections of this chapter. The equilibrium-path following scheme is introduced next.

It is known thin-walled structures have 'snap-through' problem in numerical simulation, as shown in Figure 7.5(a)(b). The true equilibrium path cannot be followed by simple force-control or displacement-control scheme, but can be found by using advanced path-following technique like arc-length method [106]. In order to simplify the code, a path-following technique is used herein where a chosen displacement component increases a fixed amount for every step, as shown in Figure 7.5(c). It should be advised the method does not intend to solve for structural behavior in Figure 7.5(d), where displacement and load both decreases traveling along the equilibrium path.

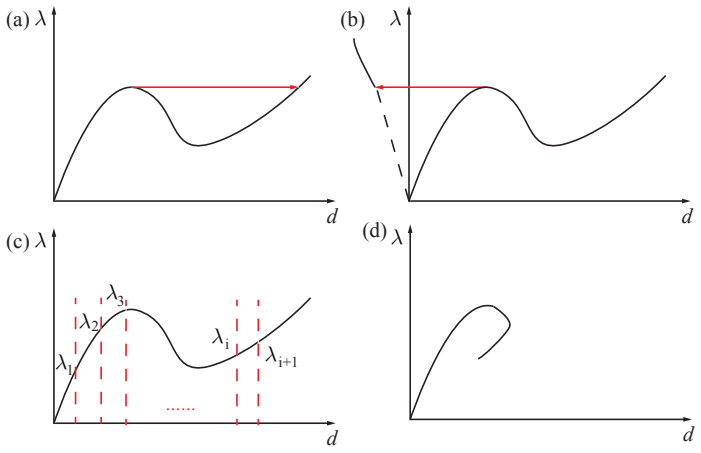

Figure 7.5: Possible equilibrium paths: (a) & (b) 'snap-through'; (c) load-following scheme where chosen displacement has constant increment; (d) a behavior that cannot be solved using current path following scheme.

The incremental equilibrium equation is set:

$$r(\delta d, \delta\lambda) = \begin{bmatrix} \delta f^{int}(d_0 + \delta d) \\ \delta U(d_0 + \delta d) \end{bmatrix} - \begin{bmatrix} \delta\lambda q \\ \delta u \end{bmatrix} = 0, \tag{7.3.1}$$

where $r(d)$ stands for the residual of unbalanced generalized force vector, which is a function of generalized displacements d; δf^{int} means the internal force vector increment; $\delta\lambda$ means the the load parameter increment; q means the load pattern; $U(d)$ stands for a function relates the generalized displacement d with a specific physical displacement u, which is believed to be always increasing, with δu denotes its increment in each step.

The unknowns in the set problem are the generalized displacement vector d and load parameter $\delta\lambda$. To use gradient based technique to find the solution, Jacobian (generalized stiffness matrix) has to be found:

$$J = \begin{bmatrix} \frac{\partial r}{\partial d} \\ \frac{\partial r}{\partial \lambda} \end{bmatrix} = \begin{bmatrix} T & q \\ \partial U/\partial d & \mathbf{0} \end{bmatrix}, \tag{7.3.2}$$

where T stands for the regular stiffness matrix as shown in Eq. (7.2.14) to Eq. (7.2.24), 0 stands for a null matrix. Once the equilibrium equation and Jacobian are both known, the problem can be solved step by step, assuming convergence always achieves. In the author's code, modified Newton-Raphson method is used where the initial stiffness of each incremental-step is used, to save the computational time. In addition, the followed convergence criteria is used,

$$\|r\|_2 \leqq 0.001. \tag{7.3.3}$$

One last comment is that the path-following technique used herein is different than the commonly used 'displacement control' scheme - there is no force applied to the displacement component, u, that is controlled. The main reason of using the path-following scheme is to avoid 'snap-through' associated with low stiffness from structural instability as shown in Figure 7.5(a)(b).

7.4 Examples

The major advantage of GBT post-buckling analysis over shell finite element method, besides the scale of the problem being smaller which might lead to faster computation, is that the contribution of different buckling modes on the key quantities can be revealed. This merit can lead to a better understanding of how different buckling modes interact and lead to structural failure. The power of GBT for decomposing the post-buckling load-deformation response is revealed by two examples. Both the examples involves a C cross-section with the geometry and GBT mode shapes shown in Figure 7.6. The web and flanges are discretized into 6 equal pieces for GBT cross-sectional analysis, and lips into two pieces. The buckling modes included in the analysis are mode 1, 3, 5, 7, 9, 11, 25, 27, 29, 48, 50 as advised by literature [107].

The first example is a 150 mm pinned-pinned column dominated by local buckling. The member length is divided into six GBT elements for the analysis. The initial imperfection is set as 0.1 times thickness of plate. The load-deformation response is calculated by GBT and shell finite element software ABAQUS and compared in Figure 7.6. It can be seen: (1) the load-deformation response yielded by GBT matches SFEA result; (2) the column experiences local buckling has post-buckling strength reserve and the load-deformation response is post-buckling stable as there is no significant stiffness loss after the eigen buckling load of 54 kN; (3) Change of geometry effect is significant in that the warping stress at the edge of mid-height is 255.4 MPa versus 48.2 MPa at maximum out-of-plane deformation location, at merely 3 mm of out-of-plane displacement, as shown in Figure 7.8 that read from SFEA. This demonstrates the well known concept of 'effective-width' [124] for load buckling.

The benefit of using GBT is that the modal contribution to the displacement field can be revealed (the author is working on modal decomposition of stress component for post-buckling range), as shown in Figure 7.9. Note that modal superposition still applies for displacement field like demonstrated by Eq. (7.1.5).

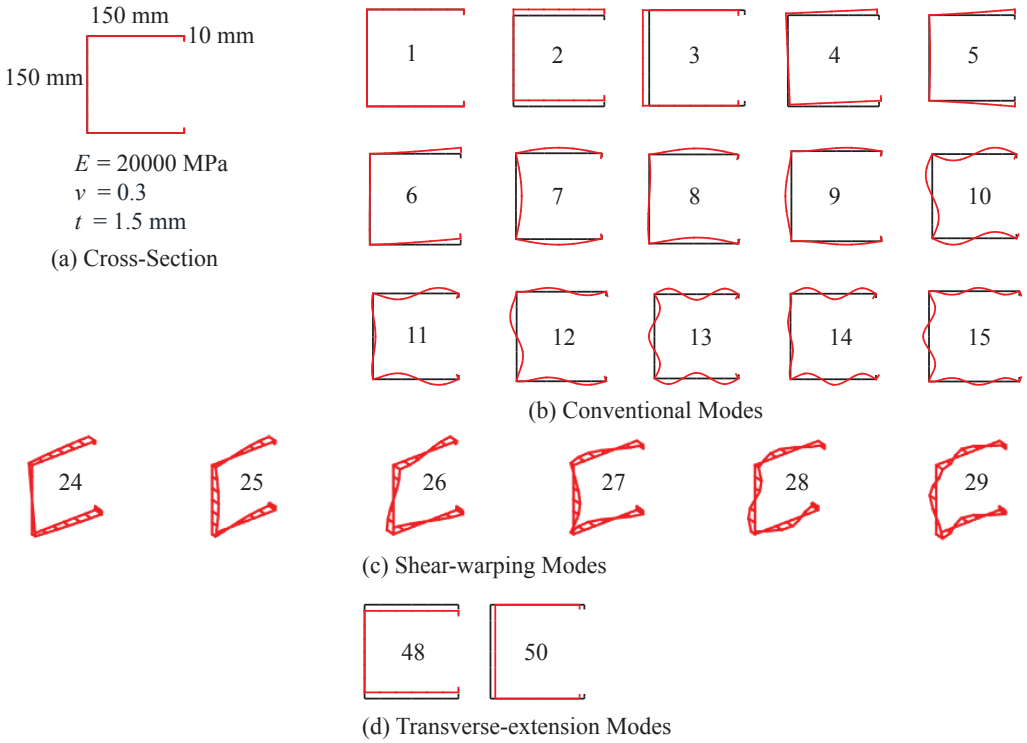

Figure 7.6: Cross-section for the post-buckling analysis: (a) cross-section geometry and material properties; (b) conventional modes; (c) shear-warping modes; (d) transverse-extension modes.

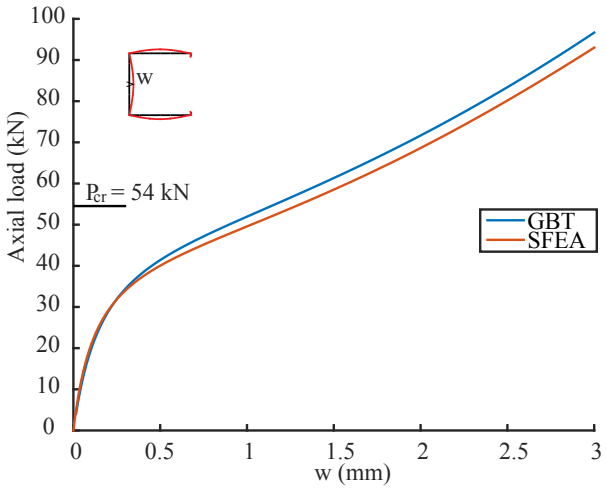

Figure 7.7: Load-deformation response for member experiencing local buckling.

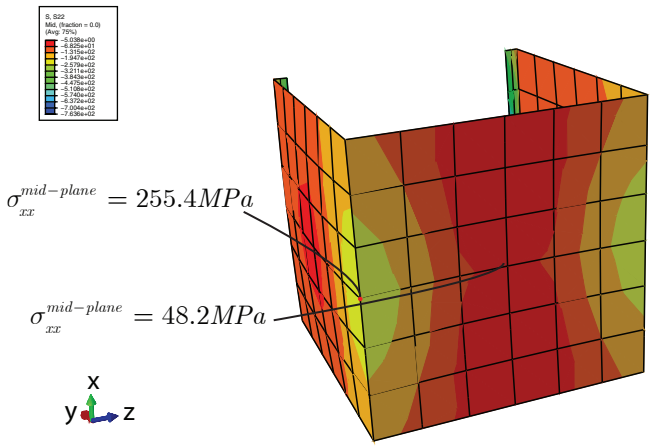

Figure 7.8: Plate mid-plane warping stress distribution for 3mm out-of-plane deformation: change of geometry effect is significant the warping stress at the edge of mid-height is 255.4 MPa vs. 48.2 MPa at maximum out-of-plane deformation location.

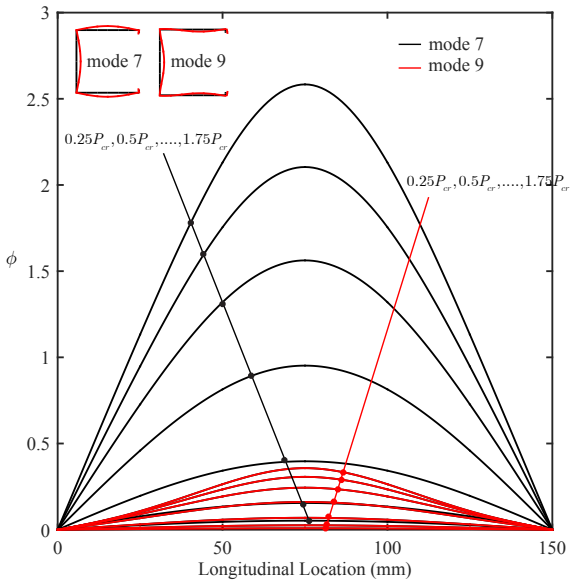

Figure 7.9: Modal amplitude development during the load-deformation response for local buckling.

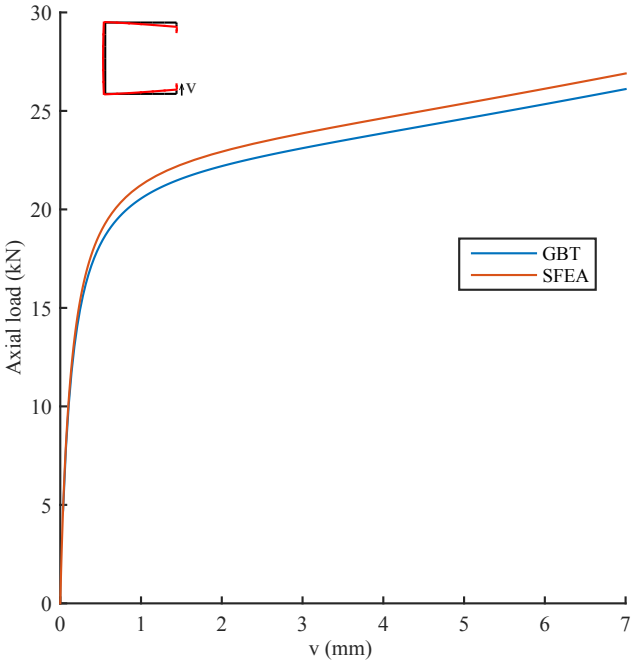

Figure 7.10: Load-deformation response for member experiencing distortional buckling.

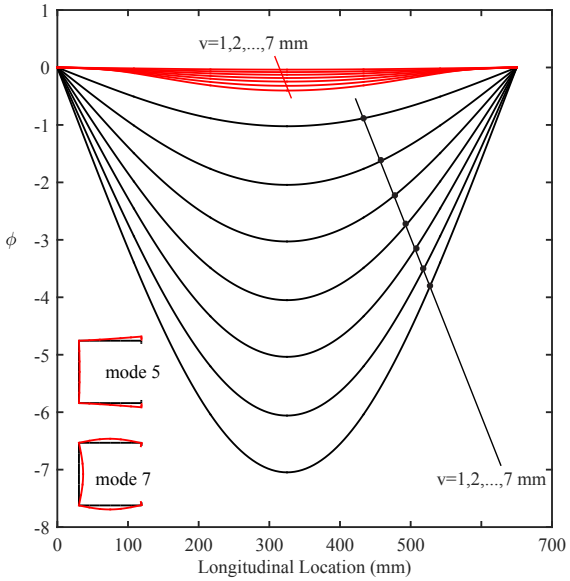

Figure 7.11: Modal amplitude development during the load-deformation response for distortional buckling.

The second example is a member with the same cross-section but the member length is 650 mm. The member is pinned-pinned and discretized into 6 GBT elements. The initial imperfection magnitude is also set as 0.1t. The load-deformation response is solved by GBT code, which agrees with that generated by ABAQUS as shown in Figure 7.10. It can be seen the member quickly losses stiffness after the eigen-buckling load of 22kN, in contrast with the previous example of local buckling. The distortional buckling is accompanied by a small portion of local buckling as well as shown in Figure 7.11.

7.5 Summary

Buckling mode decomposition of post-buckling is facilitated by performing geometrically non-linear GBT analysis. Potential energy is expressed by using third-order displacement-strain relationship. Finite element formulation is then developed using polynomial shape functions for GBT modal amplitude. A computer program is coded in Matlab with incremental-iterative scheme following the load-deformation curve. By using one local-bucking and one distortional-buckling example, it is shown the modal participation can be obtained for any load-step. The outcome can help understanding buckling mode interaction in the post-buckling range.

Chapter 8

GBT analytical solution for column post-buckling response

8.1 Analytical solution for the load-deformation response of a single GBT mode

The assumptions/simplification are:

(1) There is one conventional GBT mode relevant for the load-deformation response;

(2) The magnitude of that mode is sinusoidal: $\phi_k = a \cdot sin(\pi x/L)$.

(3) The magnitude of uniform compression is linear: $\phi_{1,x} = -e \cdot x$, as was assumed by Bazant for plate post-buckling [17].

It is stipulated that the closer these assumptions are to a real case, the better the analytical solution matches the exact solution.

8.1.1 Analytical solution for eigen-buckling

The analytical solution for eigen buckling where there is merely one mode is reported by the inventor of the theory [91]. Under uniform compression, the differential equation writes,

$$C_{kk}\phi_{k,xxxx} - D_{kk}\phi_{k,xx} + B_{kk}\phi_k + \lambda_b C_{1kk}\phi_{k,xx} = 0, \tag{8.1.1}$$

in which λ_b is the buckling load parameter. Plug in $\phi_k = sin(n\pi x/L)$ and solve for λ,

$$\lambda_b = \frac{1}{C_{1kk}} \left[C_{kk}(\frac{n\pi}{L})^2 + D_{kk} + B_{kk}(\frac{L}{n\pi})^2 \right]. \tag{8.1.2}$$

The critical length corresponds to the lowest buckling load parameter. Thus one takes derivative of λ_b with respect to L to find the minimum,

$$d\lambda_b/d_L = 0, \tag{8.1.3}$$

which yields,

$$L_c = n\pi \sqrt[4]{\frac{C_{kk}}{B_{kk}}}, \tag{8.1.4}$$

where L_c stands for critical buckling half-wave length. Substitute it back into Eq. (8.1.2), one has the critical buckling load parameter,

$$\lambda_c = \frac{2\sqrt{C_{kk}B_{kk}} + D_{kk}}{C_{1kk}}. \tag{8.1.5}$$

8.1.2 Analytical solution for post-buckling

Modal amplitude field

The functions of modal amplitude vector, and initial imperfection modal amplitude are known according to the assumptions,

$$\phi(x) = \left\{ \begin{array}{c} \phi_1(x) \\ \phi_k(x) \end{array} \right\} = \left\{ \begin{array}{c} -\frac{1}{2} \cdot e \cdot x^2 \\ a \cdot sin(\pi x/L) \end{array} \right\}, \tag{8.1.6}$$

$$\bar{\phi}(x) = \left\{ \begin{array}{c} \bar{\phi}_1(x) \\ \bar{\phi}_k(x) \end{array} \right\} = \left\{ \begin{array}{c} 0 \\ \bar{a} \cdot sin(\pi x/L) \end{array} \right\}, \tag{8.1.7}$$

where a stands for unknown parameter to solve for; $\bar{\phi}(x)$ stands for the modal amplitude of initial imperfection; $\bar{a}$ stands for the magnitude of initial imperfection.

Solving for the equilibrium equation by energy method

Recall the GBT equilibrium equation,

$$\delta V = \delta U_1 + \delta U_2 + \delta U_3 - \delta \bar{U}_1 - \delta \bar{U}_2 - \delta \bar{U}_3 = 0. \tag{8.1.8}$$

Plug Eq. (8.1.6) and Eq. (8.1.7) into Eq. (8.1.8),

$$\delta V = \frac{\partial V}{\partial a} = Ta^3 + Sa^2 + Fa + Z = 0, \tag{8.1.9}$$

where

$$\begin{aligned}
T &= L^2 \cdot (4 \cdot D^I_{kkkk} \cdot \pi^2 + 2 \cdot D^{II}_{kkkk} \cdot \pi^2))/16 + (3 \cdot C_{kkkk} \cdot \pi^4)/16)/L^3 \\
&\quad + (3 \cdot B_{kkkk} \cdot L)/16, \\
S &= ((2 \cdot D^I_{kkk} \cdot \pi^2 - 2 \cdot D^{II}_{kkk} \cdot \pi^2) \cdot L^2 - C_{kkk} \cdot \pi^4)/(L^3 \cdot \pi) \\
&\quad + (2 \cdot B_{kkk} \cdot L)/\pi - (\pi \cdot D^{III}_{kkk})/(3 \cdot L), \\
F &= ((L^2 \cdot (D^I_{kk} \cdot \pi^2 - 2 \cdot D^{II}_{kk} \cdot \pi^2))/2 + (C_{kk} \cdot \pi^4)/2)/L^3 \\
&\quad - ((D^I_{kkkk} \cdot \pi^2 \cdot L^2 \cdot a_0^2)/4 + (3 \cdot C_{kkkk} \cdot \pi^4 \cdot a_0^2)/16)/L^3 \\
&\quad + (B_{kk} \cdot L)/2 - (((4 \cdot D^I_{kkk} \cdot \pi^2 \cdot a_0)/3 - (4 \cdot D^{II}_{kkk} \cdot \pi^2 \cdot a_0)/3 \\
&\quad + (2 \cdot D^{III}_{kkk} \cdot \pi^2 \cdot a_0)/3) \cdot L^2 - (2 \cdot C_{kkk} \cdot \pi^4 \cdot a_0)/3)/(L^3 \cdot \pi) \\
&\quad + ((2 \cdot D^{III}_{kkk} \cdot \pi^2 \cdot a_0)/3 - (5 \cdot C_{1kk} \cdot \pi^3 \cdot e)/8)/(L \cdot \pi) \\
&\quad - (3 \cdot B_{kkkk} \cdot L \cdot a_0^2)/16 - (4 \cdot B_{kkk} \cdot L \cdot a_0)/(3 \cdot \pi), \\
Z &= (\pi \cdot D^{III}_{kkk} \cdot a_0^2)/(3 \cdot L) - (a_0 \cdot (B_{kk} \cdot L^4 + C_{kk} \cdot \pi^4 + D^I_{kk} \cdot L^2 \cdot \pi^2 - 2 \cdot D^{II}_{kk} \cdot L^2 \cdot \pi^2))/(2 \cdot L^3) \\
&\quad - (2 \cdot B_{kkk} \cdot L \cdot a_0^2)/(3 \cdot \pi) - (((2 \cdot D^I_{kkk} \cdot \pi^2 \cdot a_0^2)/3 - (2 \cdot D^{II}_{kkk} \cdot \pi^2 \cdot a_0^2)/3) \cdot L^2 \\
&\quad - (C_{kkk} \cdot \pi^4 \cdot a_0^2)/3)/(L^3 \cdot \pi) - (D^{II}_{kkkk} \cdot \pi^2 \cdot a_0^3)/(16 \cdot L),
\end{aligned} \tag{8.1.10}$$

in which T, S, F, Z are third order, second order, first order and zeroth order coefficients for the governing equation Eq. (8.1.9); $C's$, $B's$ and $D's$ are GBT matrices as shown in Eq. (7.1.18)˜Eq. (7.1.29). They can be thought as additional cross-sectional properties because their values depend merely on the cross-section geometry and material properties. For every value of N, and corresponding ends shortening e, the displacement magnitude a can be solved by finding the roots of Eq. (8.1.9), which is a cubic algebra equation and has analytical solution. In the followed calculation, Matlab function 'roots' is used to solve for Eq. (8.1.9).

Finding the axial force considering geometric nonlinearity

Axial force, N, is retrieved at the member mid-height,

$$\begin{aligned} N &= \int_b \frac{E}{1-\nu^2}\varepsilon_{xx} + \frac{\nu E}{1-\nu^2}\varepsilon_{ss} tds \\ &= \int_b \frac{E}{1-\nu^2}\varepsilon_{xx} tds + 0 \end{aligned}, \tag{8.1.11}$$

where ε_{ss} is null because of Vlasov's non transverse extension assumption; N means axial force. Now consider the kinematics and strain in Eq. (7.1.7),

$$\begin{aligned} N &= \int_b \frac{E}{1-\nu^2}\varepsilon_{xx} tds \\ &= \frac{EA}{1-\nu^2}\phi_{1,xx} + \int_b \frac{E}{1-\nu^2}(u_k\phi_{k,xx} + 1/2(v_k v_i + w_k w_i)\phi_{k,x}\phi_{i,x} \\ &- u_k\bar{\phi}_{k,xx} - 1/2(v_k v_i + w_k w_i)\bar{\phi}_{k,x}\bar{\phi}_{i,x})ds \\ &= \frac{EA}{1-\nu^2}\phi_{1,xx} + \int_b \frac{E}{1-\nu^2}\cdot u_k \cdot (\phi_{k,xx} - \bar{\phi}_{k,xx})\cdot tds \\ &+ \int_b \frac{E}{1-\nu^2}\cdot 1/2(v_k v_k + w_k w_k)\cdot(\phi_{k,x}\phi_{k,x} - \bar{\phi}_{k,x}\bar{\phi}_{k,x}))tds. \end{aligned} \tag{8.1.12}$$

Notice that $\int_b \frac{E}{1-\nu^2}\cdot u_k \cdot tds = 0$ because of the GBT orthogonal condition; $\int_b \frac{E}{1-\nu^2}\cdot(v_k v_k + w_k w_k)tds = C_{1kk}$; and $\phi_k = a\cdot sin(\pi x/L)$, $\bar{\phi}_k = \bar{a}\cdot sin(\pi x/L)$,

$$N = \frac{EA}{1-\nu^2}\phi_{1,xx} + \frac{1}{2}\cdot(a^2 - \bar{a}^2)\cdot(\frac{\pi}{L})^2\cdot C_{1kk}\cdot\cos^2(\frac{\pi x}{L}). \tag{8.1.13}$$

Plug in $\cos^2(\frac{\pi(1/2L)}{L}) = 0$, it can be found

$$N = \frac{EA}{1-\nu^2}\phi_{1,xx}. \tag{8.1.14}$$

8.2 Preliminary verification

8.2.1 Verification of the eigen-buckling analytical solution

The analytical solution Eq. (8.1.9) describes the load-deformation response for one GBT mode. To determine which GBT mode is the most critical, as well as the critical half-wave length, eigen buckling analysis has to performed first. Recalling Eq. (8.1.2) the critical

buckling load for any one GBT mode can be found analytically. There are merely two distortional modes for a C sections, as shown in Figure 8.1(a), and they are both considered. For local buckling modes, the first four local modes in Figure 8.1(b), are considered, because higher local modes like shown in Figure 8.1(c) usually have higher buckling loads.

The numerical test matrix consists of 75 C-sections from SFIA technical guide [94], as shown in Table 8.1. Material properties are used that elastic modulus being 29500 ksi, Poisson's ratio being 0.3, and yielding stress being 55 ksi.

Table 8.1: Numerical test matrix (unit: inch)

Section	Web Depth	Flange Width	Lip Depth			Thickness (t)				
362S162	3.625	1.625	.375	.50	.75	.0346	.0451	.0566	.0713	.1017
600S162	6.0	1.625	.375	.50	.75	.0346	.0451	.0566	.0713	.1017
800S162	8.0	1.625	.375	.50	.75	.0346	.0451	.0566	.0713	.1017
1000S162	10.0	1.625	.375	.50	.75	.0346	.0451	.0566	.0713	.1017
1200S162	12.0	1.625	.375	0.50	.75	.0346	.0451	.0566	.0713	.1017

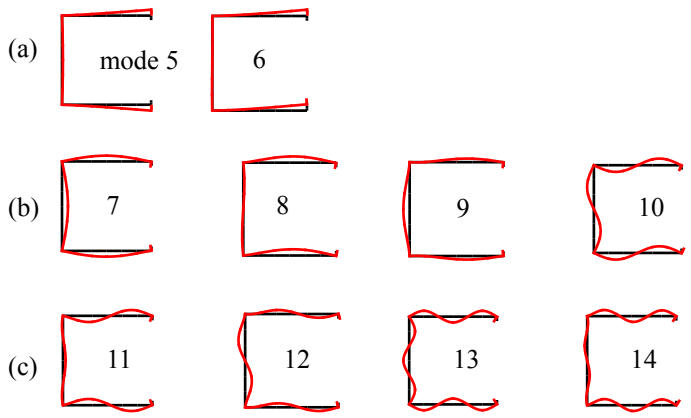

Figure 8.1: Relevant GBT mode shapes: (a) the only two distortional modes; (b) first four local modes; (c) other local modes not taken into account.

Analytical local and distortional buckling loads are calculated by using Eq. (8.1.2) and compared with numerical solution using Finite Strip method and software CUFSM [68]. The results are shown in Figure 8.2 and Figure 8.3. It can be seen the GBT analytical equation is acceptable compared with Finite Strip Method: for local buckling, the mean value is 1.0912 of the Finite Strip numerical solution, and the standard deviation is 0.1572. For distortional buckling, the mean value is 0.9818, and the standard deviation is 0.0245.

There are a few points that the discrepancy between Eq. (8.1.5) and Finite Strip method is significant for local buckling load, e.g., the red dot in Figure 8.2. The largest difference corresponding to the red dot in Figure 8.2 is for the cross-section 1200S162, with lip length 0.375 in. (shortest in the test matrix) and thickness 0.1017 in. (thickest). It is found for this particular cross-section the local-buckling mode shape per GBT cross-sectional analysis differs from that yielded by Finite Strip Method (Figure 8.4). The GBT cross-sectional analysis in this research is carried out per original formulation in [91], which the assumption for local-modes is slightly different than that of Finite Strip method, as it can be seen from Figure 8.4 that all the corners stay unmoved in (a) for Finite Strip method while the lips move laterally in the GBT mode. In the future, it would interesting to use the GBT mode shapes where the kenematical assumption for local-buckling is consistent with Finite Strip method as described in [112].

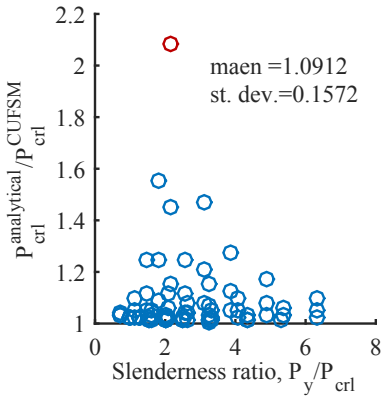

Figure 8.2: Analytical local-buckling loads per Eq. (8.1.5) compared with Finite Strip method.

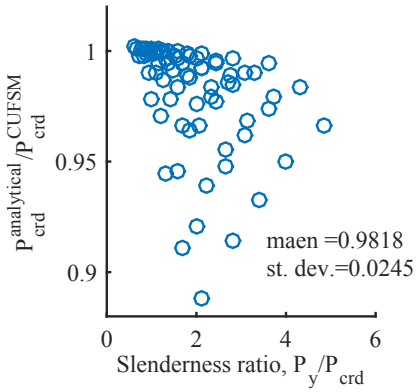

Figure 8.3: Analytical distortional-buckling loads per Eq. (8.1.5) compared with Finite Strip method.

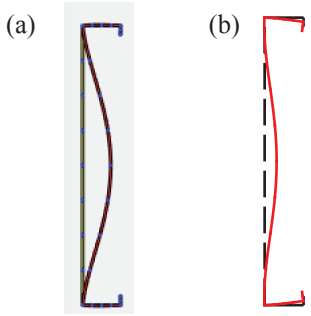

Figure 8.4: Buckling mode shape for cross-section 1200S162: (a) per Finite Strip method; (b) per GBT cross-sectional analysis.

8.2.2 Preliminary verification of the post-buckling analytical solution

The analytical solution aims to provide an approximate and convenient method for calculating the load-deformation response. Its accuracy depends on if one GBT mode analysis is adequate to provide a close approximation for the specific problem. In literature [106], both the cases where one GBT mode analysis provides satisfactory approximation or not can be found. To determine the range where one GBT mode is adequate is listed in the future work chapter of this dissertation. Here, the correctness of the post-buckling analytical derivation is preliminarily verified against the two examples in Chapter 7. Recall the examples involve one 150 mm column dominated by local buckling and one 650 mm column dominated by distortional buckling. It can be seen from Figure 8.5 that analytical formula is valid as the load-deformation responses agree with one mode GBT-element analysis.

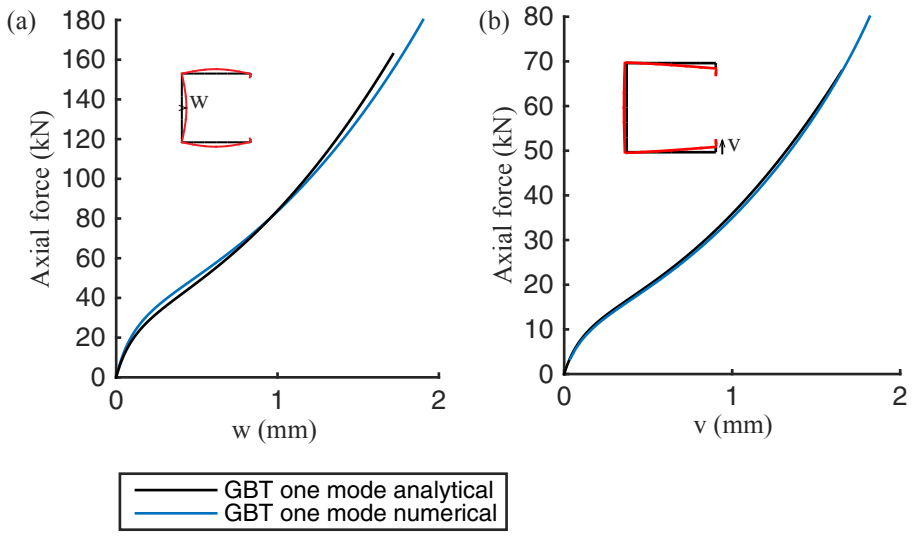

Figure 8.5: Comparison of the load-deformation responses calculated using analytical approach and numerical GBT-element.

8.3 Summary

An approximate, analytical solution for column load-deformation response of one GBT mode is derived. Sinusoidal modal amplitude function is assumed. The formula is preliminary verified by comparing with numerical one GBT mode analysis. The analytical solution can be used to efficiently estimate the load-deformation response for thin-walled members.

Chapter 9

Conclusions

Generalized beam theory elastic buckling analysis and modal decomposition for structural members with holes is introduced. Members with holes are treated as an assembly of multiple prismatic sub-members with compatibility equations for displacements and displacement derivatives across the interfaces of gross and net cross-sections. The finite element method is utilized as a numerical technique for solving the governing GBT differential equation system, where the compatibility conditions are expressed in terms of FE degrees of freedom for first order and eigen-buckling analyses. The geometric stiffness term in the GBT differential equation is modified to include the nonlinear normal stress distribution in the vicinity of the holes, which requires a first order analysis determining the stress state prior to the eigen-buckling analysis. Three examples for a column with a C-section are presented to show how GBT can be used to study the influence of holes on elastic buckling in thin-walled structural members. Local buckling above and below a hole in the net cross-section, known in design as unstiffened strip buckling, was decomposed to reveal flange-web flexural-torsional buckling interaction with unstiffened element local buckling. Distortional buckling modes in the gross cross-section are represented as rigid body flexural and torsional modes of the unstiffened strip and connected flange in the net cross-section. For a C-section column with patterned holes commonly used in upright storage racks, distortional buckling is triggered by the presence of holes, and this buckling deformation is largely defined by the torsional stiffness of the flange-web sub-members at the net cross-section. Preliminary verification is provided by comparing the critical buckling load and shape of the three examples against shell finite element results and more verification is under way. The authors are also working to include this new insight about buckling mode composition at a net cross-section in cold-formed steel capacity prediction.

Elastic buckling mode decomposition of displacement, strain energy and stress components for thin-walled structural members is introduced. Normalized displacement field, bending stress components and strain energy can all be reconstructed with quantitative participation known that can be useful for future design approaches. The method first extracts GBT

modal amplitudes at discrete cross-sections and then reconstructs the continuous modal amplitude field piece-wisely using polynomials. The normalized displacement field, bending stresses and strain energy are all retrieved and decomposed using GBT modal amplitude field and associated GBT constitutive laws. Examples are provided and the results are validated against SFEA results. The errors are minimum for the reconstructed displacement field, stress field and strain energy. Modal decomposition is applied to experimental point clouds. The image reconstructions were used to measure initial geometric imperfections and to track cross-section deformation at column mid-height including distortional buckling and weak axis flexure deformation at peak load. Modal participation throughout the load-deformation response was also characterized.

Buckling mode decomposition of post-buckling is facilitated by performing geometrically non-linear GBT analysis. Potential energy is expressed by using third-order displacement-strain relationship. Finite element formulation is then developed using polynomial shape functions for GBT modal amplitude. A computer program is coded in Matlab with incremental-iterative scheme following the load-deformation curve. By using one local-bucking and one distortional-buckling example, it is shown the modal participation can be obtained for any load-step. The outcome can help understanding buckling mode interaction in the post-buckling range. An approximate, analytical solution for column load-deformation response of one GBT mode is derived. Sinusoidal modal amplitude function is assumed. The formula is preliminary verified by comparing with numerical one GBT mode analysis. The analytical solution can be used to efficiently estimate the load-deformation response for thin-walled members.

Chapter 10

Future Work

Several interesting research topics can be studied based on the buckling mode decomposition methods developed in this dissertation. It is hoped a deeper understanding of interactive buckling will assist developing design methods for coupled buckling limit states.

(1) Buckling mode decomposition of stress components in the post-buckling range.

Understanding buckling mode interaction is of great interest now because the design methods for coupled buckling are yet to be developed. Because stress is closely related to member failure, by investigating the modal participation of stress components, information can be drawn about the interaction of buckling modes. It is well-known for a nonlinear problem modal superposition cease to apply. However, the author suspects the stress can be expressed as summation of modal contribution plus contribution from their interaction.

(2) Buckling mode decomposition in experiments of thin-walled members.

Experimental study is an important tool for tackling interactive buckling. By decomposing the displacement and stress in experiments, mechanics of buckling mode interaction can be better revealed. The main difficulty is the accurate reconstruction of the displacement field during experiment. Stress is a local quantity related to gradient of displacement field. In order to successfully retrieve stress constitution, displacement field needs to be accurately measured. Plus, the warping displacement is more difficult to measure than out-of-plane displacements in experiments, which can be an interesting research topic as well.

(3) Development of design methods for coupled buckling limit states.

After adequate understanding of buckling mode interaction is obtained, a meaningful model based on mechanics can be developed. And then experimental data can be used to adjust the mechanics based model. This is the approach the author attempts to follow.

(4) More thorough verification for the post-buckling analytical solution and applying to strength prediction.

Testing the post-buckling analytical solution for more cross-sections and members is the first task. Determining the range where the analytical solution provides satisfactory approximation can make it more useful for design office. And applying the method to strength prediction in conjunction with appropriate failure criteria is the final goal.

(5) Development of Generalized Beam Theory and computational tool.

The author is interested by advancing the Generalized Beam Theory, e.g., extending the theory to member experiencing large-rotation, as well as to develop design-office tools based on Generalized Beam Theory.

Bibliography

[1] Miguel Abambres, Dinar Camotim, and Nuno Silvestre. GBT-based elastic–plastic post-buckling analysis of stainless steel thin-walled members. *Thin-Walled Structures*, 83(October):85–102, 2014.

[2] Miguel Abambres, Dinar Camotim, and Nuno Silvestre. Modal decomposition of thin-walled member collapse mechanisms. *Thin-Walled Structures*, 74:269–291, January 2014.

[3] Miguel Abambres, Dinar Camotim, Nuno Silvestre, and Kim JR Rasmussen. GBT-based structural analysis of elastic–plastic thin-walled members. *Computers & Structures*, 136:1–23, 2014.

[4] Miguel da Silva Abambres, Nuno Miguel Rosa Pereira Silvestre, and Dinar Reis Zamith Camotim. *Análises elasto-plásticas de 1ª e 2ª ordem de perfis metálicos de parede fina utilizando a teoria generalizada de vigas*. PhD thesis, Universidade de Lisboa, Instituto Superior Técnico, Lisboa, 2014.

[5] Sándor Ádány, Attila L. Joó, and Ben W. Schafer. Buckling mode identification of thin-walled members by using cFSM base functions. *Thin-Walled Structures*, 48(10-11):806–817, October 2010.

[6] Sándor Ádány, Nuno Silvestre, Ben Schafer, and Dinar Camotim. Buckling Analysis of Unbranched Thin-Walled Members: Generalised Beam Theory and Constrained Finite Strip Method. In *III European Conference on Computational Mechanics*, pages 679–679. Springer, 2006.

[7] NAS AISI AISI-S100. *North American Specification for the Design of Cold-formed Steel Structural Members. American Iron and Steel Institute, Washington, DC.* AISI, Washition, DC, 2012.

[8] Steel Stud Manufacturers Association and others. Product technical information. 2010.

[9] Ivan Baláz. Dünnwandige Stäbe mit offenem oder geschlossenem deformierbarem Querschnitt. *Stahlbau*, 68(1):70–77, 1999.

[10] C. Basaglia, D. Camotim, and N. Silvestre. GBT-Based analysis of the local and global buckling behaviour of thin-walled steel frames subjected to arbitrary loadings. In *Proceedings of Fifth International Conference on Advances in Steel Structures (ICASS 2007—Singapore, 5-7/12), JYR Liew, YS Choo (eds.)*, 2007.

[11] C. Basaglia, D. Camotim, and N. Silvestre. GBT-based post-buckling analysis of thin-walled steel members and frames. In *Proceedings of structural stability research council annual stability conference (Nashville, 2-5/4)*, pages 215–37, 2008.

[12] C. Basaglia, D. Camotim, and N. Silvestre. Global buckling analysis of plane and space thin-walled frames in the context of GBT. *Thin-Walled Structures*, 46(1):79–101, 2008.

[13] C. Basaglia, D. Camotim, and N. Silvestre. Global buckling analysis of plane and space thin-walled frames in the context of GBT. *Thin-Walled Structures*, 46(1):79–101, January 2008.

[14] C. Basaglia, D. Camotim, and N. Silvestre. GBT-based local, distortional and global buckling analysis of thin-walled steel frames. *Thin-Walled Structures*, 47(11):1246–1264, November 2009.

[15] C. Basaglia, D. Camotim, and N. Silvestre. Non-linear GBT formulation for open-section thin-walled members with arbitrary support conditions. *Computers & Structures*, 89(21):1906–1919, 2011.

[16] Cilmar Donizeti Basaglia, Dinar Reis Zamith Camotim, and Nuno Miguel Rosa Pereira Silvestre. *Análise não-linear de barras e pórticos metálicos utilizando a teoria generalizada de vigas*. PhD thesis, UTL, Instituto Superior Técnico, Lisboa, 2010.

[17] Zdenek P. Bazant and Luigi Cedolin. *Stability of structures: elastic, inelastic, fracture and damage theories*. World Scientific, 2010.

[18] R. Bebiano, R. Gonçalves, and D. Camotim. A cross-section analysis procedure to rationalise and automate the performance of GBT-based structural analyses. *Thin-Walled Structures*, 92:29–47, July 2015.

[19] Rui Bebiano, Nuno Silvestre, and Dinar Camotim. GBT-based finite element formulation to analyse the buckling behaviour of thin-walled members subjected to non-uniform bending. In *III European Conference on Computational Mechanics*, pages 683–683. Springer, 2006.

[20] Bebiano R. *STABILITY AND DYNAMICS OF THIN-WALLED MEMBERS - APPLICATION OF GENERALISED BEAM THEORY*. PhD thesis, Instituto Superior Técnico, University of Lisbon, portugal, 2010.

[21] Bebiano R. *STABILITY AND DYNAMICS OF THIN-WALLED MEMBERS - APPLICATION OF GENERALISED BEAM THEORY*. PhD thesis, Instituto Superior Técnico, University of Lisbon, portugal, 2010.

[22] Bebiano R., Pina P., Silvestre N., and Camotim D. GBTUL, 2014.

[23] Bebiano R., Pina P., Silvestre N., and Camotim D. GBTUL, 2014.

[24] Bebiano R., Silvestre N., and Camotim D. Buckling and post-buckling behavior of stiffened cold-formed steel columns: a comparative study. In *Proceedings of the 4th European Conference on Steel and Composite Structures*, pages 145–153, Maastricht, 2005. Druck und Verlagshaus Mainz GmbH Aachen.

[25] Junle Cai and Cristopher D. Moen. Buckling Cracker | Structural Systems and Lifecycle Reliability, 2014.

[26] D. Camotim, C. Basaglia, and N. Silvestre. GBT buckling analysis of thin-walled steel frames: A state-of-the-art report. *Thin-Walled Structures*, 48(10-11):726–743, October 2010.

[27] D. Camotim, N. Silvestre, C. Basaglia, and R. Bebiano. GBT-based buckling analysis of thin-walled members with non-standard support conditions. *Thin-Walled Structures*, 46(7):800–815, 2008.

[28] D. Camotim, N. Silvestre, R. Gonçalves, and P. B. Dinis. GBT analysis of thin-walled members: new formulations and applications. *Thin-walled structures: recent advances and future trends in thin-walled structures technology*, pages 137–168, 2004.

[29] Dinar Camotim and Pedro B. Dinis. Coupled instabilities with distortional buckling in cold-formed steel lipped channel columns. *Thin-Walled Structures*, 49(5):562–575, 2011.

[30] Y. K. Cheung. THE FINITE STRIP METHOD IN THE ANALYS OF ELASTIC PLATES WITH TWO OPPOSITE SIMPLY SUPPORTED ENDS. In *ICE Proceedings*, volume 40, pages 1–7. Thomas Telford, 1968.

[31] René Conchon. *Berechnung von Platten mit der verallgemeinerten technischen Biegetheorie (VTB)*. PhD thesis, Inst. für Statik, 2001.

[32] João R. Correia, F. A. Branco, N. M. F. Silva, Dinar Camotim, and Nuno Silvestre. First-order, buckling and post-buckling behaviour of GFRP pultruded beams. Part 1: Experimental study. *Computers & Structures*, 89(21):2052–2064, 2011.

[33] J. M. Davies, C. Jiang, and P. Leach. The analysis of restrained purlins using Generalised Beam Theory. In *12th Int. Speciality Conf. on Cold-Formed Steel Structures. St. Louis, Missouri*, pages 109–20, 1994.

[34] J. M. Davies and P. Leach. First-order generalised beam theory. *Journal of Constructional Steel Research*, 31(2):187–220, 1994.

[35] J. M. Davies, P. Leach, and D. Heinz. Second-order generalised beam theory. *Journal of Constructional Steel Research*, 31(2):221–241, 1994.

[36] P. B. Dinis and D. Camotim. Local/distortional/global mode interaction in simply supported cold-formed steel lipped channel columns. *International Journal of Structural Stability and Dynamics*, 11(05):877–902, 2011.

[37] P. B. Dinis, R. Gonçalves, and D. Camotim. On the local and global buckling behaviour of cold-formed steel hollow-flange channel beams. In *Proceedings of Fifth International Conference on Thin-Walled Structures*, pages 18–20, 2008.

[38] P. Borges Dinis, D. Camotim, and NGBT Silvestre. GBT formulation to analyse the buckling behaviour of thin-walled members with arbitrarily 'branched'open cross-sections. *Thin-Walled Structures*, 44(1):20–38, 2006.

[39] Pedro B. Dinis, Dinar Camotim, and Nuno Silvestre. On the mechanics of thin-walled angle column instability. *Thin-Walled Structures*, 52:80–89, 2012.

[40] Eduardo N. Dvorkin and Klaus-Jürgen Bathe. A continuum mechanics based four-node shell element for general non-linear analysis. *Engineering computations*, 1(1):77–88, 1984.

[41] E. C. Eurocode. 3: Design of steel structures–Part 1.2: General rules–Structural fire design. *Brussels: European Committee for Standardization. DD ENV*, pages 1–3, 1996.

[42] S. C. Fan and Y. K. Cheung. STATIC ANALYSIS OF RIGHT BOX GIRDER BRIDGES BY SPLINE FINITE STRIP MET-HOD. In *ICE Proceedings*, volume 75, pages 311–323. Thomas Telford, 1983.

[43] Gerhard Girmscheid. Ein Beitrag zur Verallgemeinerten Technischen Biegetheorie unter Berucksichtigung der Umfangsdehnungen, Schubverzerrungen & grosser Verformungen. 1984.

[44] Atle Gjelsvik. *The theory of thin walled bars*. Krieger Pub Co, 1981.

[45] R. Gonçalves. *Análise de vigas de parede fina com secção deformável: Novas formulações e aplicações*. PhD thesis, Tese de Doutoramento, Instituto Superior Técnico, 2007.

[46] R. Gonçalves, P. B. Dinis, and D. Camotim. GBT formulation to analyse the first-order and buckling behaviour of thin-walled members with arbitrary cross-sections. *Thin-Walled Structures*, 47(5):583–600, 2009.

[47] Rodrigo Gonçalves and Dinar Camotim. Aplicação da Teoria Generalizada de Vigas (GBT) ao estudo da estabilidade local e global de vigas de aço enformadas a frio (Application of Generalized Beam Theory (GBT) to the study of local and global

stability of cold-formed steel beams). In *Congresso de Métodos Computacionais em Engenharia*, Lisbon, 2004.

[48] Rodrigo Gonçalves and Dinar Camotim. GBT local and global buckling analysis of aluminium and stainless steel columns. *Computers & structures*, 82(17):1473–1484, 2004.

[49] Rodrigo Gonçalves and Dinar Camotim. Thin-walled member plastic bifurcation analysis using generalised beam theory. *Advances in Engineering Software*, 38(8):637–646, 2007.

[50] Rodrigo Goncalves and Dinar Camotim. Steel-concrete composite bridge analysis using generalised beam theory. *Steel and Composite Structures*, 10(3):223–243, 2010.

[51] Rodrigo Gonçalves, Dinar Camotim, and P. Borges Dinis. Box girder bridge analysis using Generalized Beam Theory. In *Proceedings of the International Colloquium on Stability and Ductility of Steel Structures*, Lisbon, 2006.

[52] Rodrigo Gonçalves, Manuel Ritto-Corrêa, and Dinar Camotim. A new approach to the calculation of cross-section deformation modes in the framework of generalized beam theory. *Computational Mechanics*, 46(5):759–781, 2010.

[53] Rodrigo Gonçalves, Manuel Ritto-Corrêa, and Dinar Camotim. A new approach to the calculation of cross-section deformation modes in the framework of generalized beam theory. *Computational Mechanics*, 46(5):759–781, 2010.

[54] Halme T. Generalized Beam Theory in Thin Plate Analysis. In *Proceedings of the 2nd European Conference on Computational Mechanics*, pages 1072–1073, Krakow, Poland,, 2001.

[55] Halme T. Cross-sectional property calculation in Generalized Beam Theory. In *Book of Abstracts of the Fifth World Congress on Computational Mechanics*, volume II, page 450, Vienna, 2002.

[56] Gregory J. Hancock. *Design of Cold-formed Steel Structures: To Australian/New Zealand Standard AS/NZS 4600: 2005*. Australian Steel Institute, North Sydney, 2007.

[57] T. J. R. Hughes and TEi Tezduyar. Finite elements based upon Mindlin plate theory with particular reference to the four-node bilinear isoparametric element. *Journal of applied mechanics*, 48(3):587–596, 1981.

[58] Thomas JR Hughes. *The finite element method: linear static and dynamic finite element analysis*. Courier Corporation, 2012.

[59] Thomas JR Hughes and Wing Kam Liu. Nonlinear finite element analysis of shells: Part I. Three-dimensional shells. *Computer Methods in Applied Mechanics and Engineering*, 26(3):331–362, 1981.

[60] Chunxu Jiang. *Stability analysis of light gauge steel members using the finite element method and the generalized beam theory.* PhD thesis, University of Salford, 1994.

[61] Conor D. Johnson and David A. Kienholz. Finite element prediction of damping in structures with constrained viscoelastic layers. *AIAA Journal*, 20(9):1284–1290, 1982.

[62] Kesti, J. *Local and distortional buckling of perforated steel wall studs.* Ph.D. thesis, Helsinki Univ. of Technology, Espoo, Finland, 2000.

[63] Abraham Lama-Salomon, Fannie Tao, Junle Cai, and Cristopher D. Moen. Buckling mode identification for a cold-formed steel column experiment with 3d image-based reconstruction. In *Proceedings of the Annual Stability Conference*, USA, Nashville, TN., 2015.

[64] Sammy Chia Wo Lau and Gregory J. Hancock. Buckling of thin flat-walled structures by a spline finite strip method. *Thin-Walled Structures*, 4(4):269–294, 1986.

[65] Philip Leach. *The generalised beam theory with finite difference applications.* PhD thesis, University of Salford, 1989.

[66] J. Lepistö, S. Nikula, and E. Niemi. Optimum design of cold-formed sections using generalized beam theory. In *Proceedings of the Second International Conference on Coupled Instabilities in Metal Structures,(CIMS 1996 Liége, 05-07/09), J. Rondal and D. Dubina and V. Gioncu (eds.), Imperial College Press, London*, pages 101–108, 1996.

[67] Z. Li, S. Ádány, and B.W. Schafer. Modal identification for shell finite element models of thin-walled members in nonlinear collapse analysis. *Thin-Walled Structures*, 67:15–24, June 2013.

[68] Z. Li and Benjamin W. Schafer. Buckling analysis of cold-formed steel members with general boundary conditions using CUFSM conventional and constrained finite strip methods. 2010.

[69] Richard H. Macneal and Robert L. Harder. A proposed standard set of problems to test finite element accuracy. *Finite elements in Analysis and Design*, 1(1):3–20, 1985.

[70] J. Michael Davies, Philip Leach, and Angela Taylor. The design of perforated cold-formed steel sections subject to axial load and bending. *Thin-Walled Structures*, 29(1–4):141–157, September 1997.

[71] J. Michael Davies, Philip Leach, and Angela Taylor. The design of perforated cold-formed steel sections subject to axial load and bending. *Thin-Walled Structures*, 29(1–4):141–157, September 1997.

[72] Cristopher D. Moen, Anna Schudlich, and Aaron von der Heyden. Experiments on Cold-Formed Steel C-Section Joists with Unstiffened Web Holes. *Journal of Structural Engineering*, 139(5):695–704, 2013.

[73] Cristopher D. Moen and B. W. Schafer. Experiments on cold-formed steel columns with holes. *Thin-Walled Structures*, 46(10):1164–1182, 2008.

[74] Cristopher D. Moen and B. W. Schafer. Elastic buckling of cold-formed steel columns and beams with holes. *Engineering Structures*, 31(12):2812–2824, 2009.

[75] Cristopher D. Moen and B. W. Schafer. Elastic buckling of thin plates with holes in compression or bending. *Thin-Walled Structures*, 47(12):1597–1607, 2009.

[76] Ralf Möller. *Zur Berechnung prismatischer Strukturen mit beliebigem nicht formtreuem Querschnitt*. na, 1982.

[77] Mihai Nedelcu. GBT-based buckling mode decomposition from finite element analysis of thin-walled members. *Thin-Walled Structures*, 54:156–163, May 2012.

[78] Mihai Nedelcu. Buckling mode identification of perforated thin-walled members by using GBT and shell FEA. *Thin-Walled Structures*, 82:67–81, September 2014.

[79] Mihai Nedelcu. Buckling mode identification of perforated thin-walled members by using GBT and shell FEA. *Thin-Walled Structures*, 82:67–81, 2014.

[80] Silva Nuno. *Behaviour and Strength of Thin-Walled Laminated FRP Structures*. Scholars' Press, Saarbrücken, April 2015.

[81] P. Simão and L. Simões da Silva. Comparative analysis of the stability of open and closed thin-walled section members in the framework of generalised beam theory. In *Proceedings of the 3rd European conference on steel structures (EUROSTEEL 2002—Coimbra, Portugal, 19-20/09)*, volume 1, pages 711–21, 2002.

[82] T. Perry. Agisoft's PhotoScan, 2013.

[83] Stanislav Rendek and Ivan Baláž. Distortion of thin-walled beams. *Thin-Walled Structures*, 42(2):255–277, 2004.

[84] Rendek, S. and Baláž, I. Computer program employing Generalised Beam Theory. pages 809–16, Budapest, 2002.

[85] Benjamin W. Schafer. Review: the direct strength method of cold-formed steel member design. *Journal of constructional steel research*, 64(7):766–778, 2008.

[86] R. Schardt. Anwendung der Erweiterten Technischen Biegetheorie auf die Berechnung prismatischer Faltwerke und Zylinderschalen nach Theorie I. und II. Ordnung. In *Proceedings of the IASS-Symposium on Folded Plates and Prismatic Structures, Wien*, volume 1, 1970.

[87] R. Schardt. Generalized beam theory—an adequate method for coupled stability problems. *Thin-Walled Structures*, 19(2):161–180, 1994.

[88] Richard Schardt. Eine Erweiterung der technischen Biegelehre für die Berechnung biegesteifer prismatischer Faltwerke. volume Heft 6, pages 161–171, Stahlbau, 1966.

[89] Richard Schardt. Einfluss der Querschnittsverformung auf das Biegeknicken und das Biegedrillknicken. In *8. IVBH Kongress*, pages 359–362, Schlussbericht, Wien, 1968.

[90] Richard Schardt. *Verallgemeinerte technische biegetheorie*. Springer, Berlin, 1989.

[91] Richard Schardt. *Verallgemeinerte technische biegetheorie*. Springer, Berlin, 1989.

[92] Richard Schardt and C. Schardt. Unstiffened element with torsional restraint – an analytical approach for post-buckling behaviour using GBT. In *Proceedings of the International Colloquium on Stability and Ductility of Steel Structures*, pages 177–188, Lisbon, 2006.

[93] Richard Schardt, Wolfgang Schrade, Richard Schardt, and Richard Schardt. *Kaltprofilpfetten*. Institut für Statik, Technische Hochschule Darmstadt, 1982.

[94] SFIA. Technical Guide for Cold-Formed Steel Framing Products. Technical report, 2015.

[95] N. Freitas Silva and N. Silvestre. On the influence of material couplings on the linear and buckling behavior of I-section composite columns. *International Journal of Structural Stability and Dynamics*, 7(02):243–272, 2007.

[96] N. M. F. Silva, D. Camotim, and N. Silvestre. GBT cross-section analysis of thin-walled members with arbitrary cross-sections: a novel approach. In *Proceedings of the Fifth International Conference on Thin-Walled Structures 2008*, pages 1161–1171, 2008.

[97] N. M. F. Silva, D. Camotim, and N. Silvestre. Generalized beam theory formulation able to capture load application and localized web buckling effects. In *Proceedings of 19th international specialty conference on recent research and developments in cold-formed steel design and construction, St. Louis*, pages 14–15, 2008.

[98] N. M. F. Silva, D. Camotim, N. Silvestre, J. R. Correia, and F. A. Branco. First-order, buckling and post-buckling behaviour of GFRP pultruded beams. Part 2: Numerical simulation. *Computers & Structures*, 89(21):2065–2078, 2011.

[99] N. M. F. Silva, D. Camotim, N. Silvestre, and R. Degenhardt. On the use of generalized beam theory to assess the buckling and postbuckling behavior of laminated CFRP cylindrical stiffened panels. *International Journal of Structural Stability and Dynamics*, 10(04):737–760, 2010.

[100] N. M. F. Silva, N. Silvestre, D. Camotim, and M. Mahendran. Non-linear behaviour and failure analysis of laminated FRP composite thin-walled members. In *Proceedings of fifth international conference on thin-walled structures, Ictws*, pages 18–20, 2008.

[101] N. Silvestre. Generalised beam theory to analyse the buckling behaviour of circular cylindrical shells and tubes. *Thin-Walled Structures*, 45(2):185–198, February 2007.

[102] N. Silvestre. Buckling behaviour of elliptical cylindrical shells and tubes under compression. *International Journal of Solids and Structures*, 45(16):4427–4447, August 2008.

[103] N. Silvestre. Length dependence of critical measures in single-walled carbon nanotubes. *International Journal of Solids and Structures*, 45(18):4902–4920, 2008.

[104] N. Silvestre and D. Camotim. First-order generalised beam theory for arbitrary orthotropic materials. *Thin-Walled Structures*, 40(9):755–789, 2002.

[105] N. Silvestre and D. Camotim. Second-order generalised beam theory for arbitrary orthotropic materials. *Thin-Walled Structures*, 40(9):791–820, 2002.

[106] N. Silvestre and D. Camotim. Nonlinear generalized beam theory for cold-formed steel members. *International Journal of Structural Stability and Dynamics*, 3(04):461–490, 2003.

[107] N. Silvestre and D. Camotim. Nonlinear generalized beam theory for cold-formed steel members. *International Journal of Structural Stability and Dynamics*, 3(04):461–490, 2003.

[108] N. Silvestre and D. Camotim. Distortional buckling formulae for cold-formed steel C and Z-section members: Part I—derivation. *Thin-Walled Structures*, 42(11):1567–1597, 2004.

[109] N. Silvestre and D. Camotim. Distortional buckling formulae for cold-formed steel C- and Z-section members: Part II—Validation and application. *Thin-Walled Structures*, 42(11):1599–1629, 2004.

[110] N. Silvestre and D. Camotim. Distortional buckling formulae for cold-formed steel rack-section members. *Steel and Composite Structures*, 4(1):49–75, 2004.

[111] N. Silvestre and D. Camotim. GBT-based local and global vibration analysis of loaded composite open-section thin-walled members. *International Journal of Structural Stability and Dynamics*, 6(01):1–29, 2006.

[112] N. Silvestre, D. Camotim, and N. F. Silva. GENERALIZED BEAM THEORY REVISITED: FROM THE KINEMATICAL ASSUMPTIONS TO THE DEFORMATION MODE DETERMINATION. *International Journal of Structural Stability and Dynamics*, 11(05):969–997, October 2011.

[113] Nuno Silvestre and Dinar Camotim. Local-plate and distortional postbuckling behavior of cold-formed steel lipped channel columns with intermediate stiffeners. *Journal of structural engineering*, 132(4):529–540, 2006.

[114] Fernando Pedro Simões da Silva Simão and others. *Post-buckling bifurcational analysis of thin-walled prismatic members in the context of the generalized beam theory*. PhD thesis, 2007.

[115] P. Simão and L. Simoes da Silva. A unified energy formulation for the stability analysis of open and closed thin-walled members in the framework of the generalized beam theory. *Thin-walled structures*, 42(10):1495–1517, 2004.

[116] P. Simão and L. Simões da Silva. The post-buckling behavior of open cross section thin-walled columns in the context of Generalized Beam Theory (GBT). pages 891–898, Balkema, 2003.

[117] P. Simão and L. Simões da Silva. GBT stability analysis of thin-walled cold formed slender hollow- flange steel beams. In *Proceedings of the Fifth International Conference on Coupled Instabilities in Metal Structures*, volume I, pages 257–264, Sydney, Australia, 2008.

[118] P. Simão and L. Simões da Silva. Comportamento pós-bifurcacional de colunas metálicas enformadas a frio com secção de parede fina no contexto da GBT [Post-buckling behavior of thin-walled cold- formed steel columns in the context of GBT],. In *Actas do VII Congresso de Mecânica Aplicada e Computacional*, volume 1, pages 269–278, Évora, Portugal, 2003.

[119] J. C. Simo, D. D. Fox, and M. S. Rifai. On a stress resultant geometrically exact shell model. Part II: The linear theory; computational aspects. *Computer Methods in Applied Mechanics and Engineering*, 73(1):53–92, 1989.

[120] Simulia. Abaqus/CAE, 2012.

[121] Frank H. Smith and Cristopher D. Moen. Finite strip elastic buckling solutions for thin-walled metal columns with perforation patterns. *Thin-Walled Structures*, 79:187–201, June 2014.

[122] Fannie Tao, Abraham Lama-Salomon, and Cristopher Dennis Moen. Experiments on cold-formed steel studs with concrete end supports. Technical report.

[123] Shahabeddin Torabian, Baofeng Zheng, and Benjamin W. Schafer. Experimental response of cold-formed steel lipped channel beam-columns. *Thin-Walled Structures*, 89:152–168, April 2015.

[124] Theodor Von Karman, Ernest E. Sechler, and L. H. Donnell. The strength of thin plates in compression. *Trans. ASME*, 54(2):53–57, 1932.

[125] Changchang Wu. Towards linear-time incremental structure from motion. In *3D Vision-3DV 2013, 2013 International Conference on*, pages 127–134. IEEE, 2013.